

Mechanisms of Ion Migration in Ceramic Oxides

Von der Naturwissenschaftliche Fakultät
der Universität Hannover
zur Erlangung des Grades

Doktor der Naturwissenschaften

Dr. rer. nat.
genehmigte Dissertation
von

M.Sc. Mohammad Mazharul Islam

geboren am 27.07.1977
in Dhaka, Bangladesch

2005

Referent Priv.-Doz. Dr. T. Bredow
Korreferent: Prof. Dr. K. Jug
Tag der Promotion: 11.07.2005

I would like to express my utmost gratitude to Priv.-Doz. Dr. T. Bredow for his wholehearted guidance and invaluable help. His encouragement and advice have helped me to complete my thesis successfully.

I am grateful to Prof. Dr. K. Jug for giving me an opportunity to work in his research group. I thank him for his fruitful discussion.

I am deeply indebted to Prof. C. Minot, Laboratoire de Chimie Théorique, UPMC, Paris, for allowing me to work in his research group, for his proper guidance and kind hospitality, during my stay in Paris.

I would like to thank all my colleagues and friends for their help and encouragement.

I thank the state of Lower Saxony for granting me the Georg-Christoph-Lichtenberg scholarship.

Abstract

Bulk properties of Li_2O , B_2O_3 and $\text{Li}_2\text{B}_4\text{O}_7$ are investigated quantum-chemically. The reliability of three density-functional theory (DFT) methods (PWGGA, PWGGA-US and PWGGA-PAW), two DFT-Hartree Fock (HF) hybrid methods (PW1PW and B3LYP) and the semiempirical method MSINDO is examined by comparison of calculated results to available experimental data. The results at DFT level are also compared for different types of basis functions, either based on linear combinations of atom-centered orbitals (LCAO), or on plane waves, as implemented in the crystalline orbital program CRYSTAL and in VASP, respectively. The basis set dependence of the calculated properties is investigated for the LCAO based methods. In the plane wave based methods (PWGGA-US and PWGGA-PAW), ultrasoft pseudopotentials (US PP) and projector-augmented wave (PAW) potentials are used to represent the core electrons. The effect of energy cutoff (E_{cut}) on the calculated properties is investigated. A comparative study is performed for the low and high space-group symmetry of trigonal B_2O_3 . The cation vacancy and F center of Li_2O are investigated. Li^+ ion diffusion in Li_2O is investigated by calculating the activation energy E_A for the migration of Li^+ ion via cation vacancy. The calculated values are compared with the experiment. The ionic conductivity in the (001) direction of $\text{Li}_2\text{B}_4\text{O}_7$ is investigated. The calculated E_A values are compared with experimental results from the literature. The structure and stability of Li_2O (111) and (110) surfaces and the B_2O_3 (001) surface are calculated. The interface of $\text{Li}_2\text{O}:\text{B}_2\text{O}_3$ nanocomposite is modeled by the combination of supercells of Li_2O (111) and B_2O_3 (001) surface. The migration of Li^+ ion via cation vacancy is studied in the interface region. The calculated E_A is compared with that in the nanocrystalline Li_2O , and it is shown that the conductivity is enhanced in the $\text{Li}_2\text{O}:\text{B}_2\text{O}_3$ nanocomposite compared to that in Li_2O .

Keywords: density-functional theory, pseudopotential, nanocomposites, interface region

Kurzzusammenfassung

Festkörpereigenschaften von Li_2O , B_2O_3 und $\text{Li}_2\text{B}_4\text{O}_7$ wurden mit Hilfe quantenchemischer Methoden untersucht. Die Rechnungen erfolgten auf der Basis von Dichtefunktionaltheorie (PWGGA, PWGGA-US und PWGGA-PAW) und DFT-Hartree-Fock-Hybridmethoden (PW1PW und B3LYP) sowie mit der semiempirischen Methode MSINDO. Die erhaltenen Ergebnisse wurden mit experimentellen Daten verglichen. Im Falle der DFT-Rechnungen wurden als Basissätze sowohl Linearkombinationen von atomzentrierten Basisfunktionen (LCAO), wie sie in der Kristallorbitalmethode CRYSTAL implementiert sind, als auch ebene Wellen, die im Programm VASP benutzt werden, verwendet. Im Falle der LCAO-basierten Methoden sind die berechneten Eigenschaften auf eine Basissatzabhängigkeit überprüft worden. Zur Darstellung der inneren Elektronen wurden bei den Methoden mit ebenen Wellen (PWGGA-US und PWGGA-PAW) ultraweiche Pseudopotentiale (**ultrasoft pseudopotential**) und "projector-augmented wave" Potentiale verwendet. Weiterhin ist der Effekt des Energiegrenzwertes ebener Wellen (E_{cut}) auf die berechneten Eigenschaften untersucht worden. In einer vergleichenden Studie wurden das niedrig- und hochsymmetrische trigonale B_2O_3 untersucht. Am Li_2O wurden Rechnungen für die Kationenfehlstelle und das F-Zentrum durchgeführt. Für die Diffusion von Li^+ -Ionen im Li_2O ist die Aktivierungsenergie E_A der Li^+ -Wanderung über Kationenfehlstellen berechnet und mit experimentellen Daten verglichen worden. Die Ionenleitfähigkeit in (001)-Richtung im $\text{Li}_2\text{B}_4\text{O}_7$ wurde untersucht und die erhaltene E_A mit dem Experiment verglichen. Die Struktur und Stabilität der Li_2O (111)- und (110)- sowie die B_2O_3 (001)- Oberflächen wurden berechnet. Die Grenzfläche von $\text{Li}_2\text{O}:\text{B}_2\text{O}_3$ -Nanopartikeln ist durch eine Kombination von Superzellen der Li_2O (111)- und B_2O_3 (001)- Oberflächen modelliert worden. Die Wanderung von Li^+ -Ionen über Kationenfehlstellen in der Grenzflächenregion wurde untersucht. Ein Vergleich der berechneten Aktivierungsenergien zeigt, daß die Leitfähigkeit im $\text{Li}_2\text{O}:\text{B}_2\text{O}_3$ gegenüber dem reinen Li_2O erhöht ist.

Schlagwörter: Dichtefunktionaltheorie, Pseudopotentiale, Nanopartikeln, Grenzflächenregion

Contents

1	Introduction	1
2	Quantum Chemical Background	3
2.1	Hartree-Fock Method	4
2.2	Semiempirical Methods	8
2.3	Density Functional Theory	13
3	Models of Solids and Surfaces	17
3.1	Periodic Models	18
3.1.1	Localized basis	20
3.1.2	Plane Wave basis	21
3.2	Cyclic Cluster Model	25
4	Experimental Background	29
5	Bulk Properties of Li_2O	31
5.1	Stoichiometric Li_2O : MSINDO-CCM results	32
5.1.1	Parameterization	32
5.1.2	Convergence Test	34
5.2	Stoichiometric Li_2O : DFT results	36
5.3	Defect properties of Li_2O	41
5.3.1	Cation vacancy	42
5.3.2	F center	47
5.4	Diffusion of Li^+ ion in Li_2O	52
6	Bulk Properties of B_2O_3	58
6.1	B_2O_3 with P3_121 space group	60
6.2	Comparison between P3_121 and P3_1 space group	63
7	Bulk Properties of $\text{Li}_2\text{B}_4\text{O}_7$	65
7.1	Structure Optimization	67
7.2	Binding Energy	70
7.3	Band Structure and Density of States	71

7.4	Electronic charge density	74
8	Migration of Li⁺ ion in Li₂B₄O₇	77
8.1	Cation vacancy in lithium tetraborate	77
8.2	Migration of Li ⁺ ion	80
9	Model System for the Li₂O:B₂O₃ nanocomposite	84
9.1	Construction of the Li ₂ O:B ₂ O ₃ interface	84
9.1.1	Surface energy of Li ₂ O	85
9.1.2	Surface energy of B ₂ O ₃	87
9.1.3	Interface of Li ₂ O:B ₂ O ₃ nanocomposite	89
9.2	Defect properties in Li ₂ O:B ₂ O ₃ nanocomposite	92
9.2.1	Cation vacancy	92
9.2.2	Migration of Li ⁺ ion	93
10	Summary	96
	References	98

1 Introduction

In recent years, ceramic oxides have attracted considerable attention due to their broad potential applications as advanced materials with controlled chemical, mechanical, electrical, magnetic, and optical properties. Many of these properties are attributed to the mobility of metal ions. A metal ion can migrate from a regular site to an interstitial site or to an adjacent defect position. An important criterion for the probability of these processes is the corresponding activation energy. Sometimes, it is difficult to obtain this quantity with experimental techniques. Quantum chemical approaches can be utilized to determine the activation energy for the elementary steps. Recent experimental investigations for the $\text{Li}_2\text{O}:\text{B}_2\text{O}_3$ nanocomposite show that the ionic conductivity increases with increasing B_2O_3 content although B_2O_3 is an insulator. A possible explanation discussed in the literature is the formation of lattice defects at the phase boundary between nano-crystalline Li_2O and B_2O_3 which leads to an enhanced mobility of Li^+ ions. Due to this property, the $\text{Li}_2\text{O}:\text{B}_2\text{O}_3$ nanocomposite has potential applications in battery systems, fuel cells or gas sensors. In the present work, the enhanced mobility of Li^+ ions in $\text{Li}_2\text{O}:\text{B}_2\text{O}_3$ nanocomposite is investigated theoretically using both semiempirical and density functional theory (DFT) methods.

The structural, energetic and electronic properties of Li_2O , B_2O_3 , and $\text{Li}_2\text{B}_4\text{O}_7$ are studied with periodic quantum chemical calculations using the CRYSTAL03 package, the VASP package and the cyclic cluster model (CCM) implemented in the semiempirical method MSINDO. As a test for the methods, calculated bulk properties for all these systems are compared with available experimental data.

Li_2O is a fast ionic conductor. Available experimental information on the ionic transport in this system shows that the mobile species is the Li^+ ion and the most likely mechanism for its migration is via cation vacancies. Another prominent irradiation defect is known as F center, an oxygen vacancy trapping two electrons. The formation energy of the cation vacancy and the F center in Li_2O is calculated. The effect of relaxation and the influence of defects on the electronic properties are investigated for the both types of defect in Li_2O . A possible mechanism of the Li^+ migration is investigated by calculating the energy barrier for the movement of Li^+ from a regular site to an adjacent cation vacancy defect position.

$\text{Li}_2\text{B}_4\text{O}_7$ (LTB) is a Li^+ ion conductor along the (001) direction. In the present study, LTB is considered as the first model system for the interface region of $\text{Li}_2\text{O}:\text{B}_2\text{O}_3$ nanocomposite. The cation vacancy defect in LTB is investigated. The defect formation energy is calculated and the effect of relaxation is investigated for the defective system. The mechanism of Li^+ ion migration is investigated by calculating the energy barrier for the movement of Li^+ ions from regular sites to adjacent cation vacancy defect positions along the tetragonal axis.

A more realistic model system of the $\text{Li}_2\text{O}:\text{B}_2\text{O}_3$ interface region is created by combining surfaces of the two oxides. The surface energies of (110) and (111) surfaces of Li_2O and (001) surface of B_2O_3 are calculated. Using the most favorable surface structures, such as, (111) for Li_2O and (001) for B_2O_3 , the mixed model structure of $\text{Li}_2\text{O}:\text{B}_2\text{O}_3$ is prepared. The mixed structure is optimized with the relaxation of all atoms in the interface region and the migration of a Li^+ ion is studied.

2 Quantum Chemical Background

The Schrödinger equation [1–3] contains the essence of all chemistry. To quote Dirac: "The underlying physical laws necessary for the mathematical theory of a large part of physics and the whole of chemistry are thus completely known" [4]. The time-independent Schrödinger equation is

$$\hat{H}\Psi = E\Psi \quad (2.1)$$

where \hat{H} is the Hamilton operator, Ψ is the wavefunction that contains all information about the quantum system and E is the energy of the system. The nonrelativistic Hamilton operator \hat{H} is expressed (in atomic units) for a system of N nuclei and n electrons as,

$$\hat{H} = -\sum_I \frac{1}{2M_I} \nabla_I^2 - \sum_i \frac{1}{2} \nabla_i^2 - \sum_I \sum_i \frac{Z_I}{r_{Ii}} + \sum_{j>i} \frac{1}{r_{ij}} + \sum_{J>I} \frac{Z_I Z_J}{R_{IJ}} \quad (2.2)$$

The first two terms describe the kinetic energy of the nuclei and the electrons, respectively. Here M_I is the mass and Z_I is the atomic number of a nucleus I . The remaining three terms define the potential part of the Hamiltonian and represent the attractive electrostatic interaction between the nuclei and the electrons and the repulsive potential due to the electron-electron and nucleus-nucleus interactions, respectively. r_{ij} is the distance between the electrons i and j , r_{Ii} is the distance between nucleus I and electron i , and R_{IJ} is the distance between the nuclei I and J .

Since nuclei are much heavier than electrons, they move more slowly. Hence, to a good approximation, the electrons in a molecule can be considered to be moving in the field of fixed nuclei. Within this approximation, the first term of (2.2), the kinetic energy of the nuclei, can be neglected and the last term of (2.2), the repulsion between the nuclei, can be considered to be constant. The remaining terms in (2.2) are called the electronic Hamiltonian (\hat{H}_{el}). This separation of electronic and nuclear motions is called the Born-Oppenheimer approximation [5]. The Schrödinger equation (2.1) is reduced to the electronic Schrödinger equation,

$$\hat{H}_{\text{el}}\Psi_{\text{el}} = E_{\text{el}}\Psi_{\text{el}} \quad (2.3)$$

where \hat{H}_{el} has the following simplified form,

$$\hat{H}_{\text{el}} = -\sum_i \frac{1}{2} \nabla_i^2 - \sum_I \sum_i \frac{Z_I}{r_{Ii}} + \sum_{j>i} \frac{1}{r_{ij}} \quad (2.4)$$

The solutions of this equation are the electronic wavefunction Ψ_{el} and the electronic energy E_{el} . It is convenient to write the electronic Hamiltonian operator (\hat{H}_{el}) as a sum of one- and two-electron operators \hat{h}_1 and \hat{h}_{12} as following (2.5),

$$\begin{aligned}\hat{H}_{\text{el}} &= \sum_i^n \hat{h}_1(i) + \sum_{j>i}^n \hat{h}_{12}(i, j) \\ \hat{h}_1(i) &= -\frac{1}{2}\nabla_i^2 - \sum_I^N \frac{Z_I}{r_{Ii}} \\ \hat{h}_{12}(i, j) &= \frac{1}{r_{ij}}\end{aligned}\tag{2.5}$$

The total energy E_{tot} of the system is the sum of the electronic energy E_{el} and the constant nuclear repulsion term.

$$E_{\text{tot}} = E_{\text{el}} + E_{\text{nuc}}\tag{2.6}$$

where

$$E_{\text{nuc}} = \sum_{J>I}^N \frac{Z_I Z_J}{R_{IJ}}\tag{2.7}$$

2.1 Hartree-Fock Method

The Schrödinger equation for systems with more than one electron cannot be solved exactly, even for the helium atom. The helium atom has three particles (two electrons and one nucleus) and is an example of a *three-body problem*. No exact solutions have been found so far for systems that involve three or more interacting particles. In such cases, the motion of each electron is coupled to the motion of all other electrons. A further complication of multi-electron species is that the electron spin must be accounted.

To study polyelectronic atoms or molecules, approximations to the exact solutions of Schrödinger equation are necessary. One possibility is represented by the Hartree-Fock method which is based on the assumption that every electron moves in a potential created by the nuclei and the average potential of all the other electrons. In this method the n -electron wavefunction is an antisymmetrized product of n one-electron wavefunctions $\phi_i(\mathbf{q}_i)$. This product is referred to as a Slater determinant, Φ_0 [1].

$$\Psi_{\text{el}} \approx \Phi_0 = \frac{1}{\sqrt{n!}} \begin{vmatrix} \phi_1(\mathbf{q}_1) & \phi_2(\mathbf{q}_1) & \cdots & \phi_n(\mathbf{q}_1) \\ \phi_1(\mathbf{q}_2) & \phi_2(\mathbf{q}_2) & \cdots & \phi_n(\mathbf{q}_2) \\ \vdots & \vdots & \ddots & \vdots \\ \phi_1(\mathbf{q}_n) & \phi_2(\mathbf{q}_n) & \cdots & \phi_n(\mathbf{q}_n) \end{vmatrix}\tag{2.8}$$

The pre-factor $1/\sqrt{n!}$ is the normalization constant of the wavefunction. The one-electron functions $\phi_i(\mathbf{q}_i)$ are called spin orbitals, and are composed of a spatial orbital $\psi_i(\mathbf{r})$ and one of the two spin functions, $\sigma(+1/2)$ or $\sigma(-1/2)$.

$$\begin{aligned}\psi(\mathbf{r})\sigma\left(\frac{1}{2}\right) &= \psi(\mathbf{r})\alpha \\ \psi(\mathbf{r})\sigma\left(-\frac{1}{2}\right) &= \psi(\mathbf{r})\beta\end{aligned}\tag{2.9}$$

Spatial orbitals are assumed to form an orthonormal set,

$$\langle\psi_i | \psi_j\rangle = \delta_{ij}\tag{2.10}$$

Within the Hartree-Fock approximation the spatial orbitals $\{\psi\}$ are varied, under the orthonormality constraint (2.10), until a Slater determinant Φ_0 is obtained, which yields the lowest energy. After expansion of the determinant, the Hartree-Fock energy for a closed-shell system can be expressed as

$$\begin{aligned}E_0^{\text{HF}} &= \langle\Phi_0 | \hat{H}_{\text{el}} | \Phi_0\rangle \\ &= 2 \sum_i^{n/2} h_{ii} + \sum_i^{n/2} \sum_j^{n/2} (2J_{ij} - K_{ij})\end{aligned}\tag{2.11}$$

where

$$\begin{aligned}h_{ii} &= \int \psi_i^*(1)\hat{h}_1(1)\psi_i(1) d\mathbf{r}_1 = \langle i | \hat{h}_1 | i\rangle \\ J_{ij} &= \iint \psi_i^*(1)\psi_j^*(2)\hat{h}_{12}\psi_i(1)\psi_j(2) d\mathbf{r}_1 d\mathbf{r}_2 = (ii | jj) \\ K_{ij} &= \iint \psi_i^*(1)\psi_j^*(2)\hat{h}_{12}\psi_j(1)\psi_i(2) d\mathbf{r}_1 d\mathbf{r}_2 = (ij | ij)\end{aligned}\tag{2.12}$$

J_{ij} and K_{ij} are called Coulomb and exchange integrals, respectively. The Hartree-Fock equations, which determine the $\{\psi\}$ for which E_0^{HF} attains its lowest value, are given by

$$\hat{F}\psi_i = \epsilon_i\psi_i\tag{2.13}$$

ϵ_i are the eigenvalues of the Fock operator \hat{F} . According to Koopmans' Theorem [6], the negative values of the orbital energies (ϵ_i) are a first approximation to ionization energies. The Fock operator \hat{F} is a one-electron operator defined as

$$\hat{F}(1) = \hat{h}_1(1) + \sum_j^{n/2} \left[2\hat{J}_j(1) - \hat{K}_j(1) \right]\tag{2.14}$$

$$\begin{aligned}\text{where} \quad \hat{J}_j(1)\psi_i(1) &= \int \psi_j^*(2)\hat{h}_{12}\psi_j(2) d\mathbf{r}_2 \psi_i(1) \\ \hat{K}_j(1)\psi_i(1) &= \int \psi_j^*(2)\hat{h}_{12}\psi_i(2) d\mathbf{r}_2 \psi_j(1)\end{aligned}$$

A direct numerical solution of the Hartree-Fock equations for molecules is impossible. Roothaan [7] proposed to construct the molecular orbitals (MOs) ψ_i by a linear combination of atom-centered basis functions $\{\chi_\mu\}$ (LCAO) [1].

$$\psi_i = \sum_{\mu}^m c_{\mu i} \chi_{\mu} \quad (2.15)$$

Here $c_{\mu i}$ are the MO coefficients. In this way the differential equation (2.3) is converted into a set of algebraic equations [2] which are then solved by standard matrix algebra techniques.

In quantum-chemical calculations, two different kinds of atomic orbitals are used, Slater-type and Gaussian-type orbitals [1]. Slater-type orbitals have the form

$$\chi^{Slater} = \frac{[2\zeta]^{n+1/2}}{[(2n)!]^{1/2}} r^{n-1} \exp(-\zeta r) Y_l^m(\theta, \varphi) \quad (2.16)$$

where ζ is the orbital exponent, $Y_l^m(\theta, \varphi)$ is a spherical harmonic function, and n , l , and m are quantum numbers. Gaussian-type orbitals are defined as

$$\chi^{Gauss} = \left(\frac{2\alpha}{\pi}\right)^{3/4} \left[\frac{(8\alpha)^{i+j+k} i! j! k!}{(2i)! (2j)! (2k)!}\right]^{1/2} x^i y^j z^k \exp(-\alpha r^2) \quad (2.17)$$

Here i , j and k are integers, x , y , and z are Cartesian coordinates and α is the orbital exponent of the Gaussian-type function (GTF). Instead of using the individual GTFs (2.17) as basis functions, the current practice is to take each basis function as a linear combination (contraction) of a small number of GTFs according to

$$\chi_r^{CGTF} = \sum_{\mu} d_{\mu r} \chi_{\mu}^{Gauss} \quad (2.18)$$

where χ_r^{CGTF} is called a contracted Gaussian-type function (CGTF) and χ_{μ}^{Gauss} 's are called primitive Gaussians. χ_{μ}^{Gauss} 's are centered on the same atom and have the same i , j , k values but different α 's. The coefficients $d_{\mu r}$ are optimized for free atoms and held fixed during molecular calculations. By using CGTF instead of primitive Gaussians as the basis set, the number of variational coefficients to be determined is reduced, which gives large savings in computational time with little loss in accuracy if the contraction coefficients $d_{\mu r}$ are well chosen.

By substituting (2.15) in (2.13) a matrix equation for $c_{\mu i}$ is obtained which is called the Roothaan-Hall equation (2.19).

$$\sum_{\nu}^m F_{\mu\nu} c_{\nu i} = \epsilon_i \sum_{\nu}^m S_{\mu\nu} c_{\nu i} ; \mu = 1, 2, \dots, m \text{ and } i = 1, 2, \dots, m \quad (2.19)$$

$$\mathbf{FC} = \mathbf{SC}\epsilon$$

The overlap matrix \mathbf{S} has elements

$$S_{\mu\nu} = \int \chi_{\mu}^*(1) \chi_{\nu}(1) d\mathbf{r}_1 \quad (2.20)$$

The Fock matrix \mathbf{F} has elements

$$\begin{aligned} F_{\mu\nu} &= \int \chi_{\mu}^*(1) \hat{F}(1) \chi_{\nu}(1) d\mathbf{r}_1 \\ &= H_{\mu\nu} + \sum_{\rho}^m \sum_{\sigma}^m P_{\rho\sigma} \left[(\mu\nu | \rho\sigma) - \frac{1}{2} (\mu\sigma | \rho\nu) \right] \end{aligned} \quad (2.21)$$

where

$$\begin{aligned} H_{\mu\nu} &= \int \chi_{\mu}^*(1) \hat{h}_1 \chi_{\nu}(1) d\mathbf{r}_1 \\ (\mu\nu | \rho\sigma) &= \iint \chi_{\mu}^*(1) \chi_{\rho}^*(2) \hat{h}_{12} \chi_{\nu}(1) \chi_{\sigma}(2) d\mathbf{r}_1 d\mathbf{r}_2 \\ P_{\mu\nu} &= 2 \sum_i^{n/2} c_{\mu i} c_{\nu i} \end{aligned}$$

The Hartree-Fock energy, E_0^{HF} , is obtained as

$$E_0^{\text{HF}} = \frac{1}{2} \sum_{\mu}^m \sum_{\nu}^m P_{\mu\nu} (H_{\mu\nu} + F_{\mu\nu})$$

$H_{\mu\nu}$ and $P_{\mu\nu}$ are the elements of the core matrix \mathbf{H} and the density matrix \mathbf{P} , respectively. An orthonormal set of basis functions is obtained as

$$\lambda_{\nu} = \sum_{\mu}^m a_{\mu\nu} \chi_{\mu} \quad (2.22)$$

Here the coefficients $a_{\mu i}$ are the elements of transformation matrix $\mathbf{S}^{-1/2}$. In this orthonormal set the overlap matrix will be the unit matrix.

$$S_{\mu\nu}^{\lambda} = \langle \lambda_{\mu} | \lambda_{\nu} \rangle = \delta_{\mu\nu} \quad (2.23)$$

The Hartree-Fock-Roothaan equations (2.19) in the orthogonal λ -basis have a simpler form as

$$\mathbf{F}^{\lambda} \mathbf{C}^{\lambda} = \mathbf{C}^{\lambda} \epsilon \quad (2.24)$$

The elements of the matrix \mathbf{C}^{λ} are the coefficients in the linear expansion of the molecular orbitals $\{\psi_i\}$ in terms of the orthonormal basis functions $\{\lambda_{\mu}\}$.

$$\psi_i = \sum_{\mu}^m c_{\mu i}^{\lambda} \lambda_{\mu} \quad (2.25)$$

The \mathbf{F}^λ and \mathbf{F} matrices and \mathbf{C}^λ and \mathbf{C} matrices are related in the following way.

$$\mathbf{F}^\lambda = \mathbf{S}^{-1/2} \mathbf{F} \mathbf{S}^{-1/2} \quad \text{and} \quad \mathbf{C}^\lambda = \mathbf{S}^{1/2} \mathbf{C} \quad (2.26)$$

The Hartree-Fock-Roothaan equations are solved by an iterative procedure called self-consistent field (SCF) procedure [2]. In this iterative method, an initial guess is made for the coefficients $\mathbf{C}^{(0)}$ and a first density matrix $\mathbf{P}^{(0)}$ is obtained. The molecular integrals are calculated for a given nuclear configuration $\{\mathbf{R}\}$. The Fock matrix $\mathbf{F}^{(0)}$ is then evaluated. Then the matrix $\mathbf{F}^{\lambda(0)}$ is obtained using (2.26). Diagonalization of $\mathbf{F}^{\lambda(0)}$ gives $\mathbf{C}^{\lambda(1)}$ and $\epsilon^{(1)}$. Using (2.26) a new coefficient matrix $\mathbf{C}^{(1)}$ and thus the density matrix $\mathbf{P}^{(1)}$ can be obtained from $\mathbf{C}^{\lambda(1)}$. This procedure will be continued, with the evaluation of the new $\mathbf{F}^{(n)}$, $\mathbf{F}^{\lambda(n)}$, its eigenvalues and eigenvectors $\mathbf{C}^{\lambda(n+1)}$ until the density matrix elements of the new step differ by a predefined convergence threshold from the previous step.

For closed-shell systems, electrons of opposite spins occupy pairwise the same spatial orbital. The corresponding Hartree-Fock wavefunction is called restricted Hartree-Fock (RHF) wavefunction. There are two methods available for the treatment of open-shell systems, the restricted open-shell Hartree-Fock (ROHF) method and the unrestricted Hartree-Fock (UHF) method. In the ROHF approach the wavefunction is divided into a closed-shell and an open-shell part. In the closed-shell part the electrons are given pairwise the same spatial orbital function [8]. In a UHF wavefunction, the electrons of α and β spin are allowed to have different spatial orbitals [9]. A problem connected with the UHF method is that the resulting wavefunction generally does not correspond to a pure spin state.

2.2 Semiempirical Methods

Semiempirical methods are simplified versions of the Hartree-Fock (HF) method. Approaches that are based on the HF SCF procedure without additional approximation are called *ab initio* methods. *Ab initio* methods are very computer-time and -memory consuming. The number of basis functions must be much larger than the number of electrons. Furthermore, the evaluation of Fock matrix elements (2.21) requires computation of multi-center integrals, whose number increases with m^4 , where m is the number of basis functions. Limited basis sets do not have enough flexibility to repro-

duce the physics of the system and can give inaccurate results. The computational expense is reduced by making additional approximations in semiempirical methods. The following features are common for semiempirical methods,

- In semiempirical methods, atomic inner and valence electrons are separated. Only valence electrons are treated explicitly. For example, for C ($1s^2 2s^2 2p^2$): $1s$ =core electrons and $2s 2p$ =valence electrons, only the four electrons in the $2s 2p$ shell are taken into account.
- They use minimal basis sets, usually of Slater-type s , p , and sometimes d orbitals. Some recent semiempirical methods, such as, Semi-Ab-initio Model 1 (SAM1) [10], use standard STO-3G Gaussian basis set to evaluate the electron repulsion integrals.
- All the three- and four-center two-electron integrals are neglected, two-center two-electron integrals are partly calculated, whereas, two-center one-electron integrals are replaced by empirical formulas. Most of the empirical formulas are extensions of the Wolfsberg-Helmholtz formula [11], where the two-center one-electron integrals $H_{\mu\nu}$ are expressed as,

$$H_{\mu\nu} = \frac{1}{2} K S_{\mu\nu} (h_{\mu\mu} + h_{\nu\nu}) \quad (2.27)$$

Here K is an adjustable parameter or empirical function with several parameters which are optimized to reproduce experimental properties.

Semiempirical methods mainly differ in the way two-electron integrals are approximated. All existing methods are based on the zero-differential overlap (ZDO) approximation [3]. In this approximation, the overlap between pairs of different orbitals is set to zero for all volume elements $d\tau$:

$$\phi_\mu \phi_\nu d\tau = 0 \quad (2.28)$$

This directly leads to the following result for the overlap integrals,

$$S_{\mu\nu} = \delta_{\mu\nu} \quad (2.29)$$

According to this approximation, two-electron integrals $(\mu\nu | \rho\sigma)$ will vanish if $\mu \neq \nu$ or if $\rho \neq \sigma$, which can be expressed as,

$$(\mu\nu | \rho\sigma) = (\mu\mu | \rho\rho) \delta_{\mu\nu} \delta_{\rho\sigma} \quad (2.30)$$

On the basis of the ZDO approximation at different levels, there are several semiempirical methods, such as, CNDO (Complete Neglect of Differential Overlap) [12], INDO (Intermediate Neglect of Differential Overlap) [13], NDDO (Neglect of Diatomic Differential Overlap) [12]. The CNDO method uses the ZDO approximation (2.28) for all pairs of AOs. Thus, $S_{\mu\nu} = \delta_{\mu\nu}$ and $(\mu\nu | \rho\sigma) = (\mu\mu | \rho\rho)\delta_{\mu\nu}\delta_{\rho\sigma}$. In order to overcome the problems of rotational invariance, the two-electron integrals $(\mu\mu | \rho\rho)$ are set equal to parameter γ_{AB} where μ and ρ are on different atoms A and B, and to parameter γ_{AA} where μ and ρ are on atom A. γ_{AB} is the average electrostatic repulsion between an electron on atom A and an electron on atom B whereas γ_{AA} represents the average electron-electron repulsion between two electrons on an atom A. The INDO method is an improvement on CNDO. At the INDO level differential overlap between AOs on the same atom is not neglected in one-center electron-repulsion integrals, but is still neglected in two-center electron-repulsion integrals. Thus one-center integrals of the form $(\mu_A\mu_A|\mu_A\mu_A)$, $(\mu_A\mu_A|\nu_A\nu_A)$ and $(\mu_A\nu_A|\mu_A\nu_A)$ are retained. The ZDO approximation is also applied to potential terms of the one-electron integrals. The INDO method gives an improvement over CNDO results, especially where electron spin distribution is important. The NDDO method is an improvement on INDO in which differential overlap is neglected only between AOs centered on different atoms. Thus, all of the two-center two-electron integrals of the form $(\mu_A\nu_A | \rho_B\sigma_B)$ are retained.

In many cases semiempirical methods are able to reproduce experimental data with similar accuracy as *ab initio* methods at much lower computational cost. In the present work large and complex systems are investigated. For this reason the semiempirical method MSINDO was used for the calculations.

MSINDO (Modified Symmetrically orthogonalized Intermediate Neglect of Differential Overlap) [14] is a modified version of the semiempirical SCF molecular orbital method SINDO1 [15] based on the INDO formalism by Pople *et al.* [13].

In MSINDO, the ZDO approximation is justified by an approximate Löwdin transformation to the orthogonalized basis [16]. For the atoms in the second and the third row with $3d$ orbitals, additional one-center hybrid integrals of the form $(\mu_A\nu_A|\rho_A\sigma_A)$ are taken into account in order to preserve rotational invariance [17]. MSINDO uses a pseudominimal basis set of Slater-type valence atomic orbitals and takes into account the core electrons by Zerner's pseudopotential [18]. Thus $\{1s\}$ orbitals for H, $\{2s, 2p\}$

for first row elements, $\{3s, 3p\}$ for Na and Mg, $\{3s, 3p, 3d\}$ for Al-Cl, $\{4s, 4p\}$ for K and Ca, $\{3d, 4s, 4p\}$ for Sc to Zn and $\{4s, 4p, 4d\}$ for Ga to Br, are considered explicitly. In order to describe hydrogen bonding, an additional set of $2p$ orbitals can be introduced on hydrogen.

Using nonorthogonal basis functions, one-center elements of the core matrix \mathbf{H} are given by,

$$\begin{aligned}
 H_{\mu_A\mu_A} &= U_{\mu_A} + \sum_{B \neq A} (V_{\mu_A\mu_A}^B + V_{\mu_A\mu_A}^{B,\text{corr}}) - \sum_{B \neq A} \sum_{\rho_B} S_{\mu_A\rho_B}^2 \epsilon_{\rho_B} \quad (2.31) \\
 H_{\mu_A\nu_A} &= \sum_{B \neq A} (V_{\mu_A\nu_A}^B + V_{\mu_A\nu_A}^{B,\text{corr}}) - \sum_{B \neq A} \sum_{\rho_B} S_{\mu_A\rho_B} S_{\nu_A\rho_B} \epsilon_{\rho_B} \\
 \text{where } U_{\mu_A} &= \left\langle \mu_A \left| -\frac{1}{2}\nabla^2 - \frac{Z_A}{r_A} \right| \mu_A \right\rangle \\
 V_{\mu_A\nu_A}^B &= \left\langle \mu_A \left| -\frac{Z_B}{r_B} \right| \nu_A \right\rangle \\
 V_{\mu_A\mu_A}^{B,\text{corr}} &= \sum_{\nu_B} n_{\nu_B} \left\langle \mu_A \left| \hat{J}_{\nu_B} - \hat{J}_{\nu_B}^s \right| \mu_A \right\rangle \\
 &= \sum_{\nu_B} n_{\nu_B} [(\mu_A\mu_A|\nu_B^s\nu_B^s) - (\mu_A^s\mu_A^s|\nu_B^s\nu_B^s)]
 \end{aligned}$$

Here U_{μ_A} are determined from average energies of atomic configurations. $V^{B,\text{corr}}$ is a directional correction term which partially compensates the neglect of directional effects in the two-center Coulomb integrals. ν_B is a valence orbital at center B and n_{ν_B} is its atomic occupation number. μ_A^s and ν_B^s are treated like s orbitals. \hat{J}_{ν_B} and $\hat{J}_{\nu_B}^s$ are Coulomb operators. Only the atomic orbital ν_B is taken as an s orbital in \hat{J}_{ν_B} , while all orbitals are taken as s orbitals for the evaluation of $\hat{J}_{\nu_B}^s$. The last term in (2.31) is Zerner's pseudopotential which takes care of the inner orbitals ρ_B . ϵ_{ρ_B} is the energy of the core orbital ρ_B , as obtained from experimental spectra. A modified Mulliken approximation is used for calculating the two-center core integrals with a correction term, $L_{\mu_A\nu_B}$ [19].

$$H_{\mu_A\nu_B} = \frac{1}{2} S_{\mu_A\nu_B} (H_{\mu_A\mu_A} + H_{\nu_B\nu_B}) + L_{\mu_A\nu_B} \quad (2.32)$$

The correction term $L_{\mu_A\nu_B}$ has the form

$$\begin{aligned}
 L_{\mu_A\nu_B} &= -\frac{1}{2} (\zeta_{\mu_A}^2 + \zeta_{\nu_B}^2) \frac{S_{\mu_A\nu_B} (1 - |S_{\mu_A\nu_B}|)}{1 + \rho} \quad (2.33) \\
 \text{where } \rho &= \frac{1}{2} (\zeta_{\mu_A} + \zeta_{\nu_B}) R_{AB}
 \end{aligned}$$

Here the ζ 's are the orbital exponents. Two-center two-electron integrals are evaluated analytically over s -functions. The Fock-matrix elements are given by

$$\begin{aligned}
 F_{\mu_A\mu_A} &= H_{\mu_A\mu_A} + \sum_{\rho_A} \sum_{\sigma_A} P_{\rho_A\sigma_A} \left[(\mu_A\mu_A|\rho_A\sigma_A) - \frac{1}{2} (\mu_A\sigma_A|\rho_A\mu_A) \right] \\
 &\quad + \sum_{B \neq A} \sum_{\nu_B} P_{\rho_B\rho_B} (\mu_A\mu_A|\nu_B\nu_B) \\
 F_{\mu_A\nu_A} &= H_{\mu_A\nu_A} + \sum_{\rho_A} \sum_{\sigma_A} P_{\rho_A\sigma_A} \left[(\mu_A\nu_A|\rho_A\sigma_A) - \frac{1}{2} (\mu_A\sigma_A|\rho_A\nu_A) \right] \\
 F_{\mu_A\nu_B} &= H_{\mu_A\nu_B} - \frac{1}{2} P_{\mu_A\nu_B} (\mu_A\mu_A|\nu_B\nu_B)
 \end{aligned} \tag{2.34}$$

The core matrix is transformed to the orthogonalized basis by an approximate Löwdin procedure.

$$\mathbf{H}^\lambda = \mathbf{S}^{-1/2} \mathbf{H} \mathbf{S}^{-1/2} \tag{2.35}$$

$\mathbf{S}^{-1/2}$ is expanded in a Taylor series.

$$\begin{aligned}
 \mathbf{S}^{-1/2} &= (\mathbf{1} + \bar{\mathbf{S}})^{-1/2} \\
 &= \mathbf{1} - \frac{1}{2} \bar{\mathbf{S}} + \frac{3}{8} \bar{\mathbf{S}}^2 - \frac{5}{16} \bar{\mathbf{S}}^3 + \dots
 \end{aligned} \tag{2.36}$$

Here $\bar{\mathbf{S}}$ is the overlap matrix with zero diagonal elements. \mathbf{H}^λ is approximated in the overlap expansion, to second order in SINDO1, but only to first order in MSINDO. The latter avoids problems connected with large overlap integrals. The core matrix elements in orthogonal basis take the following form [14].

$$\begin{aligned}
 H_{\mu_A\mu_A}^\lambda &= H_{\mu_A\mu_A} - f^{B,\text{orth}} \sum_{B \neq A} \sum_{\rho_B} S_{\mu_A\rho_B} L_{\mu_A\rho_B} \\
 H_{\mu_A\nu_A}^\lambda &= H_{\mu_A\nu_A} - \frac{1}{2} f^{B,\text{orth}} \sum_{B \neq A} \sum_{\rho_B} (L_{\mu_A\rho_B} S_{\rho_B\nu_A} + S_{\mu_A\rho_B} L_{\rho_B\nu_A}) \\
 H_{\mu_A\nu_B}^\lambda &= L_{\mu_A\nu_B} + H_{\mu_A\nu_B}^{\text{corr}}
 \end{aligned} \tag{2.37}$$

Here $f^{B,\text{orth}}$ is a correction factor which compensates the different numbers of basis functions used for the elements and partially the neglect of higher order terms in (2.36). $H_{\mu_A\nu_B}^{\text{corr}}$ is an empirical correction term given by

$$H_{\mu_A\nu_B}^{\text{corr}} = \frac{1}{4} (K_A + K_B) S_{\mu_A\nu_B} (f_A h_{\mu_A\mu_A} + f_B h_{\nu_B\nu_B}) \tag{2.38}$$

$$\text{with } f_A = 1 - \exp(-\kappa_{P_B}(A) R_{AB})$$

$$f_B = 1 - \exp(-\kappa_{P_A}(B) R_{AB})$$

The K 's here in this equation are adjustable parameters depending only on the atomic number and the orbital symmetry in a local diatomic coordinate system. The κ 's are atomic parameters of interperiodic nature. MSINDO has been parametrized for the elements H, Li-F, Na-Cl and K-Br [20–22].

Special techniques like an embedding procedure [23] and the cyclic cluster model [24] for the description of solids and surfaces have been developed and incorporated in MSINDO. The method has been successfully applied to various solid state problems such as properties of crystalline solids [25], adsorption on surfaces [26] and surface reactions [27].

2.3 Density Functional Theory

The basic idea of density functional theory (DFT) is that the ground-state energy of a system is a functional of electron density ρ [1,28,29] which can be written as $E_0 = E[\rho]$. Integration of ρ over all space gives the total number of electrons n , i.e.,

$$n = \int \rho(\mathbf{r}) d\mathbf{r} \quad (2.39)$$

With the introduction of an external potential v_{ext} , the electronic Hamiltonian operator (2.3) has the following form

$$\hat{H}_{\text{el}} = -\sum_i^n \frac{1}{2} \nabla_i^2 + v_{\text{ext}}(\mathbf{r}) + \sum_{j>i}^n \frac{1}{r_{ij}} \quad (2.40)$$

where

$$v_{\text{ext}}(\mathbf{r}) = -\sum_i^n \sum_I^N \frac{Z_I}{r_{iI}} \quad (2.41)$$

According to the first Hohenberg-Kohn theorem [28,30], the external potential v_{ext} can be obtained from the electron density ρ . Since ρ determines n and v_{ext} , it follows that ρ also determines the ground-state wave function $\Psi[\rho]$ and hence all other electronic properties of the system. The total energy $E[\rho]$ can be expressed as

$$E[\rho] = F_{HK}[\rho] + \int \rho(\mathbf{r}) v_{\text{ext}}(\mathbf{r}) d\mathbf{r} \quad (2.42)$$

with

$$F_{HK}[\rho] = T[\rho] + V_{ee}[\rho] \quad (2.43)$$

The functional $F_{HK}[\rho]$ is a universal functional of ρ ; this means that $F_{HK}[\rho]$ is defined independently from the external potential v_{ext} . $T[\rho]$ is the kinetic energy functional of the system, $V_{ee}[\rho]$ is the potential energy functional for the classical electron-electron repulsion. Hohenberg and Kohn showed in a second theorem [30] that the electron density obeys a variational principle. The energy expectation value can be obtained as

$$\begin{aligned} E[\rho] &= \langle \Psi[\rho] | \hat{H} | \Psi[\rho] \rangle \\ &\geq E_0 \end{aligned} \quad (2.44)$$

which, by the variational principle similar to MO theory, must be greater than or equal to the true ground-state energy E_0 . However, Hohenberg-Kohn theorem does not show how to find ρ without first finding Ψ and there is no simplification over MO theory, since the final step is still the solution of the Schrödinger equation, and this is prohibitively difficult in most instances. The difficulty arises from the electron-electron interaction term in the Hamiltonian. In analogy to the universal functional $F_{HK}[\rho]$, Kohn and Sham [31] introduced a corresponding *noninteracting reference system*. The Kohn-Sham one-electron operator \hat{H}_{KS} is defined as,

$$\hat{H}_{KS} = -\frac{1}{2}\nabla^2 - \sum_I \frac{Z_I}{r_{Ii}} + \int \frac{\rho(\mathbf{r}_2)}{r_{12}} d\mathbf{r}_2 + v_{\text{xc}}[\rho] \quad (2.45)$$

Here $v_{\text{xc}}[\rho]$ is called the exchange-correlation potential which is found as the functional derivative of exchange-correlation energy $E_{\text{xc}}[\rho(\mathbf{r})]$, $v_{\text{xc}}[\rho] = \frac{\delta E_{\text{xc}}[\rho(\mathbf{r})]}{\delta \rho(\mathbf{r})}$. $E_{\text{xc}}[\rho(\mathbf{r})]$ will be discussed below.

A set of orbitals $\{\psi_i(\mathbf{r})\}$ is introduced, which are called Kohn-Sham orbitals. This leads to a set of eigenvalue equations,

$$\hat{H}_{KS}\psi_i = \epsilon_i\psi_i \quad \text{with} \quad (i = 1, \dots, n) \quad (2.46)$$

The use of the Kohn-Sham orbitals $\{\psi_i(\mathbf{r})\}$ enables to optimize the energy by solving the set of one-electron equations (2.46) self-consistently similar to the Hartree Fock equations.

Kohn and Sham also showed that the exact ground-state electron density ρ can be obtained from $\{\psi_i\}$, according to,

$$\rho = \sum_i^n |\psi_i|^2 \quad (2.47)$$

If the kinetic energy of the reference system is defined as $T_{KS}[\rho]$, the energy functional can be expressed as,

$$E[\rho] = T_{KS}[\rho] + \int \rho(\mathbf{r}) v_{\text{ext}}(\mathbf{r}) d\mathbf{r} + J[\rho] + E_{xc}[\rho(\mathbf{r})] \quad (2.48)$$

where $J[\rho]$ denotes the classical electron-electron repulsion

$$J[\rho] = \frac{1}{2} \iint \frac{\rho(\mathbf{r}_1)\rho(\mathbf{r}_2)}{r_{12}} d\mathbf{r}_1 d\mathbf{r}_2 \quad (2.49)$$

and the exchange-correlation energy, $E_{xc}[\rho(\mathbf{r})]$ includes not only the effects of quantum mechanical exchange and correlation, but also the correction for the classical self-interaction energy and for the difference in kinetic energy between the fictitious non-interacting system and the real system.

The main task associated with the Kohn-Sham equations is to find the correct functional $E_{xc}[\rho(\mathbf{r})]$. Various approximate $E_{xc}[\rho(\mathbf{r})]$ have been used in molecular DF calculations. The simplest approximation is represented by the local density approximation (LDA), where $E_{xc}[\rho(\mathbf{r})]$ is expressed as,

$$E_{xc}^{LDA}[\rho(\mathbf{r})] = \int \rho(\mathbf{r}) \epsilon_{xc}[\rho(\mathbf{r})] d\mathbf{r} \quad (2.50)$$

The value of ϵ_{xc} at some position \mathbf{r} is computed exclusively from the value of ρ at that position. In practice, $\epsilon_{xc}[\rho(\mathbf{r})]$ describes the exchange and correlation energy per particle of a uniform electron gas [32] of density ρ . The corresponding exchange-correlation potential becomes,

$$v_{xc}^{LDA}(\mathbf{r}) = \epsilon_{xc}[\rho(\mathbf{r})] + \rho(\mathbf{r}) \frac{\delta \epsilon_{xc}[\rho(\mathbf{r})]}{\delta \rho} \quad (2.51)$$

In a molecular system, the electron density is in general rather far from being spatially uniform which limits the applicability of LDA. A further advancement was obtained by the inclusion of a density gradient correction which is known as the generalized gradient approximation (GGA). In the GGA, the functionals depend on both the density and the gradient of the density, i.e., $v_{xc}^{\text{GGA}} = f(\rho, \nabla\rho)$. Popular examples of GGA functionals are Perdew-Wang GGA or PWGGA (both exchange and correlation) [33] and Becke-Lee-Yang-Parr or BLYP where B stands for the Becke GGA exchange functional [34] and LYP stands for the Lee-Yang-Parr GGA correlation functional [35]. Functionals having higher derivatives of density are called *meta*-GGA functionals.

Still the GGA functionals have problems with self interaction. Hybrid DFT functionals usually offer some improvement over corresponding pure DFT functionals. They contain a certain percentage of the exact HF exchange. In several approaches, the amount of HF contribution is determined empirically by error minimization with respect to experimental data. Of all modern functionals, the B3LYP method [35, 36] is the most popular to date. It works satisfactorily both for structural investigations and also for the computation of electronic properties [29]. The name of the functional, B3LYP, implies its use of Becke's three-parameter functional [36] as GGA exchange functional together with the GGA correlation functional LYP [35]. The functional contains 20 % HF exchange as optimized for heats of formation of small molecules. In the more recent hybrid functional PW1PW [37], the exchange functional is a linear combination of the HF expression (20 %) and the PWGGA exchange functional (80 %) which is combined with the PWGGA correlation functional [33]. This approach was parameterized to reproduce structural, energetic and electronic properties of solids [37].

The molecular orbitals in DFT are usually a linear combination of atomic basis functions which can be represented by Gaussian functions, Slater orbitals or as numerical orbitals. Another possibility is the use of plane waves as basis set for periodic infinite systems. They will be discussed in detail in the next chapter.

3 Models of Solids and Surfaces

An ideal crystal is constructed by the infinite repetition of identical structural units in space [38]. The structure of all crystals can be described in terms of a lattice, with a group of atoms attached to every lattice point. The group of atoms is called the basis; when repeated in space it forms the crystal structure. The lattice is defined by three fundamental translation vectors \mathbf{a}_1 , \mathbf{a}_2 , and \mathbf{a}_3 . A lattice translation operation is defined as the displacement of a crystal by a translation vector \mathbf{T} with integral components n_i of the fundamental vectors. The environment of a lattice point does not change and the lattice is invariant under such a transformation.

$$\mathbf{T} = n_1\mathbf{a}_1 + n_2\mathbf{a}_2 + n_3\mathbf{a}_3 \quad (3.52)$$

The coordinates of the atoms of the basis relative to a lattice point are indicated by fractional coordinates concerning the lattice vectors.

$$\mathbf{r}_i = x_i\mathbf{a}_1 + y_i\mathbf{a}_2 + z_i\mathbf{a}_3 \quad \text{with} \quad 0 \leq x_i, y_i, z_i \leq 1$$

The basic module of the solid body is the unit cell. Its choice is arbitrary in principle, as long as it fills out the space by translation. The cell with smallest possible volume V_a ,

$$V_a = |(\mathbf{a}_1 \times \mathbf{a}_2) \cdot \mathbf{a}_3| \quad (3.53)$$

is called primitive unit cell (PUC). The basis associated with a primitive cell is called a primitive basis. No basis contains fewer atoms than a primitive basis contains. A special form of the PUC is the primitive Wigner-Seitz cell (WSZ). The Wigner-Seitz cell around a lattice point is the region of space that is closer to that point than to any other lattice point. WSZ will be as symmetrical as the Bravais lattice. An example of a WSZ of a two-dimensional, hexagonal lattice is illustrated in Fig 3.1.

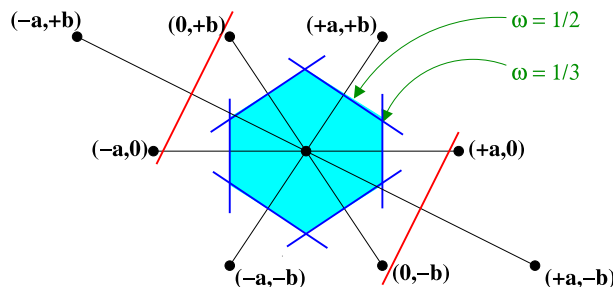


Figure 3.1: A two-dimensional Wigner-Seitz cell, hexagonal lattice

In the context of this work two models are used for the description of solids and surfaces, which are described briefly in the following. These are called the periodic models and the cyclic cluster model (CCM).

3.1 Periodic Models

Periodic models are particularly suitable for the description of ideal crystalline solids. They use the symmetry characteristics of crystals. The periodic models consist of primitive unit cells or supercells which are then replicated periodically. Thus periodic models are infinite models whose basic unit contains a finite number of atoms. The translation vectors are the lattice parameters of the real system. The periodic models or supercell models can be explained by the Bloch theorem [39].

Let \hat{T} be a translation operator, associated with the lattice vector \mathbf{T} (3.52), that satisfies the argument of any function as follows,

$$\hat{T}\hat{H}(\mathbf{r})\psi(\mathbf{r}) = \hat{H}(\mathbf{r} + \mathbf{T})\psi(\mathbf{r} + \mathbf{T}) = \hat{H}(\mathbf{r})\hat{T}\psi(\mathbf{r}) \quad (3.54)$$

Due to the periodicity of the crystal the associated Hamiltonian operator \hat{H} also follows the periodic nature, i.e., the kinetic energy operator is invariant to any translation, the potential operator, \hat{V} , is periodic by hypothesis. \hat{H} commutes with \hat{T} , and thus, the eigenfunctions of \hat{H} are also the eigenfunctions of \hat{T} .

$$\hat{T}\psi(\mathbf{r}) = \exp(i\mathbf{k} \cdot \mathbf{T})\psi(\mathbf{r}) \quad (3.55)$$

The equation (3.55) is known as Bloch theorem. Here $\mathbf{k} = k_1\mathbf{b}_1 + k_2\mathbf{b}_2 + k_3\mathbf{b}_3$ is called the reciprocal lattice vector (k_1, k_2 and k_3 are integers) and \mathbf{b}_i are the primitive vectors of reciprocal lattice \mathbf{b}_i which can be expressed as,

$$\mathbf{b}_i = 2\pi \frac{\mathbf{a}_j \times \mathbf{a}_k}{\mathbf{a}_i \cdot (\mathbf{a}_j \times \mathbf{a}_k)} \quad \text{with} \quad (i, j, k \in 1, 2, 3) \quad (3.56)$$

Each vector defined by Eq. (3.56) is orthogonal to two axis vectors of the crystal lattice. Thus $\{\mathbf{a}_i\}$ and $\{\mathbf{b}_i\}$ are related by

$$\mathbf{a}_i \cdot \mathbf{b}_j = 2\pi\delta_{ij} \quad (3.57)$$

\mathbf{k} and \mathbf{T} are linked as,

$$\mathbf{k} \cdot \mathbf{T} = 2\pi \sum_{i=1}^3 k_i n_i \quad (3.58)$$

The primitive WSZ in the reciprocal space is called the first Brillouin-Zone (BZ).

By imposing an appropriate boundary condition, the crystal system is considered as a finite but macroscopic system containing $N = N_1 \times N_2 \times N_3$ unit cells. The unit cell repeats itself infinitely in all three translation directions \mathbf{a}_1 , \mathbf{a}_2 and \mathbf{a}_3 . Thus the usual assumption is that the finite crystal is part of an infinite crystal, and it is delimited in a purely formal way. These appropriate boundary conditions to the orbitals are called *Born-Von Karman or periodic boundary* conditions [40]. According to these conditions, the Bloch function obeys the following condition,

$$\psi(\mathbf{r} + N_j \mathbf{a}_j) = \exp(iN_j \mathbf{k} \cdot \mathbf{a}_j) \psi(\mathbf{r}) = \psi(\mathbf{r}) \quad (3.59)$$

which implies:

$$\exp(iN_j \mathbf{k} \cdot \mathbf{a}_j) = 1$$

which is satisfied if,

$$k_j = \frac{l_j}{N_j} \quad \text{with} \quad l_j, N_j \in \mathbb{N} \quad \text{and} \quad k_j \in \mathbb{R}$$

The above equation shows that, because of the periodic boundary conditions, vectors \mathbf{k} are real. The general $\boldsymbol{\kappa}$ vector inside the reciprocal unit cell (first BZ) is defined as,

$$\boldsymbol{\kappa} = \frac{n_1 \mathbf{b}_1}{N_1} + \frac{n_2 \mathbf{b}_2}{N_2} + \frac{n_3 \mathbf{b}_3}{N_3} \quad \text{with} \quad n_i \in \mathbb{N} < N_i \quad (3.60)$$

Different eigenfunctions can satisfy the Bloch theorem for the same $\boldsymbol{\kappa}$ value. Thus the eigenvectors of Hamiltonian are also labelled with an n index as $\psi_n^{\boldsymbol{\kappa}}(\mathbf{r})$. The number of $\boldsymbol{\kappa}$ points is N , i.e., the number of cells in the crystal. As the crystal size increases, the $\boldsymbol{\kappa}$ points get closer and closer. At the limit of an infinite lattice, $\boldsymbol{\kappa}$ becomes continuous and can take on all possible values within the BZ [40].

Similar to LCAO, the unknown single-particle crystalline wavefunction $\psi_n^{\boldsymbol{\kappa}}(\mathbf{r})$, is expanded in a finite set of Bloch-functions (BFs) $\chi_\mu^{\boldsymbol{\kappa}}(\mathbf{r})$ as following,

$$\psi_n^{\boldsymbol{\kappa}}(\mathbf{r}) = \sum_{\mu} c_{\mu n}^{\boldsymbol{\kappa}} \chi_\mu^{\boldsymbol{\kappa}}(\mathbf{r}) \quad (3.61)$$

The coefficients, $c_{\mu n}^{\boldsymbol{\kappa}}$ are determined variationally by solving the set of coupled matrix equations:

$$\mathbf{H}^{\boldsymbol{\kappa}} \mathbf{C}^{\boldsymbol{\kappa}} = \mathbf{S}^{\boldsymbol{\kappa}} \mathbf{C}^{\boldsymbol{\kappa}} \mathbf{E}^{\boldsymbol{\kappa}} \quad (3.62)$$

$$(\mathbf{C}^{\boldsymbol{\kappa}})^\dagger \mathbf{S}^{\boldsymbol{\kappa}} \mathbf{C}^{\boldsymbol{\kappa}} = \mathbf{I}$$

where \mathbf{H}^κ is the Hamiltonian matrix in the basis set of the $\chi_\mu^\kappa(\mathbf{r})$ functions; \mathbf{S}^κ is the overlap matrix among these functions ($\mathbf{S}^\kappa = \mathbf{I}$ if the basis functions are orthogonal); \mathbf{C}^κ is the matrix of the coefficients, $c_{\mu n}^\kappa$; and \mathbf{E}^κ is the diagonal matrix of the single particle eigenvalues, ϵ_n^κ . The above procedure should be carried on for the complete set of κ points in the first BZ, so as to determine the complete set of crystalline wave functions ($\psi_n^\kappa(\mathbf{r})$). For each n , the set of electronic levels specified by ϵ_n^κ is called an energy band. Since each ϵ_n^κ is periodic in κ and continuous, it has an upper and lower bound, so that all the levels ϵ_n^κ lie in the band of energies between these limits. In a closed shell system, each energy band can allocate $2 * N$ (N is the number of cells) electrons. If there are n electrons in the unit cell, and the bands do not cross, the lowest $n/2$ bands are occupied and are separated from the empty bands. However, if n is odd, or if the valence bands cross, more than $n/2$ bands are partially occupied. At each cycle of the SCF process, the Fermi energy ϵ_F must be determined, such that the number of one electron levels with energy below ϵ_F is equal to the number of electrons. The Fermi surface is the surface in the reciprocal space, which satisfies the condition $\epsilon_n^\kappa = \epsilon_F$.

Two basic types of BFs are used for the expansion of (3.61), these are, localized basis and plane wave basis.

3.1.1 Localized basis

One possibility to represent the Bloch functions $\chi_\mu^\kappa(\mathbf{r})$ is to use local atom-centered functions $\{\chi_\mu\}$.

$$\chi_\mu^\kappa(\mathbf{r}) = \sum_{\mathbf{T}} \exp(i\kappa \cdot \mathbf{T}) \chi_\mu(\mathbf{r} - \mathbf{A} - \mathbf{T}) \quad (3.63)$$

where μ labels the AOs in the unit cell, and \mathbf{A} denotes the coordinate of the nucleus in the zero reference cell on which the local function $\{\chi_\mu\}$ is centered and the summation is extended to the set of all lattice vectors \mathbf{T} . The local functions $\{\chi_\mu\}$ are expressed as CGTFs (2.18). Substituting the AOs $\chi_\mu^\kappa(\mathbf{r})$ in eq (3.61), the crystalline orbital $\psi_n^\kappa(\mathbf{r})$ has the following form,

$$\psi_n^\kappa(\mathbf{r}) = \sum_{\mu} c_{\mu n}^\kappa \chi_\mu^\kappa(\mathbf{r}) \quad (3.64)$$

The atomic orbital based Bloch functions can be applied to HF and DFT calculations. This is realized e.g. in the crystalline orbital program CRYSTAL03 [41]. This program

is used in this study.

The localized basis is characterized by the following advantages and disadvantages:

- (+) The electronic distributions in both the valence and the core region are described accurately by relatively small numbers of GTFs.
- (+) Isolated atoms, molecules and defects are described easily.
- (+) The Fourier transform of GTFs is another Gaussian, $F_p\{\exp(-\alpha r^2)\} \propto \exp(-p^2/4\alpha)$.
- (-) A reasonable description of delocalized electrons (metallic systems) is very expensive and, in some cases, difficult, due to problems related to the non-orthogonal nature of the basis functions.
- (-) It requires to take into account the basis set superposition error (BSSE) [42, 43].
- (-) It poses the risk of pseudo-linear-dependence catastrophes when too diffuse functions are used.

An alternative way to construct the Bloch functions is represented by plane wave (PW) basis.

3.1.2 Plane Wave basis

Plane waves (PWs) for a periodic system can be expressed as [44],

$$\chi_{\mathbf{K}_n}^{\boldsymbol{\kappa}}(\mathbf{r}) = \frac{1}{\sqrt{NV_a}} \exp(i\mathbf{r} \cdot (\boldsymbol{\kappa} + \mathbf{K}_n)) \quad (3.65)$$

with $N = N_1 N_2 N_3$

where \mathbf{K}_n denotes a reciprocal lattice vector and V_a denotes the volume of the primitive unit cell (3.53). The crystalline orbital $\psi_i^{\boldsymbol{\kappa}}(\mathbf{r})$ is expressed as a linear combination of PWs,

$$\psi_i^{\boldsymbol{\kappa}}(\mathbf{r}) = \sum_n^m c_{in}^{\boldsymbol{\kappa}}(\mathbf{K}_n) \chi_{\mathbf{K}_n}^{\boldsymbol{\kappa}}(\mathbf{r}) \quad (3.66)$$

where the number m is independent from the kind, position and number of atoms in the PUC. Rather, it is determined by the kinetic energy cutoff, E_{cut} .

$$(\boldsymbol{\kappa} + \mathbf{K}_n)^2 \leq E_{cut} \quad (3.67)$$

The larger the energy cutoff E_{cut} , the more accurate is the wavefunction representation. A large number of PWs is required to represent accurately localized features of the wave functions that arise from the low-energy core orbitals or from other orbitals undergoing rapid oscillations close to the nucleus. One would need PW basis sets which are several orders of magnitude larger than Gaussian basis sets to obtain the same accuracy [45]. The concept of pseudopotentials (PPs) provides an elegant solution to such limitations of PW basis sets. The plane wave program VASP [46–48] uses three different types of potentials, these are, norm-conserving (NC) PPs [49, 50], ultra-soft (US) PPs [51, 52] and Projector Augmented Wave (PAW) [53, 55] potentials. In the present study the VASP program is used for part of calculations, applying the US pseudopotentials and PAW potentials for the core electron representation. The valence electrons are treated with plane wave sets with different energy cutoffs.

The pseudopotential approaches are called frozen-core approximation (FCA) [45]. The basic principle of PPs is the *pseudization* of the all-electron (AE) valence wave function. According to this principle, the AE valence orbital $|\psi_\nu\rangle$ is represented as a linear combination of a pseudo- (PS) wavefunction $|\phi_\nu\rangle$ and the core electron orbitals $|\psi_c\rangle$:

$$|\psi_\nu\rangle = |\phi_\nu\rangle + \sum_c \alpha_{c\nu} |\psi_c\rangle \quad (3.68)$$

The coefficients $\alpha_{c\nu}$ are determined by core-valence orthogonality (i.e., $\alpha_{c\nu} = -\langle\psi_c | \phi_\nu\rangle$). By using the fact that $|\psi_\nu\rangle$ and $|\psi_c\rangle$ are solutions of the Schrödinger equation with eigenvalues ϵ_ν and ϵ_c , respectively, one obtains the equation for PS wavefunction ($|\phi_\nu\rangle$) as,

$$\left[\hat{H} + \sum_c (\epsilon_\nu - \epsilon_c) |\psi_c\rangle \langle\psi_c| \right] |\phi_\nu\rangle = \epsilon_\nu |\phi_\nu\rangle \quad (3.69)$$

The US PP [51] approach is a modification of the NC PP [49, 50]. In the NC PP approach [49], inside some core radius, the AE wave function is replaced by a soft nodeless PS wave function. The crucial restriction is that the PS wave function must have the same norm as the AE wave function within the chosen core radius. Outside the core radius, the PS and AE wave functions are identical. However, it is now well established that good transferability requires a core radius around the outer-most maximum of the AE wave function, because only then the charge distribution and moments of the AE wave functions are well reproduced by the PS wave functions.

Therefore, for elements with strongly localized orbitals (like first-row, 3d, and rare-earth elements), the NC PP approach has proven impossible to construct a PS wave function which is much smoother than the AE one. One solution of this problem was proposed by Vanderbilt [51]. In the US PP method the norm-conservation constraint is relaxed and to make up for the resulting charge deficit, localized atom-centered augmentation charges are introduced. These augmentation charges are defined as the charge difference between the AE and PS wavefunctions, but for convenience, they are pseudized to allow an efficient treatment of the augmentation charges on a regular grid. The core radius of the pseudopotential can be chosen around the nearest distance - independent of the position of the maximum of the AE wavefunction. Only for the augmentation charges, a small cutoff radius must be used to restore the moments and the charge distribution of the AE wavefunction accurately. With these modifications, the US PP can be applicable for elements with strongly localized orbitals. The savings in the CPU time and improvements in the accuracy can be significant compared to the NC PP [54]. But the success of this method is partly hampered by the difficult construction of the PPs [53]. It requires many parameters (several cutoff radii) and therefore extensive tests are necessary in order to obtain an accurate and highly transferable PP. These disadvantages can be avoided in the PAW method [53,55].

In the PAW [55] method, a linear transformation, \mathcal{T} is defined that connects the PS wavefunctions, $\tilde{\Psi}$, and AE wavefunctions, Ψ , as, $\Psi = \mathcal{T}\tilde{\Psi}$. \mathcal{T} mainly concerns the regions of atomic cores and it can be seen as a sum of non-overlapping atom-centered contributions \mathcal{T}_R , where R denotes the atomic site. Each of \mathcal{T}_R acts within the corresponding augmentation region, such that $\mathcal{T} = 1 + \sum_R \mathcal{T}_R$. Introducing a set of projector functions $\langle \tilde{p}_i |$, the AE wave function can be obtained from the PS wavefunction by,

$$|\Psi\rangle = |\tilde{\Psi}\rangle + \sum_i (|\phi_i\rangle - |\tilde{\phi}_i\rangle) \langle \tilde{p}_i | \tilde{\Psi}\rangle \quad (3.70)$$

where $|\tilde{\Psi}\rangle = \sum_i |\tilde{\phi}_i\rangle c_i$

and $|\Psi\rangle = \sum_i |\phi_i\rangle c_i$

Here ϕ_i and $\tilde{\phi}_i$ denote the true and pseudo partial wave functions, respectively. Thus each augmentation region is associated to two sets of partial waves and a set of projector

functions. The set of the all-electron partial waves, ϕ_i , can be generated from numerical solutions of the radial Schrödinger equation, the pseudo partial waves, $\tilde{\phi}_i$, are taken by the techniques used in the pseudopotential approach and the projector functions \tilde{p}_i are orthogonal to the pseudo partial wave function, i.e., $\langle \tilde{p}_i | \tilde{\phi}_j \rangle = \delta_{ij}$.

The main difference between the PAW and US PP methods is that the PAW is an all electron method whereas the US PP approach is a pseudopotential method [55]. The comparisons between these two approaches are given as follows:

- The PAW method works directly with the full-wave functions and potentials and includes the core states. Whereas, the full-wave functions can not be treated in a reasonable way on a regular grid for the US PPs.
- In the PAW method, the non-norm-conserving PS wave functions enter naturally whereas, in the US PPs, the overlap operator and the local charges have been introduced to restore the scattering properties of the PPs.
- From the point of view of computational effort, the PAW method is more efficient.

The plane wave basis is characterized by the following advantages and disadvantages:

- (+) The calculation of the electron-electron interaction integrals in a plane wave basis is comparably simple.
- (+) They have a uniform grid of nodal surfaces, which is useful for the calculation and extrapolation of correlation energies.
- (+) The convergence of the total energy and related properties, as a function of the number of plane waves is very fast for metals.
- (−) Basis set is to be limited to a manageable size. It requires PPs for the localized inner electrons.
- (−) PW basis sets are necessarily much larger than the atomic (Gaussian) ones.
- (−) PWs are less appropriate to describe isolated atoms and molecules. They have to use periodic arrangements with huge lattice vectors.
- (−) Basis set convergence is very slow for ionic systems.

Periodic models are best suited for ordered bulk and surface structures. There are no boundary effects and moreover, long-range interactions are included in periodic models. They are less suitable for the description of local defects and non-periodic structures. The cyclic cluster model (CCM) is an alternative in such cases.

3.2 Cyclic Cluster Model

The cyclic cluster model (CCM) is obtained from the free cluster model (FCM) by introducing periodic boundary conditions. The FCM has some advantages, such as, it can be treated by all existing molecular orbital programs with high computational efficiency and it gives good description of local (non-periodic) effects. Disadvantages inherent in FCM are the loss of local symmetry for some sites, boundary effects due to the presence of low-coordinated cluster atoms, and the neglect of long range interactions, mainly of electrostatic nature. These deficiencies of the FCM are removed in the CCM [24]. It is similar to the quasi-molecular large-unit cell (QLUC) model [56]. In the CCM, the local environment of each cluster atom is replaced by that of a fictitious cyclic arrangement. In the following, a cyclic A_3B_3 cluster is used as a model for the one-dimensional periodic system AB. Conceptually, the atoms of the A_3B_3 cluster are treated as if they formed a ring (Fig. 3.2).

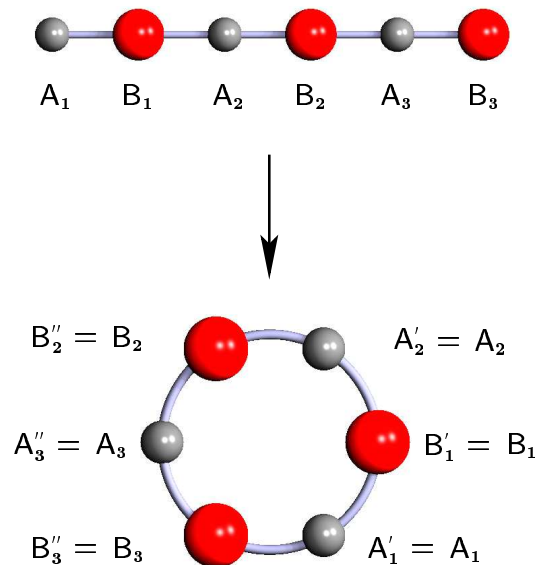


Figure 3.2: Fictitious arrangement of cluster atoms on a ring for the simulation of a linear crystal.

This fictitious arrangement would be a torus in two dimensions, and a hypertorus in three dimensions. In order to define the interaction region \mathcal{R} for every atom of the cyclic cluster, the cluster atoms are translated as follows,

$$\cdots A_2'' - B_2'' - A_3'' - B_3'' - A_1 - B_1 - A_2 - B_2 - A_3 - B_3 - A_1' - B_1' - A_2' - B_2' \cdots$$

$\xrightarrow{\mathbf{a}}$

Figure 3.3: Translation of the one-dimensional chain in CCM

Here a is the length of the translation vector. The single prime ($'$) denotes a translation in a positive x direction, and double prime ($''$) denotes the translation in negative x direction. Only interactions within the distance $r \leq a/2$ are taken into account. The interaction region is the region around an atom in which all the multi-center integrals containing the central atom are evaluated. It also defines the entries for interatomic matrix elements.

In the CCM approach [24] implemented in MSINDO, the atoms at the border of the interaction sphere are treated according to an idea of Evjen [57]. For a symmetric bulk system, there are always several neighbors at the borders of the Wigner-Seitz cell around the central atom I with the same distance. The MSINDO-CCM takes into account all of those atoms J and the interaction integrals are weighted with their reciprocal total number, ω_{IJ} . Thus ω_{IJ} will be $1/2$ for the integrals involving the border atoms in the present example (Fig. 3.2). The interaction matrix is given in Table 3.1.

Table 3.1: Weighted CCM interaction matrix for the linear chain $((AB)_3)$. Here I is a central atom and $\mathcal{R}(I)$ is its interaction region.

$\mathcal{R}(I)$			I	$\mathcal{R}(I)$		
$\frac{1}{2}B_2''$	A_3''	B_3''	A_1	B_1	A_2	$\frac{1}{2}B_2$
$\frac{1}{2}A_3''$	B_3''	A_1	B_1	A_2	B_2	$\frac{1}{2}A_3$
$\frac{1}{2}B_3''$	A_1	B_1	A_2	B_2	A_3	$\frac{1}{2}B_3$
$\frac{1}{2}A_1$	B_1	A_2	B_2	A_3	B_3	$\frac{1}{2}A_1'$
$\frac{1}{2}B_1$	A_2	B_2	A_3	B_3	A_1'	$\frac{1}{2}B_1'$
$\frac{1}{2}A_2$	B_2	A_3	B_3	A_1'	B_1'	$\frac{1}{2}A_2'$

Within the MSINDO-CCM, the one-center core Hamiltonian elements (2.31) are modified as

$$\begin{aligned}
 H_{\mu_A\mu_A} &= U_{\mu_A} + \sum_{B \neq A}^{\mathcal{R}(A)} \omega_{AB} (V_{\mu_A\mu_A}^B + V_{\mu_A\mu_A}^{B,\text{corr}}) - \sum_{B \neq A}^{\mathcal{R}(A)} \sum_{\rho_B} S_{\mu_A\rho_B}^2 \epsilon_{\rho_B} \\
 H_{\mu_A\nu_A} &= \sum_{B \neq A}^{\mathcal{R}(A)} \omega_{AB} (V_{\mu_A\nu_A}^B + V_{\mu_A\nu_A}^{B,\text{corr}}) - \sum_{B \neq A}^{\mathcal{R}(A)} \sum_{\rho_B} S_{\mu_A\rho_B} S_{\nu_A\rho_B} \epsilon_{\rho_B}
 \end{aligned} \tag{3.71}$$

where $\mathcal{R}(A)$ is the interaction region for an atom A of the cluster and ω_{AB} is the weighting factor. If ν belongs to an atom B which is not a border atom, the two-center terms $H_{\mu_A\nu_B}$ and Coulomb matrix elements $G_{\mu_A\nu_B}$ consist of single terms [24]. If ν is centered at atom B which is a border atom, $H_{\mu_A\nu_B}$ and $G_{\mu_A\nu_B}$ are calculated as weighted average over all equivalent border atoms B' , including the reference atom B as,

$$\begin{aligned}
 H_{\mu_A\nu_B} &= \sum_{B'}^{\text{equiv}} \omega_{AB'} H_{\mu_A\nu_{B'}} \\
 G_{\mu_A\nu_B} &= \sum_{B'}^{\text{equiv}} \omega_{AB'} G_{\mu_A\nu_{B'}}
 \end{aligned}$$

CCM calculations are performed in real space which corresponds to the $\kappa = 0$ approximation in the periodic models. Long-range electrostatic interactions can be approximately taken into account in CCM calculations by embedding in finite point charge arrays. But it is preferable to perform an infinite summation using the Ewald technique [58]. Analytical energy gradients for the atomic coordinates in the framework of CCM are also implemented in MSINDO [24, 58]. Numerical gradients are used for the cell vectors during lattice parameter optimizations.

The CCM and the periodic model have both similarities and differences. In both the models, the direct lattice translation vectors are transformed. A large unit cell (supercell) is introduced in both the approaches for the perfect host crystal in such a way that the point symmetry of the corresponding Bravais lattice is maintained. Both the approaches converge into equivalent results for the calculations of non-defective solids [59]. Although the CCM calculations correspond to the $\kappa = 0$ approximation, they include not only the Γ -point but also consider other points in the BZ. The reason is that by generating a large cyclic cluster of several PUCs, the BZ is transformed into a reduced Brillouin zone (RBZ). Within this transformation special points of the BZ

become equivalent to the Γ -point of the RBZ. They are therefore included in the CCM calculation [59]. The difference between both approaches is the number of considered integrals is considered in finite region in the CCM in contrast to the periodic models. The advantage of the CCM compared to the supercell model in the description of the ideal solid is that all techniques developed for molecular quantum chemistry, like the improved virtual orbitals (IVO) [60], or configuration interaction (CI), can be applied. In cases where defective crystals are considered, the CCM has the advantage that there are no artificial defect-defect interactions. In periodic calculations such interactions appear and can only be reduced by the enlargement of the supercell at the expense of computer time, but they can not be omitted completely. Furthermore, the CCM allows the calculation of charged systems without the use of an artificial counter charge, since the defect is not repeated periodically.

4 Experimental Background

Nanostructured materials represent a new generation of advanced materials. They exhibit unique and technologically attractive mechanical, electrical, optical or magnetic properties [61, 62] which are different from those of conventional coarse-grained polycrystals. Their outstanding properties are attributed to the size and interface effects [63]. This makes these solids interesting for applications as functional materials with tailored properties.

Ion conducting nanocrystalline oxides, such as, Li_2O with particle sizes in the nm range are characterized by a heterogeneous structure consisting of nanosized crystalline grains [62]. It was observed [64–66] that reducing the grain size of Li_2O from some μm to about 20 nm does not affect the overall conductivity, and hence the Li^+ diffusivity, at all. In contrast, for the composite material $\text{Li}_2\text{O}:\text{B}_2\text{O}_3$, measurements of dc conductivity have shown that the micro- and the nanocrystalline materials behave totally different. For microcrystalline samples, the conductivity decreases monotonically with the B_2O_3 content, while for the nanocrystalline samples, the conductivity shows a maximum at about 50 % of B_2O_3 content, although B_2O_3 is an insulator. In both cases, the conductivity decreases above a certain threshold (Fig. 4.4).

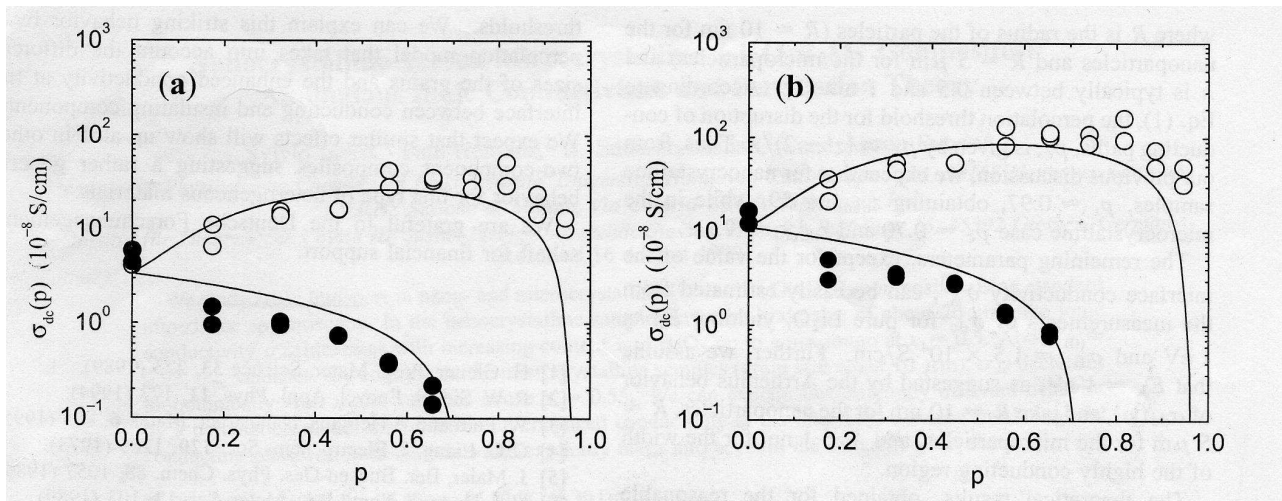


Figure 4.4: Plot of dc conductivities of the micro-(full circles) and nanocrystalline (open circles) $\text{Li}_2\text{O}:\text{B}_2\text{O}_3$ composites as a function of B_2O_3 volume fraction p at two different temperatures, (a) $T = 433$ K and (b) $T = 453$ K [64].

- For the nanocrystalline $(1-p)\text{Li}_2\text{O}:p\text{B}_2\text{O}_3$ composites (average grain size of about

20 nm), the ionic conductivity σ_{dc} increases with increasing content of B_2O_3 upto a maximum at $p \approx 0.7$, above $p \approx 0.96$, σ_{dc} decreases.

- For the microcrystalline $(1-p)Li_2O:pB_2O_3$ composites (average grain size of about $10 \mu m$), σ_{dc} decreases with p and vanishes above $p \approx 0.7$.

This striking behavior is due to the different sizes of the grains and the enhanced conductivity at the interface between conducting and the insulating components (Fig 4.5).

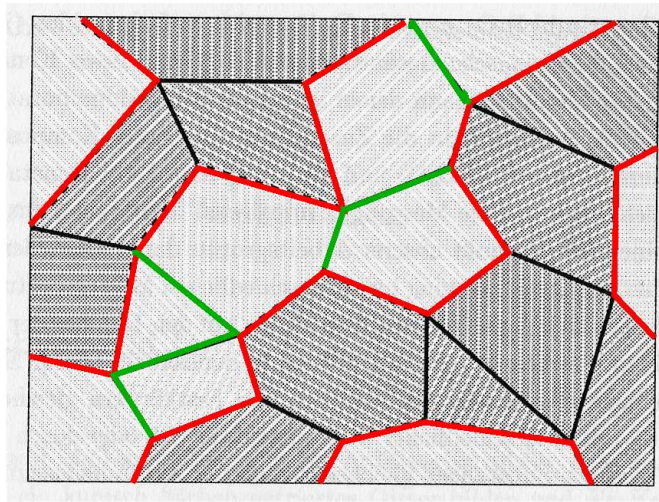


Figure 4.5: Sketch of $Li_2O:B_2O_3$ composite material; light grey areas represent ionic conductor grains (Li_2O) and dark grey areas represent insulator grains (B_2O_3). The network of interfaces consists of interfaces between ionic conductor grains (green lines), interfaces between insulator grains (black lines) and interfaces between ionic conductor and insulator grains (red lines) [66]

For the nanocrystalline samples, the width of the interfaces becomes close to the average grain size. In this case, the highly conducting interface region can act as a bridge between two Li_2O grains not in direct contact to each other, opening up additional paths for Li ions. Whereas, for microcrystalline samples, the interface region between B_2O_3 and Li_2O grains does not play a significant role since its width is negligible compared to the grain sizes, and conducting paths can open up only when two Li_2O grains get in direct contact to each other.

In the present study, quantum chemical model calculations are performed to investigate the mechanism of the observed enhanced conductivity in $Li_2O:B_2O_3$ nanocomposites.

5 Bulk Properties of Li_2O

Li_2O has anti-fluorite structure (space group $\text{Fm}\bar{3}\text{m}$) with lattice constant $a = 4.619$ Å [67] at room temperature. The lattice consists of a primitive cubic array of Li^+ ions, of spacing $a/2$, with the O^{2-} ions occupying alternate cube centers Fig. 5.6. Lithium oxide is of considerable interest because of its potential applications. It is

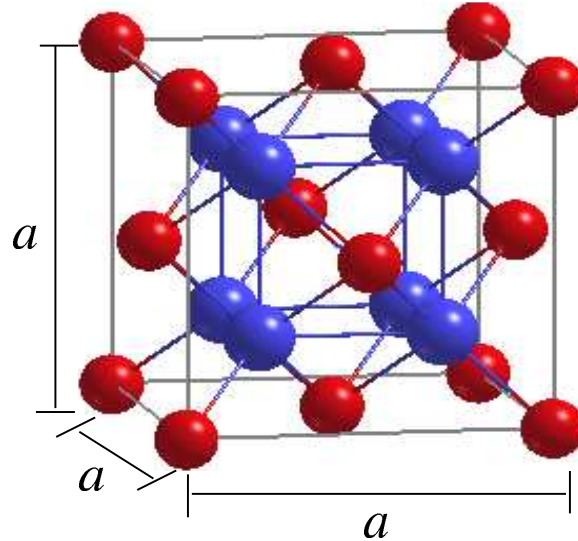


Figure 5.6: Lithium oxide bulk unit cell. Red spheres represent the oxygens and blue spheres represent the lithium atoms

applied in deuterium-tritium fusion reactors as blanket breeding material [68] and in solid state batteries [69]. It is one of the simplest oxides and hence, it serves as a model system for the study of other ionic oxides. Both theoretical and experimental investigations have been performed for Li_2O to understand the energetic properties [70–74], electronic properties [74–83], conduction mechanism [64–66,86], and properties of defects [79,81,83–93].

In this study, bulk properties of Li_2O such as, the lattice constant, the heat of atomization, the electronic properties and the defect properties have been calculated with the methods and models described in previous sections. The lattice parameter a has recently been measured at nine temperature values in the range 293–1603 K, using the technique of inelastic neutron scattering on single crystals and polycrystals [78]. The a versus T curve shows a linear behavior in the 293–1300 K interval. An extrapolation to $T = 0$ K gives $a = 4.573$ Å with a decrease of 0.05 Å with respect to room temperature value of 4.619 Å [67]. The experimental value of the heat of atomization is 1154

kJ/mol [94] and the band gap (E_g) is 7.99 eV [81]. The investigation of defects in Li_2O crystal is necessary to understand its conduction mechanism. The dominant intrinsic defects in Li_2O are point defects [84–86], either as cation vacancies or cation-Frenkel type; i.e., vacancies and interstitials in the Li sublattice. Schottky disorder is also observed, but it is not as predominant as the cation-Frenkel defect [86]. On the other hand, the dominant irradiation defects in Li_2O are known as F centers [82, 87, 88] and F^+ centers [79, 82, 83, 89, 92, 93]. In the present study, only cation vacancy and F center are investigated. The formation energies of these two types of defect are calculated and the relaxation effects are investigated.

Finally, the diffusion of Li^+ in Li_2O is investigated. The mechanism of Li^+ migration in Li_2O is studied by calculating the energy barrier for the movement of Li^+ from a regular site to an adjacent cation vacancy defect position. The calculated energy barrier is compared with the experimental activation energy [65, 66].

5.1 Stoichiometric Li_2O : MSINDO-CCM results

In this section, the calculated results for Li_2O bulk structure, heat of atomization, electronic properties as band gap and electronic density of states (DOS) are presented as calculated by the cyclic cluster model (CCM) with the semiempirical SCF-MO method MSINDO. It was found to be necessary to reoptimize the standard Li parameters [14, 22] for the crystalline Li_2O .

5.1.1 Parameterization

First, the standard parameters [14, 22] were applied for the calculation of Li_2O bulk properties. The calculated values of the lattice parameter a , the binding energy per Li_2O unit E_u and the band gap (E_g) obtained with a $\text{Li}_{64}\text{O}_{32}$ cyclic cluster are compared with experimental values in Table (5.2). Lattice parameter a is overestimated by 0.44 Å compared to the experimental value 4.573 Å [78] obtained at 0 K and is overestimated by 0.39 Å compared to the room temperature value of 4.619 Å [67]. The binding energy per Li_2O unit E_u is compared with the negative value of experimental heat of atomization of Li_2O (−1154 kJ/mol [94]). The calculated E_u value is reasonable, underestimated by only 42 kJ/mol compared to the experiment. Whereas the E_g is overestimated by 3.2 eV compared to the experimental value [81].

Table 5.2: Bulk properties a (Å), E_u (kJ/mol) and E_g (eV) of Li_2O obtained with the standard parameterization of MSINDO

Properties	Calculated	Experiment
a	5.01	4.573 [78] ^a , 4.619 [67] ^b
E_u	-1112	-1154 [94]
E_g	11.3	7.99 [81]

^a extrapolated to $T = 0$ K

^b value obtained at room temperature

In order to obtain better bulk properties of Li_2O , the Li atomic parameters and Li-O bond parameters were reoptimized with a $\text{Li}_{64}\text{O}_{32}$ cyclic cluster for the experimental lattice parameter a , heat of atomization and band gap. The calculated values obtained with new parameterization are compared with the experiment in Table (5.3). The lattice parameter a is 4.69 Å, which is only 0.07 Å larger than the experimental value obtained at room temperature [67] and 0.12 Å larger than that obtained at 0 K [78]. Calculated E_u is overestimated by 24 kJ/mol compared to the experiment [94] and E_g is overestimated by 1 eV compared to the experimental $E_g = 7.99$ eV [81].

Table 5.3: Bulk properties a (Å), E_u (kJ/mol) and E_g (eV) of Li_2O obtained with new parameterization of MSINDO

Properties	Calculated	Experiment
a	4.69	4.573 [78] ^a , 4.619 [67] ^b
E_u	-1178	-1154 [94]
E_g	9.0	7.99 [81]

^a extrapolated to $T = 0$ K

^b value obtained at room temperature

The optimized parameters for Li and O are compared with standard parameters [14,22] in the following table (5.4).

Table 5.4: Comparison of standard and optimized parameters (a.u) for Li atom and Li-O bond

	Standard	Optimized (present work)
Li		
ζ_s	0.7497	0.9072
ζ_p	0.7226	0.9072
ζ_s^U	0.6829	0.6016
ζ_p^U	0.6697	0.6016
τ_{1s}	2.0365	2.2538
I_s	-0.1952	-0.2036
I_p	-0.0586	-0.0136
K_σ	0.1510	-0.0737
$K_{p\sigma}$	0.1510	0.2269
$K_{p\pi}$	0.1150	0.3366
κ_1	0.5930	0.1267
κ_2	1.2702	0.3823
$\kappa_{3,(s,p)}$	1.2450	0.0309
O		
κ_2	0.2485	0.2263

In the next section, the convergence behavior for the optimized bulk properties with increasing size of cyclic cluster is investigated.

5.1.2 Convergence Test

Li_2O bulk is modeled with four clusters of increasing size, $\text{Li}_{32}\text{O}_{16}$, $\text{Li}_{64}\text{O}_{32}$, $\text{Li}_{216}\text{O}_{108}$ and $\text{Li}_{512}\text{O}_{256}$, using the cyclic cluster model (CCM) with Madelung contributions [24, 58]. The results obtained for the lattice parameter a , the binding energy per Li_2O unit E_u , the band gap (E_g) and band width (W) are compared to each other and to experimental results from the literature (Table 5.5). For the calculation of the band gap, the energies of the virtual orbitals are corrected according to a scheme proposed by Huzinaga (improved virtual orbitals, IVO) [60]. The cluster size and shape is quantified by the average relative coordination number k [95, 96]. Here k is defined as the average ratio of all coordination numbers K_i of the N atoms in the cluster and the

ideal coordination number K_{ib} in the bulk

$$k = \frac{1}{N} \sum_{i=1}^N \frac{K_i}{K_{ib}} \quad (5.72)$$

It can be seen that there is a rapid convergence of bulk properties with increasing cluster size. Lattice parameter a is converged with the $\text{Li}_{64}\text{O}_{32}$ cluster. The converged value, 4.68 Å, agrees with the experimental value at room temperature [67]. The

Table 5.5: Dependence of calculated a (Å), E_u (kJ/mol), E_g (eV) and W (eV) on cyclic cluster size

System	k	a	E_u	E_g	W
$\text{Li}_{32}\text{O}_{16}$	0.578	4.60	-1271	9.40	6.9
$\text{Li}_{64}\text{O}_{32}$	0.672	4.69	-1178	9.00	5.5
$\text{Li}_{216}\text{O}_{108}$	0.770	4.68	-1184	9.00	5.5
$\text{Li}_{512}\text{O}_{256}$	0.824	4.68	-1184	9.20	5.6
Exp.		4.573 [78] ^a , 4.619 [67] ^b	-1154 [94]	7.99 [81]	5 [76]

^a extrapolated to $T = 0$ K

^b value obtained at room temperature

deviation is +0.06 Å or 1.3 %. However, if it is compared with the experimental value at $T = 0$ K (4.573 Å) [78], the calculated value 4.68 Å is too large by 0.11 Å. A similar rapid convergence of the bulk properties was observed for the binding energy per Li_2O unit and the band gap. The converged value of E_u is -1184 kJ/mol. Thus E_u is overestimated by only 30 kJ/mol compared to the experimental value, -1154 kJ/mol [94]. The converged value of band gap (E_g) is 9.0-9.2 eV which is about 1 eV higher than the experimental value of 7.99 eV [81]. The slight increase of E_g from cluster $\text{Li}_{216}\text{O}_{108}$ to $\text{Li}_{512}\text{O}_{256}$ (by 0.2 eV) is due to the deficiency of the IVO correction which corresponds to a minimal CI expansion of an excited state including the highest occupied molecular orbital (HOMO) and the corresponding unoccupied orbital. For larger systems, inclusion of more orbitals is necessary to account for more delocalized character of the excitation. The density of states (DOS) curve for the $\text{Li}_{216}\text{O}_{108}$ cluster is given in Fig. 5.7. It is observed that the valence band (VB) is mainly formed by the oxygen $2p$ orbitals with only small contributions from Li, whereas the conduction band (CB) is dominated by Li states. The lowest unoccupied crystal orbital (LUCO)

is delocalized over all Li atoms of the cluster. The position of this virtual orbital is fairly independent of the model used. The converged value of valence band width (W) is 5.5-5.6 eV which is in good agreement with the experimental value of 5 eV [76].

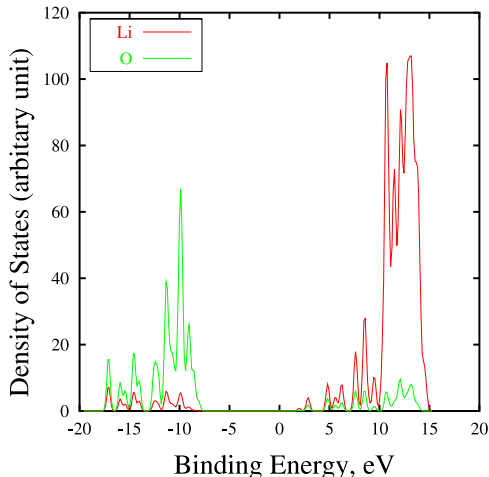


Figure 5.7: Density of states (DOS) for bulk Li_2O as obtained for $\text{Li}_{216}\text{O}_{108}$ cluster (MSINDO)

5.2 Stoichiometric Li_2O : DFT results

In this section the bulk properties of Li_2O as obtained from five different DFT methods namely, PW1PW [37], B3LYP [35, 36], PWGGA, PWGGA-US and PWGGA-PAW, are presented. The first three DFT methods are implemented in the crystalline orbital program CRYSTAL03 [41]. In order to investigate the effect of basis set changes on the structural, energetic and electronic properties, five basis sets of increasing quality are used for Li and O atoms.

For the first set, a 6-1G basis [97] is used for Li. In the second set, a 6-11G [98] basis is used which is an extension of the 6-1G basis where the outer exponent has been optimized in $\text{Li}(\text{OH})\text{H}_2\text{O}$. The third Li basis set is 7-11G* [99]. The 7-11G* basis for Li is further extended to 7-11G(2d) in the present study. The inner $1s$ and $2sp$ shells remained unchanged while the orbital exponents of the $3sp$ and d shells were optimized at PW1PW level for Li_2O (Table 5.6). For O, first a 8-411G basis is used as optimized for Li_2O by Dovesi *et al.* [70]. The second O basis set is 8-411G* [100]. The 8-411G* basis set is further extended to 8-411G(2d) by adding one more d polarization function in this study. Five combinations of these atomic basis sets (BS) have been applied, BS A (Li:6-1G, O: 8-411G), BS B (Li: 6-11G, O: 8-411G*), BS C (Li: 7-11G*, O: 8-411G*),

BS D (Li: 7-11G(2d), O: 8-411G*), and BS E (Li: 7-11G(2d), O: 8-411G(2d)).

Table 5.6: Optimized orbital exponents of the uncontracted Gaussian functions

	Lithium ^a		Oxygen ^b	
Shell	7-11G*	7-11G(2d)	8-411G*	8-411G(2d)
<i>sp</i>	0.922	0.922	0.470	0.470
<i>sp</i>	0.193	0.154	0.200	0.200
<i>d</i>	0.179	0.489	0.570	0.570
<i>d</i>		0.245		0.285

^aInner 7G core taken from Ref. [99]

^bInner 8-4G core taken from Ref. [100]

The DFT methods, denoted as PWGGA-US and PWGGA-PAW, are implemented in the VASP code [46–48]. For PWGGA-US method, sets of plane waves with three different energy cutoffs (E_{cut}), $E_1=396$ eV, $E_2=515$ eV, and $E_3=594$ eV, are used to describe the valence electrons, while the core electrons are represented by ultra soft pseudopotentials (US PP) [51,52]. In the PWGGA-PAW method, sets of plane waves with three different energy cutoffs, $E_1=400$ eV, $E_2=520$ eV, and $E_3=600$ eV, describe the valence electrons, while the core electrons are represented by Projector Augmented Wave (PAW) potentials [53,55]. In both cases, E_1 represents the E_{cut} corresponding to the standard value which is obtained from the VASP guide [101].

Structural, Energetic and Electronic properties

Calculated values of optimized lattice parameter a , binding energy per Li_2O unit E_u and band gap E_g are given in Tables 5.7 and 5.8. The deviation is less than 2.5 % for the lattice parameter with all methods. The two hybrid DFT methods, PW1PW and B3LYP, give close values to each other and to the experimental value 4.573 Å [78]. Among the three pure Perdew-Wang implementations (PWGGA, PWGGA-PAW and PWGGA-US) (Table 5.8), PWGGA-US gives the worst value of a . The deviation is 0.11 Å from the experimental value. This discrepancy can be due to an inaccurate description of the Li core electrons by the US PP. The deficiency is removed by PAW

potential. PWGGA-PAW and PWGGA methods give close values of lattice parameter a to each other and to the experimental value. The calculated lattice parameter is converged with energy cutoff $E_{cut} = \text{E2}$ for the plane wave based methods. For the CRYSTAL calculations, it is found that the choice of the atomic basis set has nearly no effect on the structural properties. a is already converged with the BS B.

Table 5.7: Basis set dependence of calculated a (\AA), E_u (kJ/mol), and E_g (eV) obtained with PW1PW and B3LYP

BS	PW1PW					B3LYP					Exp.
	A	B	C	D	E	A	B	C	D	E	
a	4.56	4.57	4.59	4.58	4.58	4.58	4.59	4.59	4.59	4.59	4.573 [78], 4.619 [67]
E_u	-1107	-1116	-1130	-1134	-1134	-1106	-1110	-1122	-1123	-1123	- 1154 [94]
E_g	10.19	8.37	8.66	7.95	7.96	10.23	8.49	8.82	8.11	8.12	7.99 [81]

Table 5.8: Optimized a (\AA), E_u (kJ/mol), and E_g (eV) calculated with three different Perdew-Wang implementations

BS/ E_{cut}	PWGGA ^a					PWGGA-US ^b			PWGGA-PAW ^b			Exp.
	A	B	C	D	E	E1	E2	E3	E1	E2	E3	
a	4.59	4.61	4.63	4.63	4.62	4.45	4.46	4.46	4.58	4.64	4.63	4.573 [78], 4.619 [67]
E_u	-1131	-1143	-1160	-1164	-1164	-1192	-1189	-1189	-1169	-1176	-1165	- 1154 [94]
E_g	8.00	6.24	6.53	5.82	5.83	5.00	5.18	5.18	5.02	5.00	5.00	7.99 [81]

^a Obtained with CRYSTAL03

^b Obtained with VASP

The binding energy per Li_2O unit (E_u) was calculated for the optimized value of lattice parameter a . For the calculation of the atomic reference energies with CRYSTAL03, the basis sets of the free atoms were optimized by augmenting the basis sets of the periodic calculations by diffuse sp and d shells until convergence was achieved for the total energy. For both the PWGGA-US and PWGGA-PAW implementations in VASP, atomic reference energies were calculated with US PP and PAW potential by using pseudo lattice constants of 13 \AA for Li atom and 8 \AA for O atom. The VOSKOWN keyword [102] was used for a better convergence of the ground state energy of atoms as it is important particularly for open-shell GGA based calculation [101]. All the methods give binding energies within ± 35 kJ/mol (Tables 5.7 and 5.8) of the negative experimental heat of atomization, -1154 kJ/mol [94]. The two hybrid methods, B3LYP

and PW1PW, (Table 5.7) underestimate E_u by 31 kJ/mol and 20 kJ/mol calculated with the BS D. The basis set convergence for E_u is slower than for structural properties. With the three LCAO based DFT implementations, E_u is converged with BS D. In the case of PWGGA-US, E_u is converged with $E_{cut} = E2$ as for the lattice parameter a . Whereas, PWGGA-PAW shows different behavior of E_u convergence with E_{cut} (Table 5.8). The reason can be attributed to the difference between the USPP and PAW potential.

In a recent experimental investigation [81], the value of the band gap (E_g) was obtained as 7.99 eV. This value is much higher than the results of photoemission and loss electron energy spectroscopy (LEES) 7-7.5 eV [76], the absorption spectroscopy at low temperature 7.02 eV [82], and optical absorption spectroscopy, 6.6 eV [80]. Several theoretical studies on the electronic properties of Li_2O have already appeared in the literature. Band gaps and bandwidths are generally overestimated by the *ab initio* Hartree-Fock method [74,75] and underestimated by the DFT local density approximation (LDA) [75,77]. DFT methods based on the generalized gradient approximation (GGA) give closer agreement [75] with the experiment, and a hybrid DFT method incorporating exact HF exchange [75] further improves electronic properties.

The calculated values of band gap (E_g) are given in Tables 5.7 and 5.8. The best agreement for the experimental value of E_g is obtained with the PW1PW method using BS D (Table 5.7). The calculated value of E_g is 7.95 eV which is very close to the experimental value of 7.99 eV [81]. The second best agreement is obtained with the B3LYP method, 8.11 eV (BS D). The three pure Perdew-Wang implementations, LCAO based PWGGA and plane wave based PWGGA-US and PWGGA-PAW, underestimate the band gap (Table 5.8). For PWGGA-US and PWGGA-PAW, the E_g values are very close, 5.18 eV and 5.00 eV, respectively. This is considerably smaller than the 5.82 eV obtained with CRYSTAL PWGGA using BS D. The difference in E_g is not due to the LCAO basis set incompleteness as it has already converged with BS D. For PWGGA-US and PWGGA-PAW methods, E_g is converged with energy cutoff E2. The atomic basis set has a pronounced effect on the electronic structure. The PW1PW E_g value is 10.19 eV with BS A, which is 1.82 eV, 1.55 eV, 2.24 eV, and 2.23 eV larger than that with BS B, C, D, and E, respectively. The difference is mainly due to the inclusion of diffuse and polarization functions in the Li basis set. These orbitals are dominating at

the lower part of the conduction band (CB). The basis set effect is almost independent from the method, as can be seen (Tables 5.7 and 5.8) by the difference obtained with BS A, B, C, D, and E for B3LYP and PWGGA methods. In all cases, E_g is converged with BS D.

The total (TDOS) and projected density of states (PDOS) were calculated using the Fourier-Legendre technique [104] with a *Monkhorst net* [105] using shrinking factors $s=8$. The calculated TDOS of Li_2O is compared with X-ray photoelectron spectrum [76] as shown in Fig. 5.8. The overview of the calculated DOS by PW1PW method with BS D is shown. This method is chosen since it gives the best agreement with experiment for E_g . The experimental XPS spectrum was shifted to the calculated Fermi level which corresponds to the VB top in the present case. A good agreement with experiment was obtained for the band widths and the main peak positions within the VB. The calculated valence band width is about 5 eV which is in good agreement with the experimental value [76]. The Li PDOS (Fig. 5.8) shows that Li atoms are involved in all bands. The CBs are created mainly by Li states.

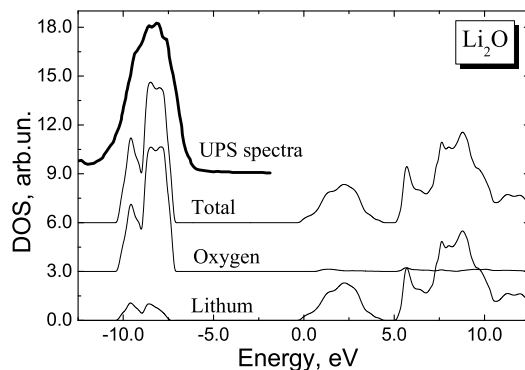


Figure 5.8: Density of states of Li_2O obtained with the PW1PW method using basis set D. For comparison the X-ray photoelectron spectrum [76] is also shown. The experimental XP spectrum was shifted to the top of the valence band.

The bonding picture of crystalline Li_2O is illustrated by the electron charge density distribution along the Li-O bond. Here, the PW1PW method is taken as an example. All the other methods give qualitatively similar behavior. The charge density distribution map is shown in Fig. 5.9. The contour lines range from 0.0 to $0.3 \text{ e}/\text{\AA}^3$ with steps of $0.02 \text{ e}/\text{\AA}^3$. It can be seen that the charge distribution around both Li and O

atoms is almost spherical.

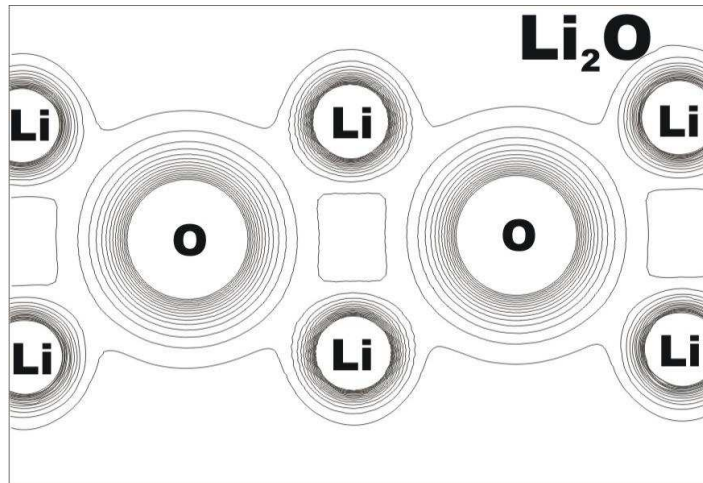


Figure 5.9: Electronic charge density distribution for Li_2O .

The charge density magnitude between these two atoms is small which indicates that the interaction is mainly ionic.

Thus the hybrid PW1PW method gives the best reproduction of bulk properties for Li_2O . The other hybrid method B3LYP gives a similar trend. The three Perdew-Wang implementations (PWGGA, PWGGA-PAW and PWGGA-US) show dissimilarity. PWGGA-US gives smaller lattice parameter and larger E_u compared to other two methods. Both the PWGGA-PAW and PWGGA-US give smaller value of E_g than CRYSTAL-PWGGA, but all three methods underestimate the band gap. Extension of localized basis set has a relatively small effect on structural and energetic properties, but a pronounced effect on electronic properties. The structural and energetic properties are converged with BS B and BS C, respectively, and electronic properties are converged with BS D. For the plane wave based DFT methods, all the properties are converged with an energy cutoff E2. The reparameterized version of MSINDO gives comparable results to the DFT methods, lattice parameter a and E_u are reasonable, E_g is overestimated by 1 eV compared to the experiment.

In the next section, the defect properties of Li_2O are presented.

5.3 Defect properties of Li_2O

In this section, the defect properties of Li_2O are discussed. Only two types of defect are considered here, the cation vacancy defect and the F center. Based on the optimized

structural parameters for the perfect crystals, supercells were constructed for defect calculations. Three different cyclic clusters, $\text{Li}_{64}\text{O}_{32}$, $\text{Li}_{216}\text{O}_{108}$ and $\text{Li}_{512}\text{O}_{108}$ are used for the simulation of defects with the MSINDO-CCM. DFT calculations are performed using the supercell model (SCM). A $\text{Li}_{64}\text{O}_{32}$ supercell is used for the simulation of defects. Among the five DFT methods discussed in the previous section, only four methods are considered here. These are PW1PW and B3LYP methods using the CRYSTAL03, and PWGGA-US and PWGGA-PAW methods using the VASP code. The LCAO based PWGGA method showed SCF convergence problems for the defective system, therefore this method is not considered here.

In the CCM, the cyclic clusters for the defective systems are embedded in the Madelung field of the perfect Li_2O crystal. The charges for this embedding are the Löwdin charges calculated from the simulation of the corresponding perfect cyclic cluster. In the SCM approach, the defective systems are considered as a new crystal with an artificially introduced point defect periodicity. The calculation is done in the same way as for a perfect crystal using the \mathbf{k} sampling of the BZ.

5.3.1 Cation vacancy

Li_2O is a fast ion conductor [65]. It is applied in solid-state batteries [69]. An experimental investigation [86] shows that the mobile species is the Li^+ ion and the most likely mechanism for its migration is via cation vacancies. Although there have been several experimental [65,86] and theoretical [84–86] studies of ionic transport in Li_2O , the defect formation energy of cation vacancy and relaxation effect for defective systems are still not known. In the present section, the formation energy of a cation vacancy in Li_2O , the effect of relaxation for this type of defect and the influence of defect on the electronic properties are studied.

In Table 5.9, calculated cation vacancy formation energy, $E_{de}(V)$ and relaxation energy, E_R using MSINDO-CCM are presented. The vacancy is created by removing one Li from the cluster keeping the system neutral. This leads to multiplicity 2 per cell. The calculations were performed by UHF method.

The formation energy of cation vacancy $E_{de}(V)$ is calculated as:

$$E_{de}(V) = E(\text{Li}_{2n-1}\text{O}_n) + E(\text{Li}) - E(\text{Li}_{2n}\text{O}_n) \quad (5.73)$$

Here $E(\text{Li}_{2n-1}\text{O}_n)$ and $E(\text{Li}_{2n}\text{O}_n)$ denote the total energy of the cyclic cluster or the supercell with and without vacancy, respectively, and $E(\text{Li})$ is the energy of free Li atom. The relaxation energy, E_R is calculated by subtracting the energy of relaxed system from that of the unrelaxed system. First, the relaxation is performed for the four nearest O atoms close to the Li vacancy. This relaxed area is indicated as 1-NN. Then the relaxed area is increased systematically up to the twelfth nearest-neighbors for the $\text{Li}_{512}\text{O}_{256}$ cyclic cluster until convergence is achieved. In the CCM approach, the relaxation area is chosen in such a way that the defect is in the center. For the smallest cluster, $\text{Li}_{64}\text{O}_{32}$, relaxation is possible only up to the third-nearest neighbors. Whereas, relaxation area can be increased up to the seventh-nearest neighbors for $\text{Li}_{216}\text{O}_{108}$. It can be seen from Table 5.9 that the defect formation energy is already converged within 1 kJ/mol for the system with relaxation of the tenth-nearest neighbors.

Table 5.9: Formation energy (kJ/mol) of cation vacancy, $E_{de}(V)$ and relaxation energy, E_R of $\text{Li}_{64}\text{O}_{32}$, $\text{Li}_{216}\text{O}_{108}$ and $\text{Li}_{512}\text{O}_{108}$ with MSINDO-CCM.

Neighbor Relaxation	$\text{Li}_{64}\text{O}_{32}$		$\text{Li}_{216}\text{O}_{108}$		$\text{Li}_{512}\text{O}_{256}$	
	$E_{de}(V)$	E_R	$E_{de}(V)$	E_R	$E_{de}(V)$	E_R
unrelaxed	767	0	776	0	778	0
1-NN	731	36	749	27	743	35
2-NN	639	128	657	119	631	147
3-NN	569	198	587	189	577	200
4-NN			581	195	570	208
5-NN			567	209	555	223
6-NN			550	226	536	242
7-NN			546	230	533	245
8-NN					520	258
9-NN					517	261
10-NN					515	263
11-NN					515	263
12-NN					514	264

Thus the defect formation energy of a cation vacancy in Li_2O according to the MSINDO-CCM is 514 kJ/mol. To the best of my knowledge, there is no experimental or theoretical value of cation vacancy defect formation energy of Li_2O . This value is, therefore, compared with the DFT results in this study. In Fig. 5.10 the convergence behavior

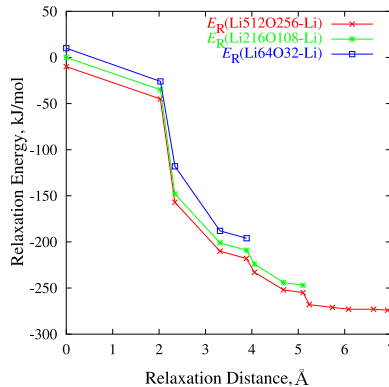


Figure 5.10: Convergence of relaxation energy, E_R (kJ/mol) for the Li defect with increasing relaxation distance (\AA) (MSINDO-CCM)

of E_R with increasing relaxation distances is shown.

In Table 5.10, calculated cation vacancy formation energies, $E_{de}(V)$ as obtained from the DFT methods are presented. $E_{de}(V)$ is calculated with Eq. (5.73) for unrelaxed and fully relaxed systems. The converged values of $E_{de}(V)$ with PW1PW and B3LYP are 576 kJ/mol and 566 kJ/mol, respectively.

Table 5.10: Formation energy of cation vacancy, $E_{de}(V)$ (kJ/mol) in Li_2O for unrelaxed and relaxed structure using the DFT methods ($\text{Li}_{64}\text{O}_{32}$ Supercell)

Method	PW1PW		B3LYP		PWGGA-US			PWGGA-PAW		
	A	B	A	B	E1	E2	E3	E1	E2	E3
unrelaxed	682	642	671	629	661	579	579	593	558	555
relaxed	577	576	567	566	583	500	500	517	480	477

The relaxation energy, E_R is ≈ 65 kJ/mol in both cases. Since the PW1PW method gives the best agreement for the bulk properties of Li_2O , it is considered as reference. For the two plane wave based DFT methods, PWGGA-US and PWGGA-PAW, $E_{de}(V)$ is converged with energy cutoff E2. Compared to the results of the PW1PW method, the PWGGA-US and PWGGA-PAW methods give smaller values of $E_{de}(V)$ by 76 kJ/mol and 96 kJ/mol, respectively. The difference can be due to the different functionals, or to the effect of two different types of basis sets. Further test calculations applying larger basis set than BS B for PW1PW and B3LYP methods showed SCF convergence problems. So it can not be confirmed whether this discrepancy arises from the incompleteness of BS B. Although there is a little difference in $E_{de}(V)$ ob-

tained with PWGGA-US and PWGGA-PAW approaches, the E_R is nearly same (≈ 80 kJ/mol). The MSINDO-CCM $E_{de}(V)$ value is smaller than the PW1PW result by 61 kJ/mol. The structural relaxation effects are investigated by measuring the changes of distances of the relaxed atoms with respect to the defect position. MSINDO-CCM and PW1PW results for the relaxation effects are shown in Tables 5.11 and 5.12, respectively. Only PW1PW results are presented here, since all other DFT methods give the same trend. Four O atoms in the first coordination shell (1-NN) give an outward relaxation from the vacancy, namely by 3.4 % with the MSINDO-CCM and by 6.6 % with the PW1PW method. This is reasonable, since the electrostatic attraction by the Li^+ cation is missing. The removal of one neutral Li atom creates a hole in the valence band. One of the surrounding four O atoms (formally O^{2-}) in 1-NN becomes O^- and spin density is localized on this O atom. Six Li atoms in the second coordination shell (2-NN) show a strong inward relaxation of -18.8 % with the MSINDO-CCM and -10.0 % with the PW1PW approach. Due to the reduced electrostatic repulsion, the 2-NN Li atoms tend to move towards the vacancy.

Table 5.11: Distances of neighboring atoms (r) Å from the Li vacancy and changes of the distances $\Delta r(\%)$ for the unrelaxed and relaxed atoms in $\text{Li}_{512}\text{O}_{256}$ (MSINDO-CCM)

Atom	r	Unrelaxed	Relaxed	$\Delta r(\%)$
O(4)	r_1	2.03	2.10	+3.4 %
Li(6)	r_2	2.34	1.90	-18.8%
Li(12)	r_3	3.31	3.39	+2.4 %
O(12)	r_4	3.88	3.87	-0.3 %
Li(8)	r_5	4.06	4.09	+0.7 %
Li(6)	r_6	4.68	4.72	+0.9 %
O(12)	r_7	5.10	5.11	+0.2 %
Li(24)	r_8	5.24	5.25	+0.2 %
Li(24)	r_9	5.74	5.75	+0.2 %
O(16)	r_{10}	6.08	6.09	+0.2 %
Li(12)	r_{11}	6.62	6.63	+0.2 %
O(24)	r_{12}	6.93	6.93	+0.0 %

The 12 Li atoms in the third coordination shell (3-NN) show an outward relaxation, whereas 12 4-NN O atoms move toward the vacancy by about -0.3 %. The Li atoms

Table 5.12: Distances of neighboring atoms (r) Å from the Li vacancy and changes of the distances $\Delta r(\%)$ for the unrelaxed and relaxed atoms in $\text{Li}_{64}\text{O}_{32}$ with PW1PW method (BS B)

Atom	r	Unrelaxed	Relaxed	$\Delta r(\%)$
O(4)	r_1	1.98	2.11	+6.6 %
Li(6)	r_2	2.29	2.06	-10.0 %
Li(12)	r_3	3.23	3.26	+0.9 %
O(12)	r_4	3.79	3.78	-0.3 %
Li(8)	r_5	3.98	4.00	+0.5 %
Li(6)	r_6	4.57	4.61	+0.9 %

in the fifth and sixth nearest neighbors show an outward relaxation in both MSINDO-CCM and PW1PW approaches. For the investigation of further relaxation by PW1PW method, one has to consider a supercell larger than $\text{Li}_{64}\text{O}_{32}$ which was not possible due to limited computer resources. With the MSINDO-CCM, it is possible to investigate the relaxation effect for more neighbors using a very large supercell $\text{Li}_{512}\text{O}_{256}$. From Table 5.11, it can be seen that 7-NN O atoms, 8-NN Li atoms, 9-NN Li atoms, 10-NN O atoms and 11-NN Li atoms have very slight outward relaxation, whereas the positions of 12-NN O atoms are unchanged. Thus the results of MSINDO and PW1PW are in qualitative agreement. Relaxation is mainly restricted to the nearest and the second-nearest neighbor atoms.

The study of electronic properties is performed by calculating the density of states (DOS) of the defective supercells. The DOS for a defective $\text{Li}_{216}\text{O}_{108}$ cyclic cluster obtained with MSINDO is shown in Fig. 5.11. All the other methods show qualitatively the same behavior. It can be seen that Li^+ ion vacancy introduces an extra unoccupied level roughly 3.4 eV below the bottom of the conduction band, which is marked by an arrow. In the case of PW1PW method, the unoccupied defect level is situated at 2.1 eV below the bottom of the conduction band. There is no experimental or theoretical value for the position of the unoccupied cation defect level in Li_2O . Since the PW1PW gives the best description of electronic properties of Li_2O among all methods, this is taken as reference. Thus MSINDO-CCM gives higher value (by 1.3 eV) compared to the PW1PW. The B3LYP gives close value (2.0 eV) to the PW1PW. Both the values

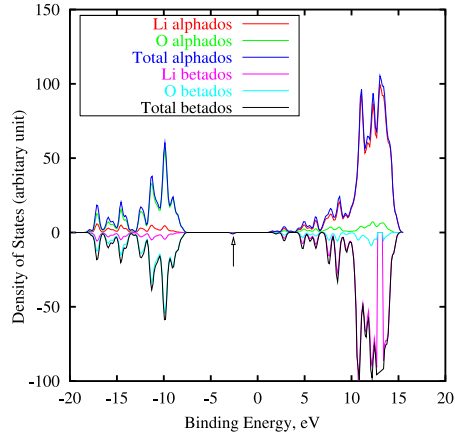


Figure 5.11: Density of states (DOS) for Li vacancy in $\text{Li}_{216}\text{O}_{108}$ (MSINDO-CCM)

are obtained with BS B. PWGGA-US and PWGGA-PAW methods give very small value, 1.3 eV and 1.0 eV, respectively.

5.3.2 F center

Li_2O is proposed as a blanket material in deuterium-tritium fusion reactors [68]. Studies are needed to understand its behavior under irradiation. One of the predominant irradiation defects is known as F center, an oxygen vacancy trapping two electrons. Very few theoretical and experimental investigations [82, 87, 88] have been performed to understand the F center defect in Li_2O . Tanigawa *et al.* [88] performed supercell calculation at the HF level using the CRYSTAL95 code and at the GGA level using the plane wave based CASTEP code. The effect of relaxation on F centers in Li_2O was investigated only for 8 1-NN Li atoms and 12 2-NN O atoms and relaxations were too small to estimate the accuracy. The optical transition energy of F centers was calculated as 4.82 eV [87] with the embedded-molecular-cluster model using semiempirical INDO-type calculation scheme. In a photoluminescence study of Li_2O under excitation with UV light in the fundamental absorption region at low temperature [82], the optical transition energy of F centers was approximated as 3.70 eV. No experimental or theoretical investigations were found in the literature that predict the defect formation energy of F center, $E_{de}(F)$. In the present study, a systematic investigation is performed for the calculation of F center formation energy, $E_{de}(F)$, the effect of relaxation on F center and the optical transition energy of F center with MSINDO-CCM and DFT supercell calculations (PW1PW, B3LYP, PWGGA-US and PWGGA-PAW). To create the F center, one neutral oxygen atom was removed from the supercell. The

defect formation energy of F center, $E_{de}(F)$ is calculated as:

$$E_{de}(F) = E(\text{Li}_{2n}\text{O}_{n-1}) + E(\text{O}) - E(\text{Li}_{2n}\text{O}_n) \quad (5.74)$$

Here $E(\text{Li}_{2n}\text{O}_{n-1})$ and $E(\text{Li}_{2n}\text{O}_n)$ denote the total energy of the cyclic cluster or the supercell with and without defect, respectively, and $E(\text{O})$ is the energy of the free O atom in its ground state. In Table 5.13, calculated F center formation energies, $E_{de}(F)$ and relaxation energies, E_R from MSINDO-CCM calculation are presented. It was found that $E_{de}(F)$ is 1467 kJ/mol for the triplet state of the defective cluster which is 248 kJ/mol larger than that of closed-shell singlet state. The triplet state was treated by the UHF method. The convergence for the defect formation energy and relaxation energy is much faster for the F center compared to the cation vacancy in Li_2O . The converged value of $E_{de}(F)$ is 1219 kJ/mol.

Table 5.13: Defect formation energy of F center, $E_{de}(F)$ and relaxation energy, E_R , kJ/mol of $\text{Li}_{64}\text{O}_{32}$ and $\text{Li}_{216}\text{O}_{108}$ cyclic clusters (MSINDO results)

Neighbor Relaxation	$\text{Li}_{64}\text{O}_{32}$		$\text{Li}_{216}\text{O}_{108}$	
	$E_{de}(F)$	E_R	$E_{de}(F)$	E_R
unrelaxed	1246	0	1231	0
1-NN	1239	7	1224	7
2-NN	1239	7	1224	7
3-NN	1237	9	1221	10
4-NN			1220	11
5-NN			1220	11
6-NN			1220	11
7-NN			1219	12
8-NN			1219	12
9-NN			1219	12
^a 9-NN			1467	185

^a open shell triplet (UHF) calculation

In Fig. 5.12 the convergence behavior of E_R against the relaxation distance is shown. It can be seen that the convergence is achieved within 1 kJ/mol with the relaxation of the seventh-nearest neighbors. Since the convergence is achieved with $\text{Li}_{216}\text{O}_{108}$, it is not necessary to consider the $\text{Li}_{512}\text{O}_{256}$ cyclic cluster here.

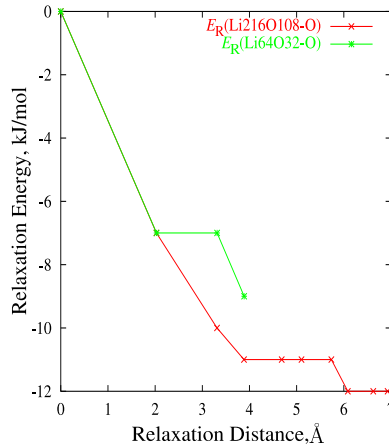


Figure 5.12: Convergence of relaxation energy, E_R (kJ/mol) for F centers with increasing relaxation distance (\AA) (MSINDO-CCM)

In Table 5.14, calculated defect formation energies of F center, $E_{de}(F)$ obtained with DFT methods are presented. The defect formation energy, $E_{de}(F)$ is calculated using Eq. (5.74) for unrelaxed and fully relaxed systems. For the calculations with PW1PW and B3LYP using the CRYSTAL03 program, the basis functions of the oxygen ion were left at the defect position. Calculations were performed for the closed shell singlet state. An open shell triplet state calculation was also performed with PW1PW method using BS B. It was found that $E_{de}(F)$ value for the triplet state is 539 kJ/mol larger than that for the closed shell singlet state. As for the cation vacancy, the PW1PW method is taken as a reference. The converged value of $E_{de}(F)$ with PW1PW using BS C is 848 kJ/mol. The B3LYP method gives a higher value of $E_{de}(F)$, 890 kJ/mol.

Table 5.14: Defect formation energy of F center, $E_{de}(F)$ (kJ/mol) in Li_2O for unrelaxed and relaxed structures at DFT level

Method BS/ E_{cut}	PW1PW				B3LYP			PWGGA-US			PWGGA-PAW		
	A	B	B ^a	C	A	B	C	E1	E2	E3	E1	E2	E3
unrelaxed	1003	878	1420	853	1010	893	894	1089	990	990	1016	975	966
relaxed	1001	873	1412	848	1009	888	890	1051	952	953	1001	957	948

^a open shell triplet calculation

In both methods, the relaxation energy is very small (≈ 5 kJ/mol). For the two plane wave based DFT methods, PWGGA-US and PWGGA-PAW, the converged value of

$E_{de}(F)$ is 950 kJ/mol. Compared to the PW1PW method, this value is overestimated by 100 kJ/mol. The relaxation energies, E_R obtained with PWGGA-US and PWGGA-PAW methods are 37 kJ/mol and 18 kJ/mol, respectively, which are larger than that obtained with PW1PW. The difference can be due to the use of different functionals. Further test calculations applying larger basis set than BS C for the PW1PW method or B3LYP method showed SCF convergence problems. The MSINDO-CCM $E_{de}(F)$ value is 371 kJ/mol larger than the PW1PW result.

The relaxation effects for the F centers are investigated by measuring the changes of distances of the relaxed atoms. MSINDO-CCM and PW1PW results for the relaxation effects are shown in Tables 5.15 and 5.16, respectively. In the case of MSINDO-CCM, results are presented for the $\text{Li}_{216}\text{O}_{108}$ cyclic cluster. Among the DFT methods, only PW1PW results are presented here. All other DFT methods give qualitatively same trend. The F center is surrounded by 8 Li atoms in the first coordination shell (1-NN). Li atoms in 1-NN show an outward relaxation from the vacancy, namely by 2 % with the MSINDO-CCM method and by 1.5 % with PW1PW method. This is reasonable, since the 1-NN Li atoms are positively charged and should, therefore, repel each other as the central oxygen ion is removed. But the effect is much smaller than for the oxygens surrounding the Li defect.

Table 5.15: Distances of neighboring atoms (r) (\AA) from the F center and changes of the distances Δr (%) for the unrelaxed and relaxed atoms in $\text{Li}_{216}\text{O}_{108}$ (MSINDO-CCM)

Atom	r	Unrelaxed	Relaxed	$\Delta r(\%)$
Li(8)	r_1	2.03	2.07	2.0 %
O(12)	r_2	3.31	3.32	0.3 %
Li(24)	r_3	3.88	3.89	0.3 %
O(6)	r_4	4.68	4.69	0.2 %
Li(24)	r_5	5.10	5.11	0.2 %
O(24)	r_6	5.74	5.74	0.0 %
Li(32)	r_7	6.08	6.09	0.2 %
O(12)	r_8	6.62	6.62	0.0 %
Li(48)	r_9	6.93	6.93	0.0 %

The 12 2-NN O atoms show an outward relaxation of 0.3 % with MSINDO-CCM and

Table 5.16: Distances of neighboring atoms (r) (\AA) from the F center and changes of the distances Δr (%) for the unrelaxed and relaxed atoms in $\text{Li}_{64}\text{O}_{32}$ obtained at the PW1PW level with BS B

Atom	r	Unrelaxed	Relaxed	Δr (%)
Li(8)	r_1	1.98	2.01	1.5 %
O(12)	r_2	3.23	3.24	0.1 %
Li(24)	r_3	3.79	3.79	0.0 %
O(6)	r_4	4.57	4.57	0.0 %
Li(24)	r_5	4.98	4.98	0.0 %
O(24)	r_6	5.60	5.60	0.0 %

of 0.1 % with the PW1PW approach, indicating that the positions of the oxygen atoms are almost unchanged. These agree well with the outward relaxation of 1-NN Li atoms and 2-NN O atoms for the F centers in Li_2O obtained by Tanigawa *et al.* [88]. But in that study the displacements were very small, namely by 0.05 % for 1-NN Li atoms and 0.01 % for 2-NN O atoms.

Further relaxation at the PW1PW level (Table 5.16) shows that 24 3-NN Li atoms, 6 4-NN O atoms, 24 5-NN Li atoms and 24 6-NN O atoms are unchanged. Similar behavior is obtained with the MSINDO-CCM approach (Table 5.15).

The experimental value of optical transition energy for oxygen deficient Li_2O is 3.7 eV [82], indicating a location of a doubly occupied defect level about 4.3 eV above the valence-band-maximum (VBM). In the present study, the absorption band is measured by calculating the density of states (DOS) of the defective supercells. The DOS curve for a defective $\text{Li}_{216}\text{O}_{108}$ supercell using MSINDO-CCM approach is shown in Fig. 5.13.

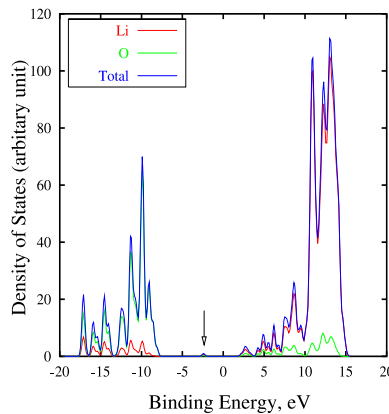


Figure 5.13: Density of states (DOS) for F center in $\text{Li}_{216}\text{O}_{108}$ by MSINDO

Other methods show similar behavior. The calculated value of the absorption band using the MSINDO-CCM approach is 4.0 eV, which is in very good agreement with the experimental value of 3.7 eV. The doubly occupied defect level is marked with an arrow in Fig. 5.13. The optical absorption band is 4.0 eV at PW1PW level and 3.8 eV at B3LYP level. Thus MSINDO reproduces the value of experimental optical absorption band as it is obtained with the high level DFT hybrid methods PW1PW and B3LYP. Two pure PWGGA approaches are giving too small values of the optical absorption energy, namely 2.7 eV with both implementations.

Lithium oxide exhibits high ionic conductivity. This behavior is characterized by the rapid diffusion of a significant fraction of Li ions, within an essentially rigid framework formed by oxygen ions [64–66,84–86]. The diffusion of Li ions occurs through the cation vacancies [66,84–86].

In the following section, the diffusion of Li ions in lithium oxide is discussed.

5.4 Diffusion of Li^+ ion in Li_2O

Diffusion and ionic conduction in Li_2O are matters of great interest in recent years due to the superionic behavior of this material. Lithium oxide has a number of technological applications ranging from miniature, lightweight high-power-density lithium-ion batteries for heart pacemakers, mobile phones and laptop computers to high-capacity energy storage devices for next-generation electric vehicles [106]. The common feature of superionic materials is that these materials show markedly improved diffusivity and in turn fast ionic conductivity in disordered state as compared to their coarse-grained or single-crystalline modifications [66]. In a combined experimental and theoretical study of the defects in Li_2O , Chadwick *et al.* [86] showed that Li^+ ions migrates via cation vacancies. This study was performed in a combination of *ac* conductivity measurements and non-linear least-squares computer simulation, where the diffusion of Li^+ ions was investigated by measuring the activation energy. The experimental value of activation energy (E_A) is 0.49 eV as compared to their calculated value of 0.21 eV. In DFT-LDA studies [84,85], it was also observed that Li^+ ions are diffusing in Li_2O through the cation vacancies, where an E_A of 0.34 eV was calculated.

Recently, Heitjans *et al.* [66] presented two different types of experimental approaches for the study of diffusion and ionic conduction in nanocrystalline ceramics. The first

one is macroscopic method, such as tracer diffusion method, and the second method is known as microscopic method such as, NMR relaxation. E_A for Li ion diffusion in Li_2O derived from the NMR relaxation method is 0.31 eV whereas that obtained with the tracer diffusion method is 0.95 eV. The NMR relaxation method gives smaller E_A value compared to the tracer diffusion method because it gives access to microscopic diffusion parameters like hopping rates of atoms or ions, i.e. short-range motion of the ion and barrier heights for a jump process, whereas, the tracer diffusion method probes the long-range transport [66].

In the present study, diffusion of Li ions in Li_2O is investigated. For the MSINDO-CCM approach, $\text{Li}_{64}\text{O}_{32}$ and $\text{Li}_{216}\text{O}_{108}$ supercells are used whereas for the DFT methods (PW1PW, B3LYP, PWGGA-US, and PWGGA-PAW), only the $\text{Li}_{64}\text{O}_{32}$ supercell is used. First the migration of Li^+ ion is investigated with non-relaxed defective supercells by calculating the activation energy, E_A . The effect of relaxation on E_A is investigated by relaxing the nearest neighboring atoms and then all atoms surrounding the defect and the migrating Li^+ ion. PW1PW and B3LYP calculations were performed using BS A whereas PWGGA-US and PWGGA-PAW calculations were performed using energy cutoff E1. Basis sets larger than BS A and energy cutoffs larger than E1 are not considered, because of high expense of CPU time.

Unrelaxed system

The calculated results of activation energy E_A for the Li^+ ion migration in unrelaxed systems are compared with the experimental value in Table 5.17. The investigation is performed for a single Li^+ ion hop through the cation vacancy. This process is comparable to that studied with NMR relaxation by Heitjans *et al.* [66]. The activation energy is calculated as the difference of energies for the system in which the migrating ion is mid-way between the neighboring regular sites and the system in which the vacancy is on a regular site. The experimental hopping distance for the migration of Li^+ ion from its original tetrahedral site to the vacancy is equal to the nearest Li-Li distance in Li_2O , namely, 2.29 Å. The calculated hopping distance differs for different methods due to the different lattice constants. The hopping distances are 2.28 Å, 2.29 Å, 2.23 Å, 2.29 Å and 2.34 Å, for PW1PW, B3LYP, PWGGA-US, PWGGA-PAW, and MSINDO-CCM, respectively. In Fig. 5.14, the relative energy as function of the Li

Table 5.17: Comparison of calculated activation energy, E_A (eV) for unrelaxed systems with experimental value

Method	Supercell	E_A
PW1PW	$\text{Li}_{64}\text{O}_{32}$	0.45
B3LYP	$\text{Li}_{64}\text{O}_{32}$	0.63
PWGGA-US	$\text{Li}_{64}\text{O}_{32}$	0.47
PWGGA-PAW	$\text{Li}_{64}\text{O}_{32}$	0.49
MSINDO-CCM	$\text{Li}_{64}\text{O}_{32}$	0.17
MSINDO-CCM	$\text{Li}_{216}\text{O}_{108}$	0.21
Exp.		0.31 [66]

hopping distance is shown. The migration path of the Li^+ ion is divided into ten small steps. It can be seen that the Li^+ ion has to pass a barrier in the mid-way between its original position and vacancy position. It can be seen from Table 5.17 that the E_A value differs from method to method. MSINDO-CCM approach is underestimating the experimental E_A value whereas the DFT methods are giving too large values.

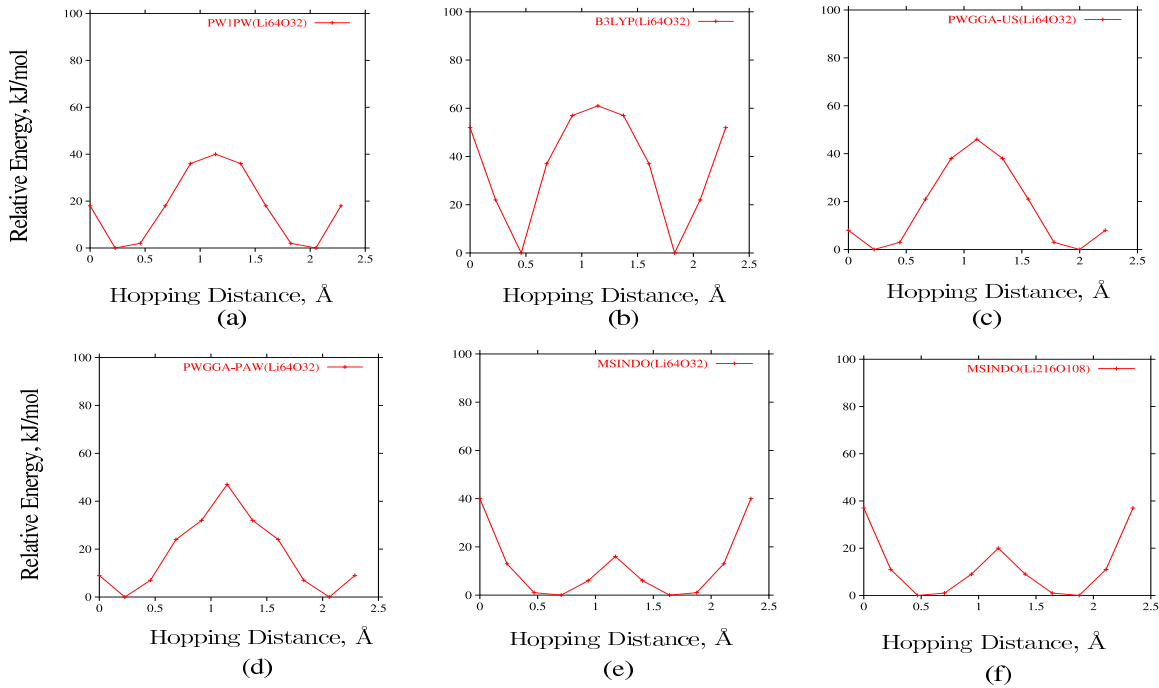


Figure 5.14: Potential energy curves of Li^+ ion migration for unrelaxed systems, (a) PW1PW (b) B3LYP, (c) PWGGA-US, (d) PWGGA-PAW, (e) MSINDO-CCM for $\text{Li}_{64}\text{O}_{32}$ and (f) MSINDO-CCM for $\text{Li}_{216}\text{O}_{108}$

Relaxation of the first nearest neighbors

To investigate the relaxation effect on the diffusion of a Li^+ ion, first the nearest neighbors of the defect and the migrating ion were relaxed. Both are surrounded by four oxygens in the first coordination shell. The migrating Li^+ ion and the cation vacancy thus have six oxygens as nearest neighbors of which two oxygens are common or bridging between the migrating Li^+ ion and the cation vacancy (Fig. 5.15). In the defective structure, one unpaired electron is localized on one of these oxygens, mainly in the $2p$ orbitals. The same situation was observed in recent DFT investigations for the Li^+ ion diffusion in Li_2O [84, 85].

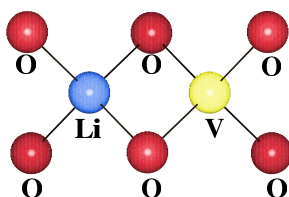


Figure 5.15: The first nearest neighbors of the migrating Li^+ ion and cation vacancy (V).

In Fig. 5.16, the energy curves of this level of relaxation are shown. In Table 5.18, the calculated activation energies obtained with different methods are compared with the experimental value.

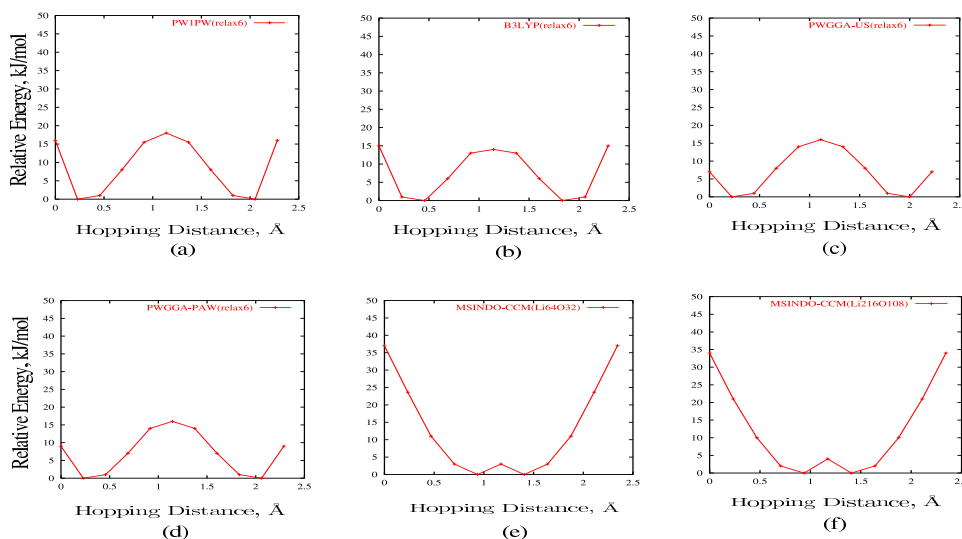


Figure 5.16: Potential energy curves for the systems with relaxation of the first nearest neighbors (a) PW1PW (b) B3LYP, (c) PWGGA-US, (d) PWGGA-PAW, (e) MSINDO-CCM for $\text{Li}_{64}\text{O}_{32}$ and (f) MSINDO-CCM for $\text{Li}_{216}\text{O}_{108}$

In all cases, the barrier is considerably reduced compared to the unrelaxed structures (Table 5.17). The MSINDO E_A value is much lower than the experimental value. The DFT methods are also giving small values of E_A .

Table 5.18: Comparison of calculated activation energy, E_A (eV) for the systems with relaxation of nearest neighbors

Method	Supercell	E_A
PW1PW	$\text{Li}_{64}\text{O}_{32}$	0.17
B3LYP	$\text{Li}_{64}\text{O}_{32}$	0.16
PWGGA-US	$\text{Li}_{64}\text{O}_{32}$	0.16
PWGGA-PAW	$\text{Li}_{64}\text{O}_{32}$	0.17
MSINDO-CCM	$\text{Li}_{64}\text{O}_{32}$	0.03
MSINDO-CCM	$\text{Li}_{216}\text{O}_{108}$	0.04
Exp.		0.31 [66]

Relaxation of all atoms

94 atoms of the $\text{Li}_{64}\text{O}_{32}$ supercell surrounding the migrating Li^+ ion and cation vacancy were relaxed for the calculation of activation energy for the diffusion of Li^+ ion. In the MSINDO-CCM calculation, full relaxation of 94 atoms in the $\text{Li}_{64}\text{O}_{32}$ cluster and of 322 atoms in the $\text{Li}_{216}\text{O}_{108}$ cluster leads to severe distortions of the lattice. This must be considered as an artefact of the implemented model. In order to avoid this problem, a limited relaxation of 28 atoms for the $\text{Li}_{64}\text{O}_{32}$ cluster and of 74 atoms for the $\text{Li}_{216}\text{O}_{108}$ cluster was performed.

In Fig. 5.17, potential curves for Li movement are shown for all methods. The activation energy is calculated as before. In Table 5.19, the calculated values of E_A with different methods are presented and compared with the experimental value. It can be seen that MSINDO does not reproduce the experimental E_A for the Li^+ ion diffusion in Li_2O . The minimum structure is found for a structure with the Li^+ on an interstitial position between the regular sites which is the transition structure for all other methods. Again this must be considered as an artefact of the present implementation of the CCM in MSINDO.

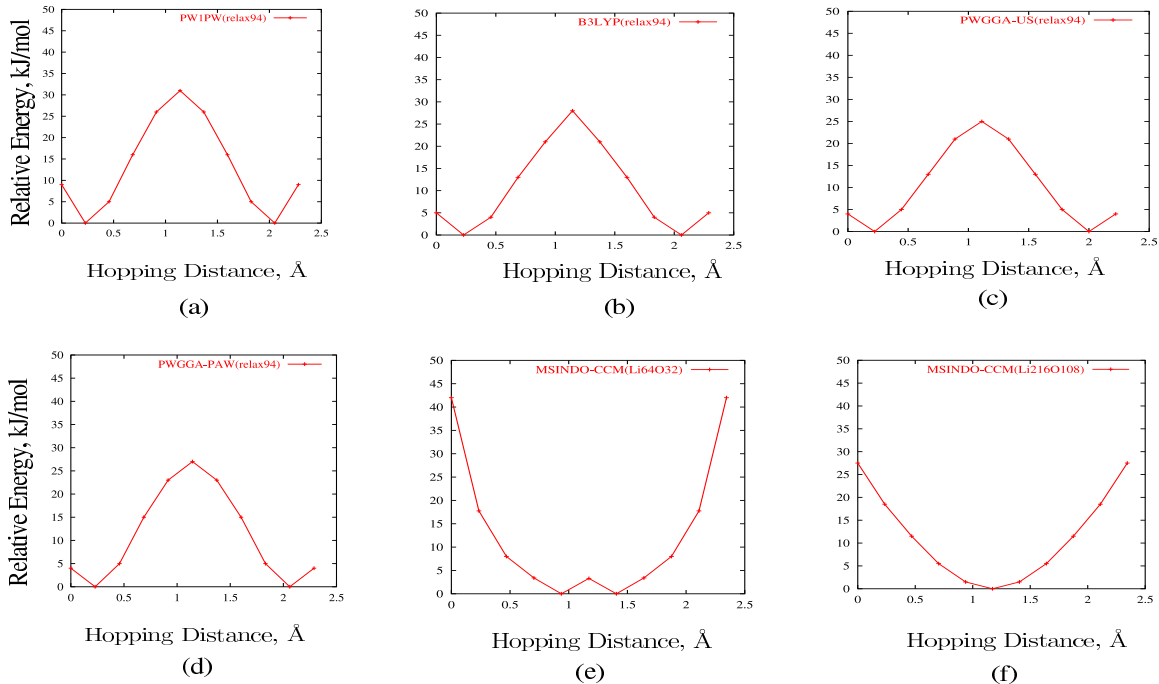


Figure 5.17: Potential curves for the Li migration for the fully relaxed systems (a) PW1PW (b) B3LYP, (c) PWGGA-US, (d) PWGGA-PAW, (e) MSINDO-CCM for $\text{Li}_{64}\text{O}_{32}$ and (f) MSINDO-CCM for $\text{Li}_{216}\text{O}_{108}$

On the other hand, all DFT methods give activation energies in agreement with the experimental value at this relaxation level. The hybrid methods PW1PW and B3LYP have the best agreement with the experimental value (Table 5.19). A similar activation energy (0.34 eV) was obtained with the DFT-LDA approach [84, 85]. Thus all DFT methods are giving a similar trend for the Li^+ ion diffusion in Li_2O , whereas MSINDO-CCM approach fails to explain this behavior.

Table 5.19: Comparison of calculated activation energy, E_A (eV) for fully relaxed systems with experimental value

Method	Supercell	E_A
PW1PW	$\text{Li}_{64}\text{O}_{32}$	0.33
B3LYP	$\text{Li}_{64}\text{O}_{32}$	0.29
PWGGA-US	$\text{Li}_{64}\text{O}_{32}$	0.25
PWGGA-PAW	$\text{Li}_{64}\text{O}_{32}$	0.28
MSINDO-CCM	$\text{Li}_{64}\text{O}_{32}$	0.02
MSINDO-CCM	$\text{Li}_{216}\text{O}_{108}$	0.00
Exp.		0.31 [66]

6 Bulk Properties of B_2O_3

B_2O_3 plays an important role in modern research of ceramic and glass technology [64–66, 107]. There are two polymorphs [108–110] in which boron atoms have different coordination numbers. At normal pressure, B_2O_3 has a trigonal structure (B_2O_3 -I) characterized by a three-dimensional network of corner-linked BO_3 triangles [108, 109]. At high pressure, there is an orthorhombic modification (B_2O_3 -II) consisting of a framework of linked BO_4 tetrahedra [110]. Neither of these two crystalline forms occurs naturally, since B_2O_3 does not crystallize readily from the highly dehydrated viscous melts [111]. Furthermore, it is not even easy to prepare crystals under special conditions and to measure their properties. For this reason in spite of the vast importance of borate glasses, there exist very few investigations on crystalline B_2O_3 .

In this study the theoretical investigation of the geometrical, energetic and electronic properties of the low-pressure phase of B_2O_3 (B_2O_3 -I) is presented. A new crystal structure refinement [109] based on published X-ray data [108] shows that B_2O_3 -I has the correct space group (152) $P3_121$ instead of (144) $P3_1$ as suggested earlier [108]. In B_2O_3 -I of space group $P3_121$ [109], the BO_3 triangles are almost planar, the sum of the three O-B-O angles being $359.8(6)^\circ$. The two crystallographically independent O atoms are coordinated to two B atoms (Fig. 6.18).

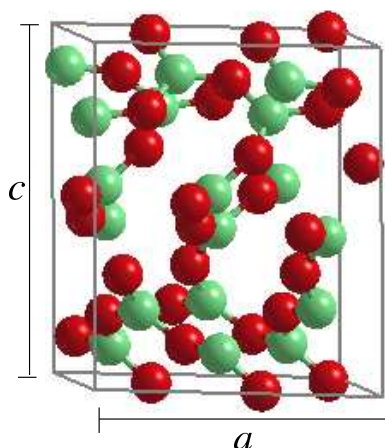


Figure 6.18: B_2O_3 conventional unit cell for $P3_121$ space group. Red spheres represent the oxygens and green spheres represent the boron atoms

In the previously suggested $P3_1$ structure [108], the three B-O bond lengths within the BO_3 triangle are not equidistant. The B atoms can be separated into types B_1 and B_2 which give two slightly different BO_3 units (Fig. 6.19). The three O atoms bonded to

B_1 (B_2) are labeled as O_1 , O_2 , and O_3 (O'_1 , O'_2 , and O'_3). The B atom is at the center of three nearest O with an average O-B-O angle of 119.97° and an average bridging angle for B-O-B of 130.71° . The coordination figures in the $P3_121$ structure are more regular than in the $P3_1$ structure. The experimental lattice parameters [108, 109] of

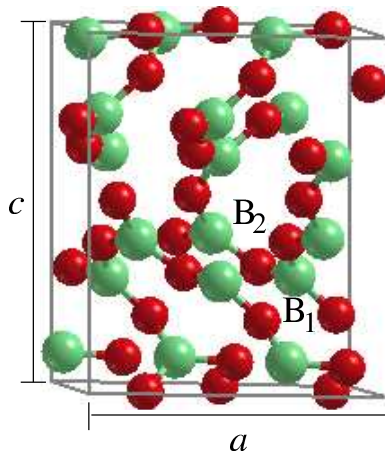


Figure 6.19: B_2O_3 conventional unit cell for $P3_1$ space group. Red spheres represent the oxygens and green spheres represent the boron atoms

trigonal B_2O_3 -I are $a=4.3358 \text{ \AA}$ and $c=8.3397 \text{ \AA}$. The experimental value of the heat of atomization is 3127 kJ/mol [94]. Several experimental [112, 113] and theoretical investigations [114, 115] were performed for the electronic structure of B_2O_3 -I. No experimental value for the band gap is available in the literature. Li *et al.* [114] suggested that the band gap is 6.2 eV based on calculations at DFT LDA level.

In the present study, the investigation was done for both proposed structures ($P3_121$ and $P3_1$) of crystalline B_2O_3 -I. The calculations on the lattice parameters, bond lengths, binding energy per B_2O_3 unit (E_u) and the band gap (E_g) are performed by applying the methods and models which were discussed in the previous chapters. The optimization of B_2O_3 structure was performed with the CRYSTAL03 package by exploiting the new feature of analytical gradients. First a full optimization of atomic fractional coordinates was performed keeping the lattice vectors fixed at the experimental values. Starting from the then obtained internal coordinates, the lengths of the lattice vectors were optimized. This procedure was repeated iteratively until the minimum of total energy was obtained. For boron, a 6-21G* basis [116] is used which is a modification of the original 6-21G [117] basis set, where the outer *sp* exponent is optimized for solid BN. For O, a 8-411G* [100] basis is used. Similar optimization was performed with

VASP using energy cutoff E2. For the MSINDO-CCM, the calculations were performed with the standard empirical parameters [14, 22] for a $B_{48}O_{72}$ cluster.

6.1 B_2O_3 with P3₁21 space group

The calculated values for lattice parameters a and c , bond distances, E_u and E_g are compared with experimental values in Table 6.20. The LCAO based PWGGA gives the largest values for a and c among all methods, the deviations from the experimental values are $+0.05 \text{ \AA}$ and $+0.10 \text{ \AA}$ respectively. MSINDO-CCM gives the smallest values, $\Delta a = -0.06 \text{ \AA}$ and $\Delta c = -0.3 \text{ \AA}$. Both plane wave based methods, PWGGA-US and PWGGA-PAW are giving similar agreement with the experimental values for a and c . The best agreement with the experimental values is obtained with the hybrid PW1PW approach which overestimates a and c by 0.01 \AA and 0.05 \AA , respectively. The hybrid B3LYP gives larger a ($\Delta a = +0.02 \text{ \AA}$) and c ($\Delta c = +0.09 \text{ \AA}$) values.

The experimental average B-O bond distance, $R(\text{B-O})$ is 1.368 \AA [109]. All the methods give large values of B-O bond distances compared to the experiment. The deviation is less than 0.014 \AA (or 1.0%) for $R(\text{B-O})$. As for the lattice parameters, PWGGA gives the largest value of $R(\text{B-O})$. PWGGA-US and PWGGA-PAW methods give similar agreement to the experiment for the B-O bond distances. The best agreement was obtained with PW1PW which deviates from the experimental distances of B-O₁, B-O₂ and B-O₃ by only $+0.001 \text{ \AA}$, $+0.014 \text{ \AA}$, and $+0.001 \text{ \AA}$, respectively. The second best agreement was obtained with the MSINDO-CCM which deviates the experimental $R(\text{B-O})$ by 0.007 \AA . The other hybrid method B3LYP also gives close agreement to the experiment, deviation is 0.008 \AA .

The binding energy per B_2O_3 unit (E_u) was calculated for all methods in the same way as it was done for Li_2O (see sections 5.1.2 and 5.2). For both PWGGA-US and PWGGA-PAW implementations in VASP, atomic reference energy of B atom was calculated by using pseudo lattice constant of 15 \AA . PW1PW approach gives the best agreement to the experimental value for E_u . The deviation is -35 kJ/mol (Table 6.20). MSINDO gives the second best agreement to the experiment, deviating by -45 kJ/mol . B3LYP underestimates the experimental E_u by 65 kJ/mol . The three Perdew-Wang implementations, PWGGA, PWGGA-US and PWGGA-PAW give different E_u values. Among them the best agreement to the experiment is obtained with the LCAO based

PWGGA approach which gives a deviation of -103 kJ/mol. The deviations are large for PWGGA-US and PWGGA-PAW, namely by -142 kJ/mol and -241 kJ/mol, respectively. The reasons of this difference can be due to the incompleteness of the basis set used for the CRYSTAL-PWGGA or due to the influence of the effective potentials in the plane wave based PWGGA-US and PWGGA-PAW. The E_u obtained with PWGGA-US and PWGGA-PAW differ by 99 kJ/mol. This difference is more significant than in the case of E_u of Li_2O (see Table 5.8). So it can be assumed that this is due to the description of core electrons of B atom, which affects the binding energy.

Table 6.20: Comparison of calculated lattice vectors a and c (\AA), bond distances (\AA), E_u (kJ/mol) and E_g (eV) with the experimental values for B_2O_3 of $P3_121$ space group

Properties	PWGGA	PWGGA-US	PWGGA-PAW	PW1PW	B3LYP	MSINDO	Exp.
a	4.39	4.36	4.36	4.35	4.36	4.28	4.34 ^a
c	8.44	8.39	8.38	8.39	8.43	8.04	8.34 ^a
bonds (\AA)							
B-O ₁	1.385	1.380	1.384	1.376	1.389	1.383	1.375 ^a
B-O ₂	1.379	1.371	1.376	1.370	1.366	1.371	1.356 ^a
B-O ₃	1.383	1.379	1.381	1.374	1.372	1.372	1.373 ^a
R(B-O)	1.382	1.377	1.380	1.373	1.376	1.375	1.368 ^a
E_u	-3230.4	-3268.7	-3368.9	-3162.4	-3062.2	-3172.4	-3127 ^b
E_g	6.5	6.2	6.1	9.1	8.8	10.5	(6.2) ^c

^a Ref. [109]

^b Ref. [94]

^c LDA result [114]

The calculated values of band gap E_g with all the methods are presented in Table 6.20. E_g is calculated from the total density of states (TDOS). There is no experimental value of E_g to compare. So the calculated results are compared among themselves. Since PW1PW approach gives the best agreement for E_g in the case of Li_2O (see Table 5.7), this method is chosen as reference here. The PW1PW E_g is 9.1 eV, which is higher than the $E_g=6.2$ eV obtained at LDA level by Li *et al.* [114]. This is reasonable, since generally the band gap is underestimated by the DFT local density approximation (LDA) [75, 77]. The best agreement to the PW1PW result is obtained with B3LYP

with a difference of -0.3 eV. PWGGA-US and PWGGA-PAW are giving similar values to each other and to the previous LDA result [114]. The E_g value calculated with the LCAO based PWGGA is 6.5 eV, which differs from PWGGA-US and PWGGA-PAW approaches. This is in line with the previous investigation of Li_2O (see Table 5.8). The E_g value obtained with MSINDO-CCM is 10.5 eV, which is 1.4 eV larger than that with PW1PW.

The TDOS and PDOS of B_2O_3 calculated at the PW1PW level are shown in Fig. 6.20 together with an experimental PE spectrum [113]. There is good agreement of the band widths and the relative positions of the two main peaks between the theoretical and the experimental spectra.

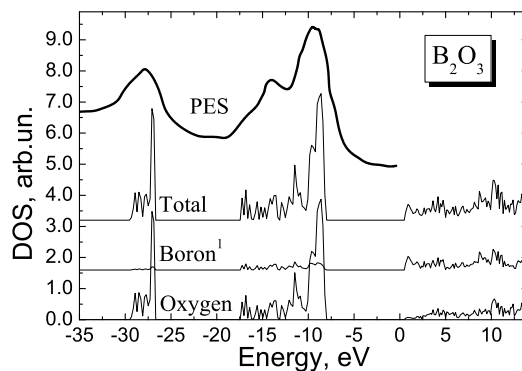


Figure 6.20: Density of states of B_2O_3 obtained with the PW1PW method. For comparison the experimental PES spectrum [113] is also shown.

The oxygen $2p$ states have the major contribution in the VB, similar to Li_2O . The CB consists of boron $2p$ states. The semi-core states at about -27 eV correspond to $2s$ oxygen orbitals.

The electron charge density distribution was calculated along the B-O bond. As in the case of Li_2O , PW1PW method is taken as an example (Fig. 6.21). The charge distribution

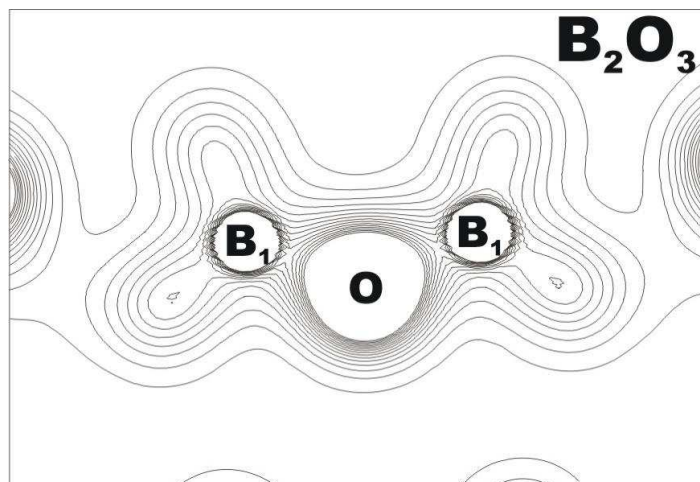


Figure 6.21: Electronic charge density distribution for B_2O_3 .

is deformed from the oxygen atom towards the boron atom. This shows that the B-O bond has covalent character.

6.2 Comparison between $P3_121$ and $P3_1$ space group

The bulk properties of B_2O_3 -I with $P3_1$ space group were calculated with all the approaches discussed in the previous section. In Table 6.21, the calculated values are compared with experimental values. As for $P3_121$ space group, PW1PW gives the best reproduction of bulk properties of $P3_1$ space group. All the other methods give the similar deviations for lattice vectors a and c , bond distances, binding energy per unit of B_2O_3 E_u and band gap E_g , as in the case of $P3_121$ space group.

Table 6.21: Comparison of calculated lattice vectors a and c (Å), bond distances (Å), E_u (kJ/mol) and E_g (eV) with the experimental values for B_2O_3 of $P3_1$ space group

Properties	PWGGA	PWGGA-US	PWGGA-PAW	PW1PW	B3LYP	MSINDO	Exp.
a	4.37	4.36	4.36	4.37	4.35	4.27	4.34 ^a
c	8.52	8.38	8.38	8.40	8.44	8.10	8.34 ^a
bonds (Å)							
B ₁ -O ₁	1.394	1.380	1.384	1.383	1.390	1.383	1.404 ^a
B ₁ -O ₂	1.389	1.379	1.381	1.380	1.389	1.373	1.366 ^a
B ₁ -O ₃	1.374	1.373	1.376	1.375	1.382	1.370	1.337 ^a
B ₂ -O' ₁	1.373	1.372	1.376	1.378	1.380	1.369	1.336 ^a
B ₂ -O' ₂	1.394	1.379	1.383	1.385	1.390	1.383	1.401 ^a
B ₂ -O' ₃	1.388	1.373	1.382	1.382	1.389	1.373	1.384 ^a
E_u	-3229.7	-3268.5	-3368.6	-3160.7	-3059.3	-3171.5	-3127 ^b
E_g	6.4	6.5	6.3	8.8	8.8	10.5	(6.2) ^c

^a Ref. [108]

^b Ref. [94]

^c LDA result [114]

Comparing the structural properties and the small difference of E_u between the $P3_121$ and $P3_1$, it can be said that these two structures are practically the same. It can be observed from Tables 6.20 and 6.21 that there is an energy minimum for the structure with space group $P3_121$. With all the methods, its E_u is lower by ≈ 1 kJ/mol. This confirms that the stable structure is the recently proposed structure [109] with the $P3_121$ space group.

7 Bulk Properties of $\text{Li}_2\text{B}_4\text{O}_7$

The binary $\text{Li}_2\text{O}-\text{B}_2\text{O}_3$ system is characterized by the formation of nine lithium borate compounds, namely Li_3BO_3 , $\alpha\text{-Li}_4\text{B}_2\text{O}_5$, $\beta\text{-Li}_4\text{B}_2\text{O}_5$, $\text{Li}_6\text{B}_4\text{O}_9$, LiBO_2 , $\text{Li}_2\text{B}_4\text{O}_7$, $\text{Li}_3\text{B}_7\text{O}_{12}$, LiB_3O_5 and $\text{Li}_2\text{B}_8\text{O}_{13}$ [118–121]. Only Li_3BO_3 (lithium orthoborate), $\text{Li}_6\text{B}_4\text{O}_9$, LiBO_2 (lithium metaborate), $\text{Li}_2\text{B}_4\text{O}_7$ (lithium tetraborate) and LiB_3O_5 (lithium triborate) are stable at room temperature. A common feature of all anhydrous lithium borate crystalline structures is the boron-oxygen anion subsystem. This subsystem forms a covalent anionic framework with BO_3 -triangles and BO_4 -tetrahedra that have a polycondensation susceptibility [122]. Lithium ions, in turn, are connected with the anion subsystem electrostatically. The loose connectivity results in the appearance of ionic conductivity and superionic properties.

Crystalline lithium tetraborate (LTB) $\text{Li}_2\text{B}_4\text{O}_7$ is of considerable interest due to its practical applications. LTB has important physical properties [123], such as high coefficient of electrochemical coupling, low velocity of propagation of surface acoustic waves, zero thermal expansion coefficient, high mechanical strength, and low electrical conductivity at room temperature. It is used for laser radiation converters [124], as substrate for thermostable surface [125–127] and bulk [128] acoustic wave-based devices, as piezoelectric nonlinear optical device for second harmonic generation [129–131], in electroacoustic devices [132–134], as pyroelectric sensor [134, 135] and in thermoluminescent dosimetry of X-ray, gamma and neutron radiation [136–138]. LTB was also found to be a Li^+ ion conductor along the (001) direction (polar axis) [139–147].

In this study, a theoretical investigation of the bulk properties is performed for the single crystal of $\text{Li}_2\text{B}_4\text{O}_7$ which can be regarded as a possible structure in the $\text{Li}_2\text{O}:\text{B}_2\text{O}_3$ nanocomposite interface region. The accuracy of the various approaches is tested by comparison to available experiments.

$\text{Li}_2\text{B}_4\text{O}_7$ belongs to space group $\text{I4}_1\text{cd}$ and has 104 atoms per unit cell [148] (Fig. 7.22(b)). The measured lattice parameters are $a = 9.48 \text{ \AA}$ and $c = 10.29 \text{ \AA}$. The main structural pattern is a $[\text{B}_4\text{O}_9]^{6-}$ complex (Fig. 7.22(a)) which consists of two planar trigonal (BO_3) and two tetrahedral (BO_4) units. The lithium atoms are located at interstices [148].

The experimental value of the heat of atomization of crystalline $\text{Li}_2\text{B}_4\text{O}_7$ is 7658 kJ/mol

[149]. A limited number of experimental investigations on the electronic structure [150–152] are available in the literature. The electronic structure, namely the valence band, of LTB has been experimentally studied by X-ray photoelectron spectroscopy (XPS) [151] in combination with a theoretical investigation based on local density approximation (LDA) calculations of the free anion $[\text{B}_4\text{O}_9]^{6-}$. The LTB band structure was calculated [152] by a modified LCAO method using symmetrized Bloch functions, but only the results for the valence band were presented. To my best knowledge there are no experimental and theoretical results in the literature about the value of the band gap (E_g). It is only known that the fundamental absorption edge is 7.3 eV [150] which is comparable to the value of ≈ 7.9 eV found by reflection spectroscopy [152]. Therefore E_g of LTB is estimated based on the measured fundamental absorption (FA) energy, 7.3 eV [150], and experimental and calculated band gaps and FA energies which are available for other alkali borate crystals. In a previous theoretical study of LiB_3O_5 [150] an extrapolation scheme was suggested to obtain an estimation for the experimental band gap from the experimental value of FA 7.8 eV [153]. In this way $E_g(\text{LiB}_3\text{O}_5) \approx 9.5$ eV was obtained. Taking into account the similarities between $\text{Li}_2\text{B}_4\text{O}_7$ and LiB_3O_5 for luminescence properties and optical spectra, and that the FA energy (FAE) of LTB is smaller than FAE of LiB_3O_5 by 0.5 eV, the E_g of LTB is assumed to be about 9.0 eV. This approximate value is compared with the calculated values in the present study.

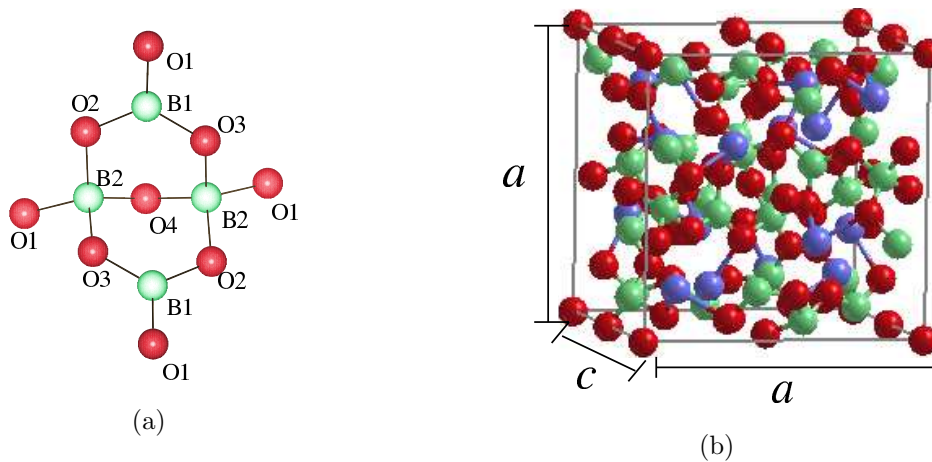


Figure 7.22: The main structural pattern $[\text{B}_4\text{O}_9]^{6-}$ (a) and the unit cell (b) of LTB.

Red spheres represent oxygen atoms, green spheres represent boron atoms and blue spheres represent lithium atoms

7.1 Structure Optimization

The optimized lattice parameters, bond distances and angles as obtained with PW1PW, PWGGA and B3LYP using CRYSTAL03, with PWGGA-US, PWGGA-PAW using VASP, and with MSINDO, are given in Table 7.22 together with the corresponding experimental values [148]. The numbering of the Li, B and O atoms is shown in Fig. 7.22(a). The optimization of atomic fractional coordinates and lattice vectors was performed in the same way as it was done for B_2O_3 (see chapter 6). In the MSINDO structure optimization the cyclic cluster $\text{Li}_{16}\text{B}_{32}\text{O}_{56}$ was used which corresponds to the conventional unit cell of LTB (Fig. 7.22(b)). The calculations were performed with the standard empirical parameters [14, 22]. For the DFT methods, the primitive LTB unit cell was used. In the CRYSTAL-DFT calculations, the basis sets used here correspond to BS B, BS C and BS D for Li_2O (see chapter 5.2). For boron, a 6-21G* basis [116] is used for BS B. In the extended sets (BS C and BS D), a 6-21G(2d) basis is used which contains an additional polarization function in the 6-21G* basis.

The best agreement for a and c is obtained with the two hybrid methods PW1PW ($\Delta a = +0.02 \text{ \AA}$, $\Delta c = +0.03 \text{ \AA}$) and B3LYP ($\Delta a = +0.04 \text{ \AA}$, $\Delta c = +0.01 \text{ \AA}$). The results of the LCAO implementation (in CRYSTAL) and the plane wave implementations (PWGGA-US, PWGGA-PAW in VASP) of the PWGGA method are relatively similar. This is particularly the case if ultrasoft pseudopotentials are used (PWGGA-US). Here the differences between CRYSTAL and VASP results are smaller than 0.01 \AA . The deviations from experiment are between 0.04 \AA and 0.05 \AA . The PWGGA-PAW approach gives too large lattice parameters with respect to the experimental values, namely a is overestimated by 0.08 \AA and c is overestimated by 0.09 \AA . It can be observed from Table 7.22 that structural properties are already converged with the energy cutoff E2 for the plane wave based approaches and with BS C for the LCAO based approaches. With MSINDO, the lattice parameter a is underestimated by 0.04 \AA and c is overestimated by 0.15 \AA . The calculated bond lengths and angles for all methods agree well with the experimental values (Table 7.22). The deviation of the calculated boron-oxygen bond distances for three-fold coordinated boron atoms (B_1 , see Fig. 7.22(a)) does not exceed 0.035 \AA . The best agreement was found for PW1PW where the deviation is less than 0.004 \AA . For the plane wave based PWGGA implementations (PWGGA-PAW and PWGGA-US), this deviation is not more than 0.01 \AA ,

whereas the LCAO-based PWGGA implementation overestimates $\text{B}_1\text{-O}$ bond lengths by 0.02 Å. For B3LYP, the deviation of $\text{B}_1\text{-O}$ bond lengths is less than 0.015 Å. The semiempirical method MSINDO performs similar as the hybrid methods. The same trends were observed for the $\text{B}_2\text{-O}$ bond lengths, where the boron atom is four-fold coordinated. The experimentally obtained distances $\text{B}_2\text{-O}_2$ and $\text{B}_2\text{-O}_3$ are larger than the corresponding distances $\text{B}_2\text{-O}_1$ and $\text{B}_2\text{-O}_4$. The four lithium-oxygen distances range from 1.94 to 2.18 Å [148]. The worst result for these bond lengths is obtained by the semiempirical method, where the error for the Li-O_1 bond (Table 7.22) is 0.22 Å. Among the DFT methods, PWGGA-US gives the worst values of lithium-oxygen distances. The Li-O_1 bond length is overestimated by 0.13 Å and $R(\text{Li-O}_3)$ is underestimated by 0.19 Å. A possible explanation is that the US pseudopotential gives an insufficient description of the Li core electrons and this deficiency is partly removed by the PAW potential where deviations of $R(\text{Li-O})$ are much smaller (Table 7.22).

All calculated bond angles show good agreement with experimental data. The errors are smaller than 1.6 %. For brevity, the comparison is shown only with the experimental angles of $\text{B}_1\text{-O}_1\text{-B}_2$, $\text{B}_1\text{-O}_2\text{-B}_2$, $\text{B}_1\text{-O}_3\text{-B}_2$ and $\text{B}_2\text{-O}_4\text{-B}_2$ (Table 7.22) The agreement for the other angles is similar.

Table 7.22: Structural properties of solid $\text{Li}_2\text{B}_4\text{O}_7$. Comparison of calculated and experimental lattice vectors a and c , bond distances (\AA), and angles (degrees). For the numbering of the atoms see Figure 7.22(a)

Methods Basis Set/Energy Cutoff	PWGGA			PWGGA-PAW			PWGGA-US			PW1PW			B3LYP			MSINDO	Exp. ^a
	B	C	D	E1	E2	E3	E1	E2	E3	B	C	D	B	C	D		
a	9.53	9.57	9.55	9.42	9.57	9.56	9.41	9.52	9.51	9.50	9.50	9.50	9.52	9.55	9.55	9.44	9.48
c	10.32	10.33	10.33	10.22	10.39	10.38	10.22	10.33	10.32	10.32	10.34	10.33	10.30	10.34	10.39	10.44	10.29
bonds																	
B ₁ -O ₁	1.372	1.369	1.372	1.353	1.365	1.364	1.352	1.363	1.363	1.361	1.360	1.358	1.362	1.365	1.365	1.360	1.355
B ₁ -O ₂	1.393	1.394	1.394	1.368	1.381	1.380	1.368	1.377	1.376	1.378	1.375	1.375	1.384	1.384	1.386	1.385	1.371
B ₁ -O ₃	1.396	1.395	1.396	1.374	1.386	1.385	1.375	1.383	1.382	1.381	1.379	1.379	1.388	1.387	1.389	1.371	1.374
B ₂ -O ₁	1.470	1.459	1.458	1.449	1.454	1.454	1.437	1.441	1.441	1.451	1.450	1.446	1.451	1.449	1.451	1.442	1.452
B ₂ -O ₂	1.527	1.524	1.526	1.505	1.522	1.519	1.511	1.528	1.526	1.510	1.510	1.509	1.517	1.521	1.520	1.498	1.506
B ₂ -O ₃	1.517	1.518	1.519	1.502	1.517	1.518	1.507	1.515	1.514	1.508	1.508	1.504	1.512	1.514	1.519	1.488	1.501
B ₂ -O ₄	1.463	1.467	1.471	1.451	1.464	1.462	1.450	1.458	1.459	1.463	1.462	1.460	1.464	1.465	1.466	1.447	1.454
Li-O ₁	2.153	2.167	2.119	2.110	2.107	2.118	2.273	2.303	2.300	2.082	2.090	2.090	2.079	2.098	2.103	2.394	2.170
Li-O ₂	1.974	1.977	1.976	1.959	1.979	1.980	1.770	1.826	1.825	1.966	1.970	1.964	1.970	1.978	1.971	2.027	1.967
Li-O ₃	2.012/ 2.082	2.009/ 2.092	2.001/ 2.087	2.005/ 2.067	2.018/ 2.102	2.021/ 2.098	1.847/ 2.065	1.836/ 2.051	1.836/ 2.045	2.005/ 2.086	2.008/ 2.088	1.999/ 2.069	1.995/ 2.085	2.004/ 2.097	1.995/ 2.070	2.102/ 2.103	2.027/ 2.080
angles																	
B ₁ -O ₁ -B ₂	124	125	124	125	126	126	124	125	125	125	125	126	125	125	125	126	126
B ₁ -O ₂ -B ₂	115	115	115	116	115	116	115	115	115	116	116	116	115	116	115	119	116
B ₁ -O ₃ -B ₂	119	119	119	120	119	120	119	119	119	119	120	119	119	119	119	121	120
B ₂ -O ₄ -B ₂	108	110	109	109	109	109	109	109	109	109	109	109	109	109	109	110	109

^a Ref. [148]

7.2 Binding Energy

In the table 7.23, the calculated values of binding energy per $\text{Li}_2\text{B}_4\text{O}_7$ formula unit (E_u) are compared with the negative value of experimental heat of atomization [149] of crystalline $\text{Li}_2\text{B}_4\text{O}_7$.

Table 7.23: Comparison of calculated binding energies per $\text{Li}_2\text{B}_4\text{O}_7$ unit E_u (kJ/mol) with the experimental value

Method	BS/ E_{cut}	E_u
PWGGA	B	-7840
	C	-7829
	D	-7829
PWGGA-PAW	E1	-8137
	E2	-8127
	E3	-8119
PWGGA-US	E1	-7998
	E2	-7932
	E3	-7932
PW1PW	B	-7674
	C	-7674
	D	-7678
B3LYP	B	-7450
	C	-7453
	D	-7451
MSINDO		-8128
Exp. ^a		-7658

^a Ref. [149]

The PW1PW approach gives the best agreement for E_u with the experimental value with a deviation of only -20 kJ/mol (Table 7.23). As for B_2O_3 , PWGGA, PWGGA-US and PWGGA-PAW give different E_u values of LTB. Among them, the CRYSTAL PWGGA implementation gives the best agreement for E_u , -7829 kJ/mol, deviating from the experimental value by -171 kJ/mol. PWGGA-US and PWGGA-PAW give more negative values, namely by -274 kJ/mol and -461 kJ/mol, respectively. The reason of these differences between the LCAO and plane wave based cohesive energies could be attributed to the fact that the atomic reference energies obtained with plane waves are too high. The difference between E_u obtained with PWGGA-PAW

and PWGGA-US indicates the influence of the effective potentials in the plane wave program VASP.

The convergence of atomic reference energies are tested with respect to the lattice parameter and energy cutoff in the atomic plane wave calculations. The atomic energies of ^3O atom, ^2Li atom, and ^2B atom at UKS level change only by up to 5 kJ/mol with PWGGA-PAW, and by less than 10 kJ/mol with PWGGA-US when the standard energy cutoffs are increased. This effect cannot account for the observed differences between E_u obtained with the three PWGGA implementations. Therefore, it can be concluded that the differences between CRYSTAL and VASP results are mainly due to the description of core electrons. This mainly affects binding energies, while geometry parameters are less sensitive.

The B3LYP hybrid method gives 207 kJ/mol smaller absolute value of E_u than the experimental value. This trend is in line with previous studies of MgO, NiO, and CoO [37]. The MSINDO result for E_u is in the range of the first-principles methods.

7.3 Band Structure and Density of States

The band structure was calculated along the path that contains the highest number of high-symmetry points of the Brillouin zone [103] ($M \rightarrow \Gamma \rightarrow X \rightarrow P \rightarrow N$). The calculated results of the electronic structure for the PW1PW method with BS D are shown in Fig. 7.23. This method was chosen since it gave best agreement with experiment for the electronic structure of Li_2O , B_2O_3 (see chapters 5.2 and 6). Other methods give the same qualitative band structure, only the bands are shifted therefore the value of the band gap changes, as will be shown below.

According to calculated results, LTB is a wide gap insulator. Both the valence band (VB) and the conduction band (CB) have a small dispersion as found for similar crystals $\alpha\text{-B}_2\text{O}_3$, $\beta\text{-B}_2\text{O}_3$ [114] and LiB_3O_5 [154].

The total (TDOS) and projected density of states (PDOS) were calculated at PW1PW level using the Fourier-Legendre technique [104] with a *Monkhorst net* [105] using shrinking factors $s=8$.

The calculated TDOS of LTB compared with X-ray photoelectron spectrum [151] is shown on Fig. 7.23(b). A good agreement with experiment was obtained for the band widths and the interband distances within the VB. The valence band width is about 10

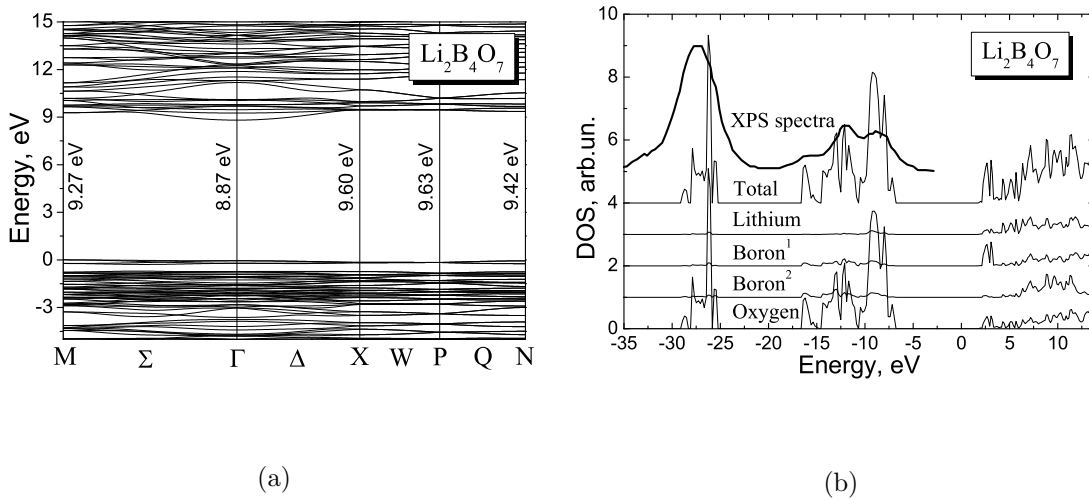


Figure 7.23: Electronic band structure and density of states of LTB obtained with the PW1PW method using BS D. For comparison the X-ray photoelectron spectrum [151] is also shown.

eV. The difference between the upper and lower valence band, which is mainly formed by O 2s states, is about 8 eV.

The analysis of DOS shows that LTB has very sharp VB and CB edges. The states near the VB top are mainly created by oxygen 2p states. The contributions from atomic orbitals of other atoms (Li, B₁ - boron in BO₃, and B₂ - boron in BO₄) are ten times smaller than the oxygen PDOS. The bottom of the CB is dominated by contributions from B₁ atoms.

Calculated values for vertical VB-CB transitions in $\text{Li}_2\text{B}_4\text{O}_7$ and minimal transition energies are presented in Table 7.24. All considered methods indicate that LTB has an indirect ($M - \Gamma$) band gap. However, the direct $\Gamma - \Gamma$ transition energy is only slightly larger. The difference does not exceed 0.05 eV. The calculated values of E_g vary from 6.17 eV (PWGGA-PAW) to 8.81 eV (PW1PW). The extrapolated experimental $E_g=9.0$ eV agrees well with the PW1PW and B3LYP results, ≈ 8.8 eV (Table 7.24, BS D), whereas the corresponding PWGGA, PWGGA-US and PWGGA-PAW results, 6.73 eV, 6.20 and 6.17 eV, are considerably too small. It should be noted that the MSINDO band gap, 9.7 eV, is in better agreement with experiment than the corresponding PWGGA, PWGGA-US and PWGGA-PAW results.

The three PWGGA implementations, CRYSTAL PWGGA, PWGGA-PAW and PWGGA-

Table 7.24: The values of vertical electronic transitions and minimal transition (MT) energies (eV) for $\text{Li}_2\text{B}_4\text{O}_7$ calculated with different methods

Transition	PWGGA			PWGGA-PAW			PWGGA-US			PW1PW			B3LYP			MSINDO
	B	C	D	E1	E2	E3	E1	E2	E3	B	C	D	B	C	D	
Γ Γ	7.15	6.80	6.79	6.23	6.27	6.23	6.24	6.31	6.25	9.41	8.94	8.87	9.37	8.91	8.80	
N N	7.24	7.15	7.19	7.04	7.08	7.03	7.05	7.10	7.05	9.55	9.43	9.42	9.54	9.42	9.35	
P P	7.40	7.31	7.38	7.28	7.31	7.26	7.29	7.34	7.28	9.75	9.64	9.63	9.71	9.60	9.53	
X X	7.35	7.27	7.35	7.18	7.22	7.17	7.18	7.24	7.18	9.72	9.61	9.60	9.67	9.56	9.50	
M M	7.19	7.00	7.05	6.93	6.96	6.92	6.94	6.99	6.94	9.42	9.29	9.27	9.40	9.27	9.21	
MT	M- Γ	M- Γ	M- Γ	M- Γ	M- Γ	M- Γ	M- Γ	M- Γ	M- Γ	M- Γ	M- Γ	M- Γ	M- Γ	M- Γ	M- Γ	9.70
	7.11	6.76	6.73	6.18	6.22	6.17	6.19	6.26	6.20	9.31	8.88	8.81	9.32	8.85	8.73	

US give similar values of the transition energies except for the $\Gamma - \Gamma$ transition (Table 7.24). For PWGGA-US and PWGGA-PAW, the $\Gamma - \Gamma$ transition energies are very close, 6.25 eV and 6.23 eV, respectively. This is considerably smaller than the 6.79 eV obtained with CRYSTAL PWGGA using the the largest basis set (BS D). The difference is ≈ 0.5 eV, which is responsible for the difference in the value of band gap (6.20 eV for PWGGA-US, 6.17 eV for PWGGA-PAW and 6.73 eV for PWGGA). The difference in $\Gamma - \Gamma$ transition energy is not due to the LCAO basis set incompleteness as the values of the transition energies are already converged with BS C.

The atomic basis set has a pronounced effect on the electronic structure. The PWGGA $\Gamma - \Gamma$ transition energy is 7.15 eV with BS B which is 0.35 eV larger than that with BS C and 0.34 eV larger than that with BS D. A similar difference is found for the band gap. This change is mainly due to the inclusion of diffuse and polarization functions in the Li and B basis sets. These orbitals are dominating at the lower part of the CB. The main effect of basis set increase is a lowering of the CB bottom while the VB top is essentially unchanged. The basis set effect is even larger for the hybrid methods, as can be seen by the differences obtained with BS B, BS C and BS D for PW1PW and B3LYP. In all cases the values are converged within 0.1 eV by the basis set C.

7.4 Electronic charge density

The electronic charge density distribution for the three main types of bonds ($\text{B}_1\text{-O}$, $\text{B}_2\text{-O}$, Li-O bonds) was calculated. Here the B3LYP method is chosen as an example. Test calculations showed that the other methods give a qualitatively similar behavior. Three planes containing $\text{O-B}_1\text{-O}$, $\text{O-B}_2\text{-O}$ and O-Li-O angles were considered. B_1 and B_2 represent the boron atoms in BO_3 and BO_4 units, respectively. The charge density distribution maps are shown in Fig. 7.24. The contour lines range from 0.0 to $0.3 \text{ e}/\text{\AA}^3$ with steps of $0.02 \text{ e}/\text{\AA}^3$.

As in the case of B_2O_3 , the charge distribution is deformed from oxygen towards the boron atoms B_1 (Fig. 7.24(a)) and B_2 (Fig. 7.24(b)). This shows that the bonds in triangular BO_3 and tetrahedral BO_4 groups have covalent character and as a result the B-O bonds are strong. As for Li_2O , the charge distribution of both Li and O atoms is almost spherical and decreases almost to zero between the atoms (Fig. 7.24(c)). The Li atom is in the spacious location of the network, and gives up almost all its valence

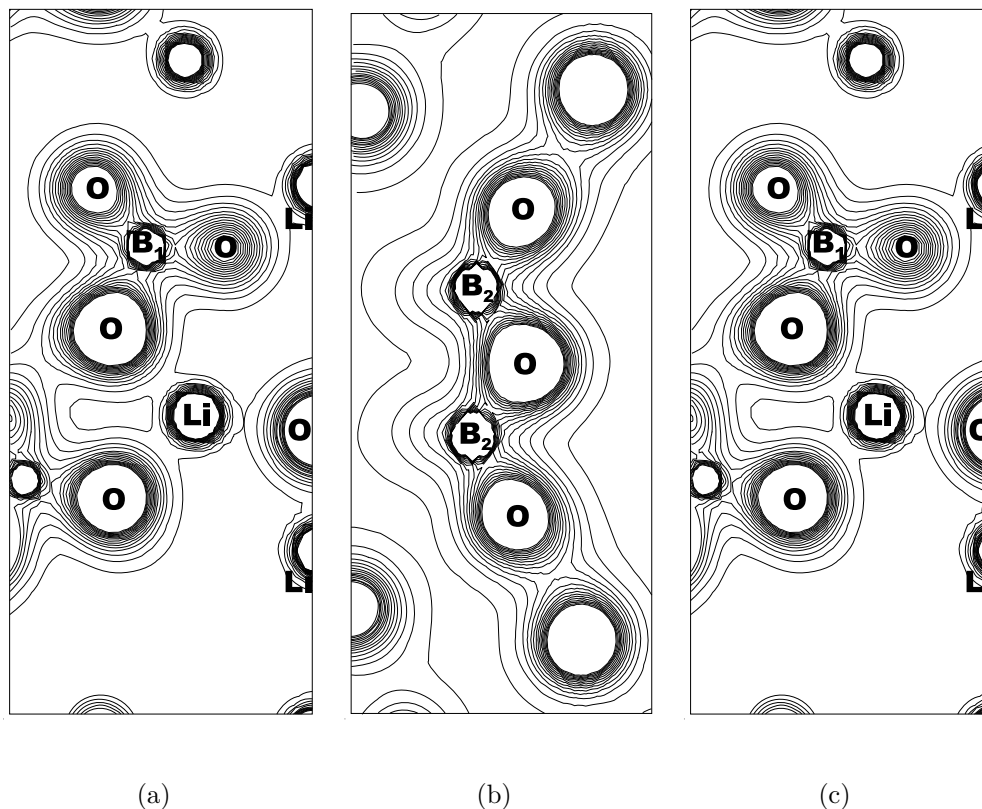


Figure 7.24: Electronic charge density distribution for LTB for plains containing O-B₁-O (a), O-B₂-O (b) and O-Li-O (c) angles.

charge, yet it does not have a large semi-core-like orbital to participate in a partially covalent type of bonding. The charge density magnitude between these two atoms is small which indicates that the bond is mainly ionic. This is in qualitative agreement with similar analysis of LiB_3O_5 [150].

As for Li_2O and B_2O_3 , PW1PW gives the best agreement with experiment for structural, energetic and electronic properties of $\text{Li}_2\text{B}_4\text{O}_7$. B3LYP gives the similar agreement for structural and electronic properties but smaller cohesive energy. Differences for the same functional PWGGA exist between CRYSTAL03 and VASP. Structural properties are similar. CRYSTAL-PWGGA gives close agreement for energetic properties with the experiment whereas VASP-PWGGA gives smaller values of E_u . Band gap is ≈ 0.5 eV lower with VASP-PWGGA compared to CRYSTAL-PWGGA. MSINDO gives overestimated lattice parameters and band gap. MSINDO cohesive energy is comparable with the DFT methods. The atomic basis set and energy cutoff have less effect on structural and energetic properties, whereas pronounced effect on electronic

properties.

Thus the best method of choice is either PW1PW or B3LYP for this type of complex system and for the study of ionic conductivity in ceramic oxides. But the hybrid methods are CPU time consuming. PWGGA can be the second best choice as it is comparatively less expensive.

8 Migration of Li^+ ion in $\text{Li}_2\text{B}_4\text{O}_7$

Crystalline lithium tetraborate (LTB) $\text{Li}_2\text{B}_4\text{O}_7$ is a Li^+ ion conductor along the (001) direction (polar axis) [139, 140]. There have been several experimental investigations on the ionic conductivity of this system [141–147]. It was suggested [141–143] that the conduction of Li^+ ion occurs through a one-dimensional channel in the tetragonal axis. The ionic conductivity in LTB is attributed to the cation vacancies [141, 142].

Several different values for the activation energy E_A of the ion migration in LTB appeared in the literature depending on the preparation method of the samples [143]. Kim *et al.* [142] showed a comparison of E_A for the LTB crystals prepared from $\text{Li}_2\text{B}_4\text{O}_7$ powder (LTBp) and from $\text{Li}_2\text{CO}_3\text{-B}_2\text{O}_3$ mixed powder (LTBm). Their measured value of activation energy for LTBp is 0.42 eV and that for LTBm is 0.46 eV.

In the present study, $\text{Li}_2\text{B}_4\text{O}_7$ is considered as a possible structure of the interface region of the $\text{Li}_2\text{O}:\text{B}_2\text{O}_3$ nanocomposite. A theoretical investigation of the cation vacancy defect and the migration of Li^+ ion in LTB is performed. The activation energy is calculated for the Li^+ ion movement from its original position to an adjacent cation vacancy position along the (001) direction. The calculated activation energy is compared with the experiment. The investigation was performed for a $\text{Li}_{16}\text{B}_{32}\text{O}_{56}$ supercell at the PW1PW level with BS B and the PWGGA-PAW method with energy cutoff E1. Larger BS and energy cutoff than these were not used as these would be too CPU time consuming.

8.1 Cation vacancy in lithium tetraborate

For the simulation of the cation vacancy in LTB, first a supercell $\text{Li}_{16}\text{B}_{32}\text{O}_{56}$ was created by using the transformation matrix \mathbf{L} (8.75).

$$\mathbf{L} = \begin{pmatrix} 0 & 1 & 1 \\ 1 & 0 & 1 \\ 1 & 1 & 0 \end{pmatrix} \quad (8.75)$$

One Li was removed from the cell to create the vacancy keeping the system neutral. The optimized geometry of the nondefective supercell was taken as starting structure for the defective system. The formation energy of cation vacancy $E_{de}(V)$ is calculated according to the Eq. (5.73) of cation vacancy defect in Li_2O as follows:

$$E_{de}(V) = E^{SCM}(V) + E(\text{Li}) - E^{SCM} \quad (8.76)$$

Here $E^{SCM}(V)$ and E^{SCM} denote the total energy of the supercell with and without vacancy, respectively, and $E(\text{Li})$ is the energy of the free Li atom. In Table 8.25 calculated $E_{de}(V)$ are presented. There is no experimental or previous theoretical value of cation vacancy formation energy of LTB. So the calculated $E_{de}(V)$ values are compared between each other in the following.

Table 8.25: Formation energy of cation vacancy, $E_{de}(V)$ (kJ/mol) in $\text{Li}_2\text{B}_4\text{O}_7$ for unrelaxed and relaxed structure.

System	PW1PW	PWGGA-PAW
unrelaxed	800	693
relaxed	728	658

Since PW1PW gives the best reproduction of the experimental bulk properties of LTB and also the defect properties of Li_2O , this method is taken as reference. The $E_{de}(V)$ obtained with PW1PW is 728 kJ/mol. As for cation vacancy defect in Li_2O (see Table 5.10), PWGGA-PAW method gives smaller value of $E_{de}(V)$ compared to PW1PW. The deviation is -70 kJ/mol. The relaxation energy, E_R at PW1PW level is 72 kJ/mol. The PWGGA-PAW E_R is 37 kJ/mol smaller than PW1PW E_R value. As for Li_2O , the E_R values with both methods are high, which indicates that relaxation is important for the defect properties and migration of defects.

The effect of relaxation is further investigated by measuring the changes of distances of the nearest oxygen atoms, boron atoms and lithium atoms with respect to the defect position. In nondefective LTB, the Li atom is surrounded by four close oxygen atoms in an arrangement which may be regarded as a considerably distorted tetrahedron [148,155]. The four lithium-oxygen distances lie in the range from 1.97 to 2.17 Å [148]. Thereupon follows a fifth lithium-oxygen distance of 2.611 Å, forming a oxygen five-vertex polyhedron [143,148]. The next lithium-oxygen distances are 2.85 Å and more. Hence the coordination around the lithium cannot be said truly fourfold. Here six nearest oxygens are considered to observe the effect of relaxation (Fig. 8.25). In Table 8.26, the calculated distances of O atoms from the vacancy before and after relaxation are shown. Here r_1, r_2, r_3, r_4, r_5 and r_6 denote the distance of O1, O2, O3, O4, O5 and O6, respectively, from the vacancy. The numbering follows the Fig. 8.25. It can be seen that all the oxygens move away from the vacancy. Both methods give similar

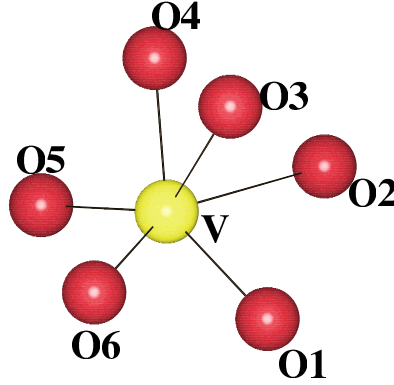


Figure 8.25: Six nearest oxygen atoms from the cation vacancy (V) in LTB crystal.

trend. This is due to the fact that the removal of a neutral Li atom creates a hole in

Table 8.26: Distances of the nearest oxygen atoms (r) Å from the Li vacancy and changes of the distances $\Delta r(\%)$ for the unrelaxed and relaxed atoms

Distance	PW1PW			PWGGA-PAW		
	Unrelaxed	Relaxed	$\Delta r(\%)$	Unrelaxed	Relaxed	$\Delta r(\%)$
r_1	1.96	2.04	+4.1 %	1.96	2.03	+3.0 %
r_2	2.00	2.10	+5.0 %	2.00	2.08	+4.0 %
r_3	2.08	2.13	+2.4 %	2.07	2.13	+2.9 %
r_4	2.09	2.18	+4.3 %	2.11	2.15	+1.9 %
r_5	2.73	2.85	+4.4 %	2.62	2.82	+7.6 %
r_6	2.84	2.85	+0.2 %	2.63	2.84	+0.4 %

the valence band. One of the surrounding oxygen atoms which was formally O^{2-} in nondefective LTB becomes O^- . One unpaired electron is localized on the $2p$ orbital of one of those oxygen atoms.

It should be noted that the sixth oxygen atom shows a small relaxation, +0.2 % (PW1PW) and +0.4 % (PWGGA-PAW), indicating that the position of this oxygen atom is almost unchanged.

The calculated distances of three nearest boron atoms and two nearest lithium atoms from the vacancy before and after relaxation are shown in Table 8.27. r_1 , r_2 and r_3 denote the distance of three boron atoms, respectively and r_4 denotes the distance of two lithium atoms from the vacancy. All the boron atoms move towards the vacancy. The position of the third boron atoms is unchanged with both the methods, 0.0 % (PW1PW) and -0.2 % (PWGGA-PAW). The reason could be that the boron atoms are

positively charged and therefore feel reduced electrostatic repulsion and move towards the vacancy. The two nearest lithium atoms show inward relaxation of -4.2% with

Table 8.27: Distances of the nearest boron and lithium atoms (r) Å from the Li vacancy and changes of the distances $\Delta r(\%)$ for the unrelaxed and relaxed atoms

Distance	PW1PW			PWGGA-PAW		
	Unrelaxed	Relaxed	$\Delta r(\%)$	Unrelaxed	Relaxed	$\Delta r(\%)$
r_1	2.66	2.65	-0.4%	2.66	2.64	-0.8%
r_2	2.69	2.69	-0.7%	2.68	2.65	-1.1%
r_3	2.86	2.86	-0.0%	2.838	2.831	-0.2%
r_4	3.06	2.93	-4.2%	3.08	2.99	-2.9%

the PW1PW and -2.9% with the PWGGA-PAW approach. Due to the reduced electrostatic repulsion, the Li atoms move towards the vacancy. This is in line with the relaxation of nearest lithium atoms for the cation vacancy defect in Li_2O (see Tables 5.11 and 5.12), where the nearest Li atoms show strong inward relaxation.

In the next section, the Li^+ ion migration through cation vacancies is discussed.

8.2 Migration of Li^+ ion

In LTB, Li^+ ion migrates through a one-dimensional channel of ion conduction path in the (001) direction [141–143]. In this channel, Li ions form five-vertex oxygen polyhedra (LiO_5). The high atomic packing density and the rigidity of triangular and tetrahedral boron-oxygen polyhedra prevent direct jumps of Li ions along the tetragonal axis [143]. Rather it is assumed that the Li^+ ion migrates through the large triangular faces of the two nearest oxygen five-vertex polyhedra facing each other. Ionic transport along this channel occurs through the cation vacancies [141, 142]. The distance of a Li^+ ion hop is less than 3.114 \AA , which is the distance between the lithium positions in LTB [148]. In Fig. 8.26, two nearest oxygen five-vertex polyhedra, one of the Li ion and the other of the adjacent cation vacancy (V), are shown. The arrow shows the direction of migrating Li^+ ion towards the vacancy. The migration path of Li^+ ion along the tetragonal axis can be illustrated as following.

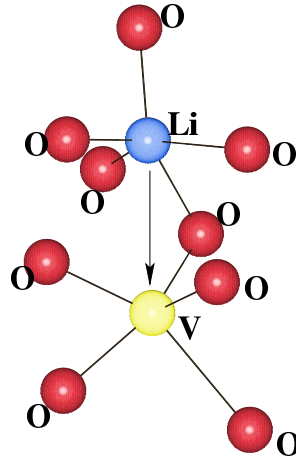


Figure 8.26: Two nearest oxygen five-vertex polyhedra of lithium along the tetragonal axis of LTB crystal.

The top view and side view of the schematic diagram of Li^+ ion migration in LTB are shown in Fig. 8.27 and 8.28. The migrating Li^+ ion and the vacancy are in their

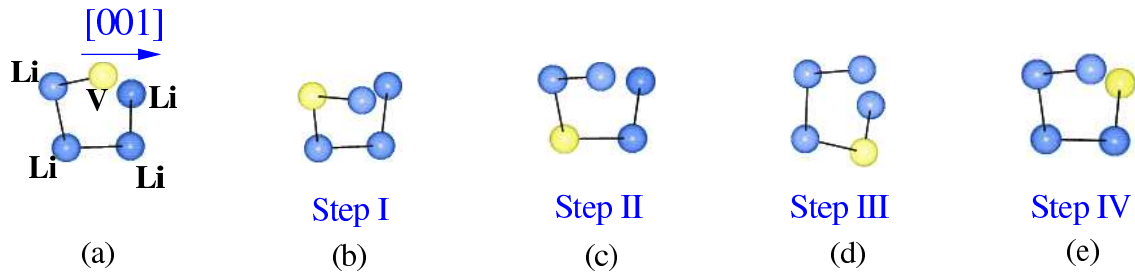


Figure 8.27: The schematic diagram of Li^+ ion migration in LTB (top view).

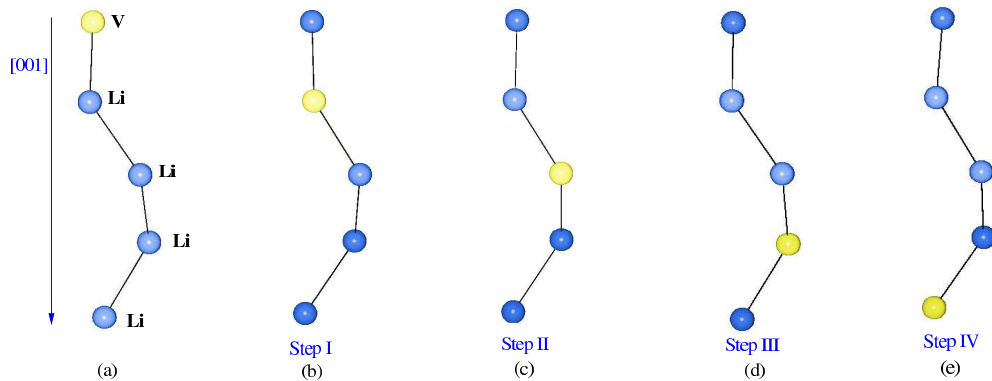


Figure 8.28: The schematic diagram of Li^+ ion migration in LTB (side view).

original position in Fig. 8.27(a) or 8.28(a). The entire migration path is modeled in four steps. In the first step, Step I (Fig. 8.27(b) or 8.28(b)) one Li^+ ion migrates to the adjacent vacancy. The migrating Li^+ ion accesses to the position of vacancy and the vacancy reaches to the original position of migrating ion. Similarly, in the

following steps, (Fig. 8.27(c),8.27(d), and 8.27(e) or 8.28(c), 8.28(d), and 8.28(e)) Li^+ ion migrates along the (001) direction.

In every step, there is an intermediate position that corresponds to the transition structure. The activation energy was calculated for the unrelaxed and relaxed systems. In Table 8.28, the calculated values E_A are compared with experimental value [142]. E_A for each of the four steps is calculated as the difference of the energy of the system in which the migrating ion is mid-way between the neighboring regular sites and the system in which the vacancy is on a regular site. The calculated values of hopping distance are 3.064 Å and 3.077 Å, with PW1PW and PWGGA-PAW, respectively, which are in good agreement with the experimental hopping distance of 3 Å [143]. In Fig. 8.29, the potential energy curves for the Li^+ ion migration in LTB for unrelaxed systems are shown. In each step, the migration path is modeled in ten sub-steps.

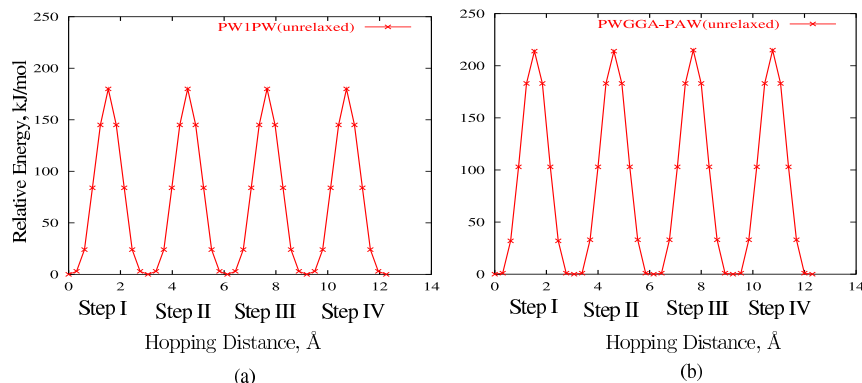


Figure 8.29: Potential energy curves for Li^+ ion migration in LTB for unrelaxed systems, (a) PWGGA-PAW and (b) PW1PW.

In every step, E_A is equal as the local environment of the migrating Li^+ ion and the vacancy is identical. For the unrelaxed system, both PW1PW and PWGGA-PAW methods give too large values for E_A compared to the experiment (Table 8.28). This is in line with the previous finding for the Li^+ ion diffusion in Li_2O (see Table 5.17).

Table 8.28: Comparison of calculated activation energy, E_A (eV) for unrelaxed and relaxed systems with experimental value

System	PW1PW	PWGGA-PAW	Exp. [142]
unrelaxed	1.87	2.22	
relaxed	0.37	0.27	0.42, 0.46

The potential energy curves for Li^+ ion migration for the relaxed systems are shown in Fig. 8.30. All 102 atoms surrounding the migrating Li^+ ion and the vacancy of the supercell were relaxed. The activation energy was calculated for every step of migration. The calculated values of E_A are given in Table 8.28. It can be seen that relaxation has a large effect on the E_A . Both methods give good agreement with experiment. As for Li_2O , PW1PW approach gives the best agreement with the experimental value of E_A , deviating by only 0.05 eV.

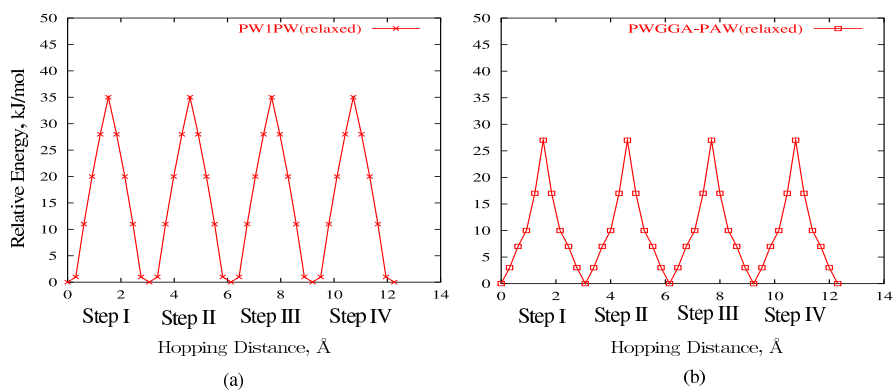


Figure 8.30: Potential energy curves for Li^+ ion migration in LTB for relaxed systems, (a) PWGGA-PAW and (b) PW1PW.

9 Model System for the $\text{Li}_2\text{O}:\text{B}_2\text{O}_3$ nanocomposite

In the last decade, the diffusion in nanocrystalline ceramics have received considerable interest. The diffusion in ionic crystals is related to ion transport and thus to electrical conductivity. The conductivity in ceramic oxides is observed in single-phase systems as well as in composites of different components [64–66,156]. A good example of single-phase nanocrystalline ceramic is Li_2O as Li ion conductor [64]. Composite materials show enhanced conductivity compared to the single-phase ceramic oxides. It was observed that the conductivity is higher in $\text{Li}_2\text{O}:\text{B}_2\text{O}_3$ nanocomposites than in Li_2O , although B_2O_3 is an insulator [64,66]. This is due to the increased fraction of structurally disordered interfacial regions or enhanced surface area [66].

In nanocrystalline Li_2O , there are interfaces between similar crystallites. Whereas, $\text{Li}_2\text{O}:\text{B}_2\text{O}_3$ nanocomposites contain three types of interfaces, these are interfaces between the ionic conductor grains, between the insulator grains and between the ionic conductor and the insulator grains (see Fig. 4.5). The latter can lead to surprising effects in the conductivity of composite materials [66]. The conductivity enhancement in the interfacial regions may have different origins, e.g. the formation of space charge layers, an enhanced concentration of dislocations, or defects or the formation of new phases [66,157–159].

In the present study, a quantum chemical investigation is performed to understand the mechanism of the enhanced conductivity in $\text{Li}_2\text{O}:\text{B}_2\text{O}_3$ nanocomposite. First, an interface of $\text{Li}_2\text{O}:\text{B}_2\text{O}_3$ nanocomposite was modeled by the combination of two favorable surfaces of Li_2O and B_2O_3 . The defect properties were investigated in the interface region. The ionic conductivity was then investigated by the calculation of the activation energy, E_A for the Li ion movement. The calculations were performed at the PW1PW approach with BS A.

9.1 Construction of the $\text{Li}_2\text{O}:\text{B}_2\text{O}_3$ interface

The expression 'interface' denotes the two-dimensional transition region between three-dimensional regions that are homogeneous in the equilibrium case [160]. The internal interfaces may include two different types of boundaries, such as, Type-1: the both phase boundaries which mean the interfaces between grains of different structure and

Type-2: the proper grain boundaries which mean the interfaces between grains of the same structure. Heitjans *et al.* [66] suggested that the conductivity enhancement in $\text{Li}_2\text{O}:\text{B}_2\text{O}_3$ nanocomposites is due to the increased fraction of interface between the ionic conductor and the insulator grains, which corresponds to Type-1.

The aim is to construct an interface region between the ionic conductor grains (Li_2O) and the insulator grains (B_2O_3) by combining the stable surfaces of these two crystals. It is assumed that their surfaces are the most stable lattice planes. Therefore, the surface energies of Li_2O and B_2O_3 are studied.

9.1.1 Surface energy of Li_2O

In recent theoretical investigations [161, 162], it was shown that the (111) and (110) surfaces of Li_2O are most stable. Here these two stable surfaces are studied.

Slabs parallel to the (111) and (110) surfaces were studied for various numbers of layers ($n = 3, 6, 9, 12$ and $n = 5, 10$, respectively). Top view and side view of slabs of the (111) and the (110) surfaces are shown in Figs. 9.31 and 9.32, respectively.

The lattice parameters of the (111) surface are $a = b = 3.229 \text{ \AA}$, and $\gamma = 120^\circ$ and those of the (110) surface are $a = 3.229 \text{ \AA}$, $b = 4.567 \text{ \AA}$ and $\gamma = 90^\circ$.

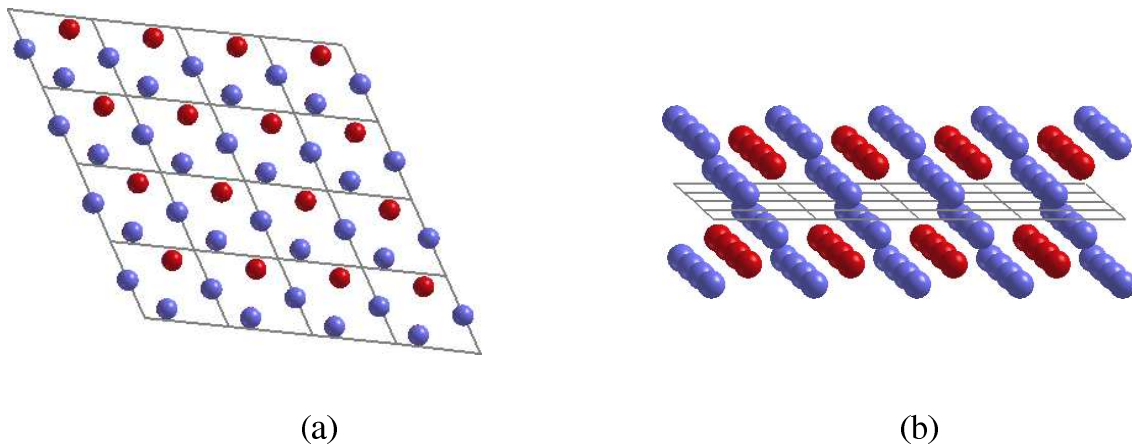


Figure 9.31: Top view (a) and side view (b) of a slab parallel to the (111) surface of Li_2O . Red spheres represent oxygen atoms and blue spheres represent lithium atoms

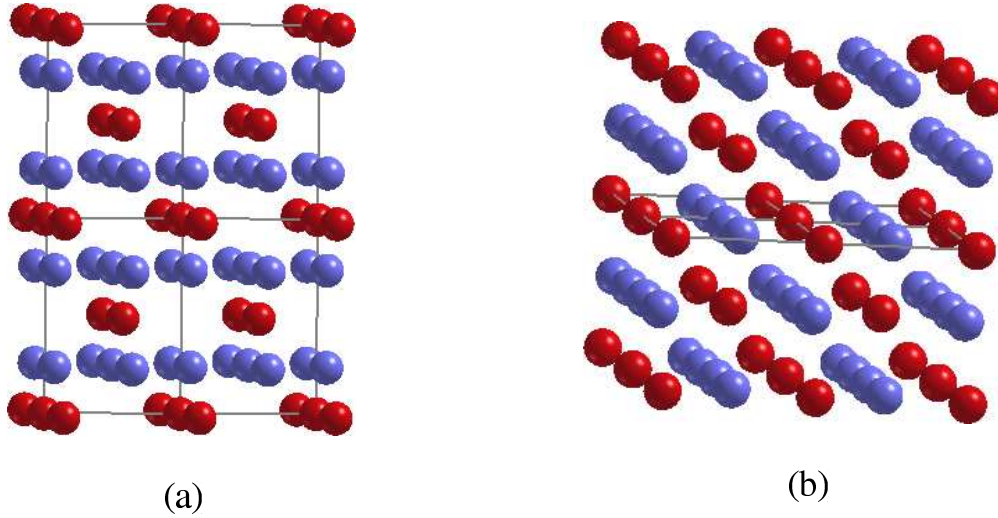


Figure 9.32: Top view (a) and side view (b) of a slab parallel to the (110) surface of Li_2O . Red spheres represent oxygen atoms and blue spheres represent lithium atoms

In Tables 9.29 and 9.30, the surface energies and their convergence with increasing number of layers are presented for unrelaxed and relaxed slabs. The surface energy (E_s) was calculated according to the equation

$$E_s = \frac{E_{\text{slab}} - E_{\text{bulk}}}{2A} \quad (9.77)$$

where E_{slab} is the total energy of the two-dimensional slab, E_{bulk} is the total energy of the three-dimensional bulk and A is the surface area of the slab. For the (111) surface, E_s has converged within 0.001 Jm^{-2} with a six-layer slab (Table 9.29). Thus there is fast convergence with the number of layers for the (111) surface.

Table 9.29: Comparison of calculated surface formation energies E_s (Jm^{-2}) of (111) surface before and after relaxation

n	E_s (unrelaxed)	E_s (relaxed)
3	0.815	0.799
6	0.819	0.789
9	0.820	0.790
12	0.821	0.790

For the (110) surface, E_s has converged with a five-layer slab (Table 9.30). There is a larger relaxation effect for the (110) surface compared to that for the (111) surface.

Table 9.30: Comparison of calculated surface formation energies E_s (Jm^{-2}) of (110) surface before and after relaxation

n	E_s (non-relaxed)	E_s (relaxed)
5	1.440	1.243
10	1.440	1.240

The converged E_s value of the (111) surface is 0.79 Jm^{-2} and that of the (110) surface is 1.24 Jm^{-2} . Therefore the (111) surface is the most stable surface of Li_2O . This agrees well with the HF *ab initio* study of Li_2O surfaces by Lichanot *et al.* [162].

9.1.2 Surface energy of B_2O_3

To the best of my knowledge, there is no experimental or theoretical investigation on the stability of B_2O_3 surfaces. There are several possible stable low-index B_2O_3 surfaces, such as, (001) or (111) or (100). In the present study, only the (001) surface of B_2O_3 is investigated. The aim is to construct a suitable model of a $\text{Li}_2\text{O}:\text{B}_2\text{O}_3$ nanocomposite. For this purpose, the (001) surface of B_2O_3 is the best choice for the following reasons.

In a recent investigation of Li ion transport and interface percolation in nano- and microcrystalline composites [163], the $\text{Li}_2\text{O}:\text{B}_2\text{O}_3$ composite was considered as brick-layer type model. Three different possibilities were presented in that study, such as, the two conducting grains immersed in an insulating material connected to each other parallelly, or connected at the edge, or connected at the corner. Among them, the first one shows the most enhanced conductivity. On the basis of this model, the interface would be constructed by the combination of a supercell of the most stable Li_2O (111) surface with a supercell of a suitable B_2O_3 surface. In this case, the lattice vectors of B_2O_3 surface should fit to those of the Li_2O (111) surface. The lattice parameters of the B_2O_3 (001) surface are $a = b = 4.352 \text{ \AA}$, and $\gamma = 120^\circ$ which fit well with those of the Li_2O (111) surface. Whereas, the lattice vectors of B_2O_3 (111) and B_2O_3 (100) surfaces are $a = 7.538 \text{ \AA}$, $b = 9.456 \text{ \AA}$, $\gamma = 113.49^\circ$ and $a = 4.352 \text{ \AA}$, $b = 8.395 \text{ \AA}$, $\gamma = 90^\circ$, respectively. For this reason, only the B_2O_3 (001) surface is taken into account in the present study. In the following, the convergence of surface energy E_s of B_2O_3 (001)

surface is discussed.

Slabs parallel to the (001) surface were studied with increasing number of layers ($n = 5, 10, 15$ and 30). Top view and side view of slab of B_2O_3 (001) surface are shown in Fig. 9.33.

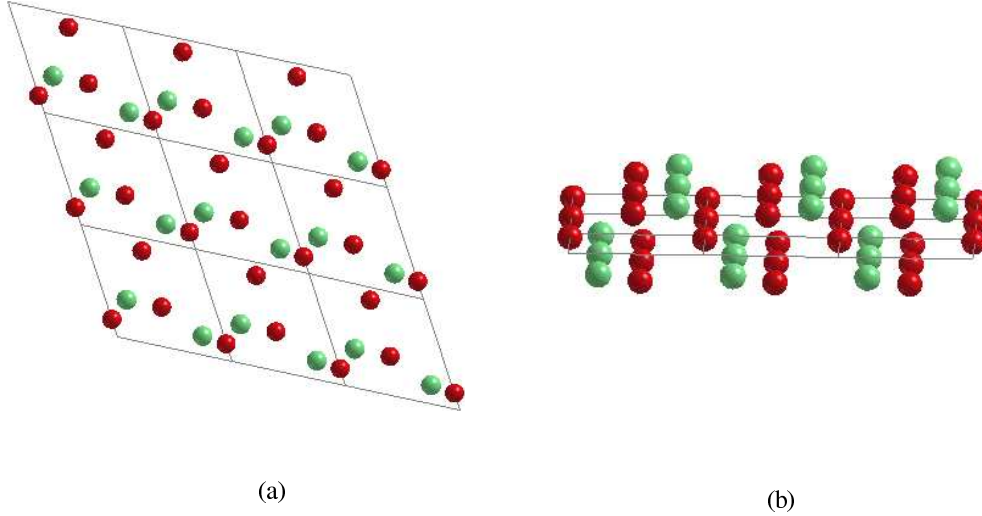


Figure 9.33: Top view (a) and side view (b) of the slab parallel to (001) surface of B_2O_3 . Red spheres represent oxygen atoms and green spheres represent boron atoms

In Table 9.31, the surface energies and their convergence with slab thickness are presented for unrelaxed and relaxed slabs. E_s is calculated according to equation (9.77). E_s is converged within 0.05 Jm^{-2} with the five-layer slab. There is a large effect of relaxation compared to the Li_2O surfaces which is an indication of the more covalent nature of the B-O bond. The surface atoms compensate the loss of a bond by increasing the interaction to atoms in the second layer.

Table 9.31: Comparison of calculated surface formation energies E_s (Jm^{-2}) of (001) surface before and after relaxation

n	E_s (non-relaxed)	E_s (relaxed)
5	4.246	2.115
10	4.307	2.167
15	4.313	2.188
30	4.336	2.206

9.1.3 Interface of $\text{Li}_2\text{O}:\text{B}_2\text{O}_3$ nanocomposite

The $\text{Li}_2\text{O}:\text{B}_2\text{O}_3$ nanocomposite is constructed by the combination of supercells of Li_2O (111) surface and B_2O_3 (001) surface. First a 4×4 supercell of six-layer slab parallel to the (111) surface for Li_2O was created. The lattice parameters of this supercell are $a = b = 13.0 \text{ \AA}$, and $\gamma = 120^\circ$. Then a 3×3 supercell of a five-layer slab parallel to the (001) surface for B_2O_3 was created. The lattice parameters of this supercell are also $a = b = 13.0 \text{ \AA}$, and $\gamma = 120^\circ$. Then these two supercells were combined to create a two-dimensional model of the $\text{Li}_2\text{O}:\text{B}_2\text{O}_3$ nanocomposite as shown in Fig. 9.34.

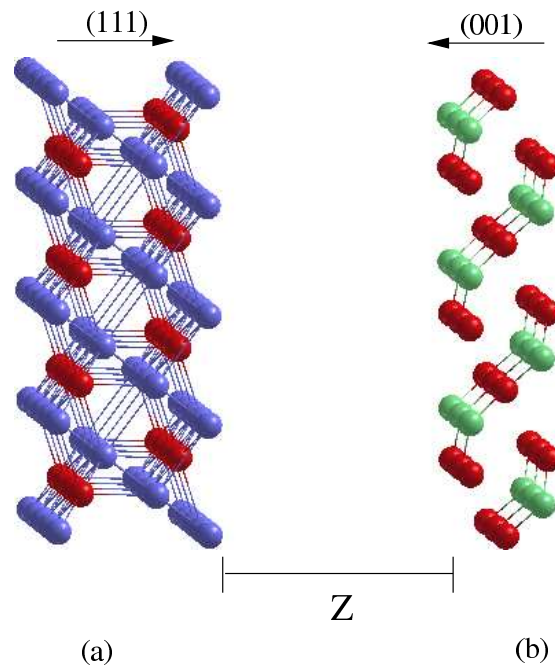


Figure 9.34: Mixture of supercells of (111) slab of Li_2O (a) and (001) slab of B_2O_3 (b).

The distance (Z) between the two slabs is set to 10 \AA initially.

Initially, the distance (Z) between the two slabs was set to 10 \AA . Z was then optimized with fixed a . Taking the optimized value of Z , the lattice parameter a was optimized. In Fig. 9.35, the optimization of Z and a is presented. The optimized values of Z and a are 5.0 \AA and 12.4 \AA , respectively. 75 atoms in the interface region of two slabs are relaxed which is considered as the interface of $\text{Li}_2\text{O}:\text{B}_2\text{O}_3$ nanocomposite.

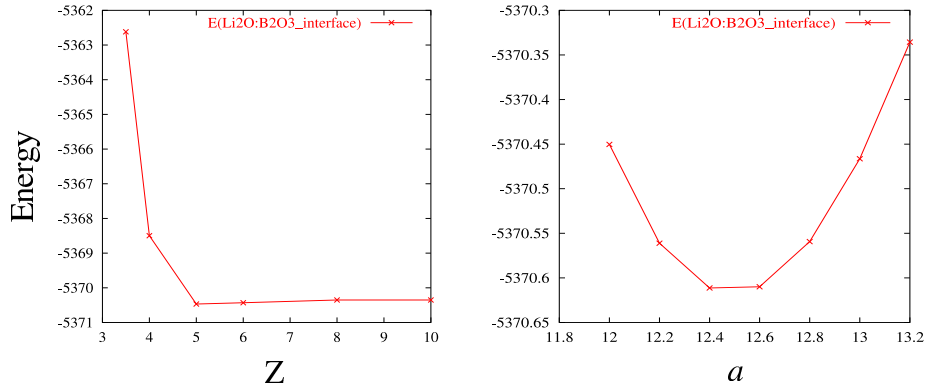


Figure 9.35: Optimization of interface distance (Z) and lattice parameter a Å.

The interface region is marked with a box in the Fig. 9.36(a). The remaining atoms in the outermost layers are kept fixed at bulk-like positions.

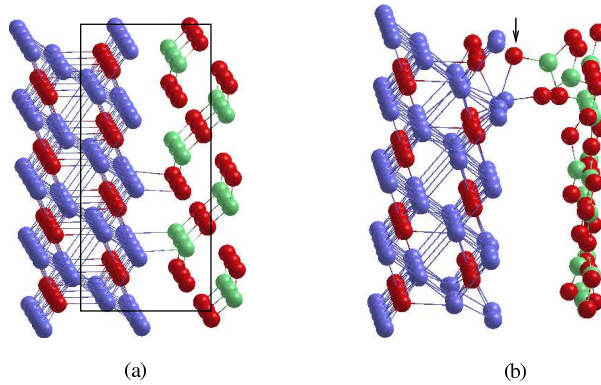


Figure 9.36: The interface of $\text{Li}_2\text{O}:\text{B}_2\text{O}_3$ nanocomposite before (a) and after (b) optimization.

A full optimization of atomic fractional coordinates of the interface region was performed taking the optimized values of Z and a . The optimized structure is shown in Fig. 9.36(b). It is observed that all boron and oxygen atoms of B_2O_3 surface move from the interface region towards the boundary atoms and thus form several rings of trigonal BO_3 . One of the oxygen atoms of Li_2O surface (marked by an arrow in Fig. 9.36(b)) also moves towards the boron atom and readily forms an additional bond. In the B_2O_3 (001) surface, the boron atoms are coordinated to two oxygen atoms at a distance of 1.31-1.33 Å. Whereas, in the interface of $\text{Li}_2\text{O}:\text{B}_2\text{O}_3$ nanocomposite, the boron atoms are three-fold coordinated to oxygen atoms as in the case of the three-dimensional bulk trigonal B_2O_3 [109]. The average B-O bond distance of the BO_3 group is 1.41 Å, which is 0.04 Å larger than that in bulk B_2O_3 . The BO_3 triangle is very close to planar, the sum of the three O-B-O angles being 359.2°.

Whereas, lithium atoms have two different types of coordination with oxygen atoms in the interface region. In one type, the lithium atoms are coordinated to three oxygen atoms (O1, O2 and O3) at an average distance of 1.9 Å. The fourth Li-O bond distance is larger than 3.2 Å. This oxygen (O4) is bonded to a boron atom at distance of 1.35 Å (as shown in Fig. 9.37(a)).

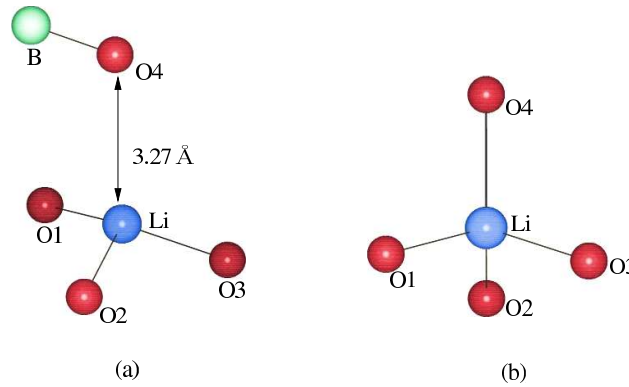


Figure 9.37: The coordination of lithium atom with oxygen atoms. (a) One oxygen atom (O4) has large bond distance with Li which is also bonded to boron atom. (b) Slightly distorted tetrahedral coordination of lithium atom with oxygen atoms.

In the other type, lithium atom is coordinated to four closer oxygen atoms at distances of 1.87 Å, 1.90 Å, 1.98 Å and 2.10 Å, which can be considered as a distorted tetrahedron as shown in Fig. 9.37(b). It can be noted that the lithium atoms are tetrahedrally coordinated to oxygen atoms at a distance of 2.0 Å in bulk Li_2O . Thus lithium has reduced coordination number in the interface of $\text{Li}_2\text{O}:\text{B}_2\text{O}_3$ nanocomposite. Nearly all the lithium atoms move from their positions at the perfect (111) surface, some of them come very close while some other move far from each other. The nearest Li-Li distances vary from 2.15 Å to 2.30 Å compared to 2.23 Å before optimization.

It is well known for the grain boundaries in nanocrystalline metals that many atoms have a reduced coordination number with respect to the grain interior and the local density is smaller, which leads to an enhanced diffusivity of the atoms [164]. Such an effect is expected to be found also in ceramic systems [66]. In the interface of $\text{Li}_2\text{O}:\text{B}_2\text{O}_3$, there is Li-O bond weakening and simultaneously B-O bond formation. Li atom shows reduced coordination number in the grain boundary. This process might reduce the bond strength of lithium to the oxygen atoms in the interface region.

Consequently, the defect formation could be easier in the $\text{Li}_2\text{O}:\text{B}_2\text{O}_3$ nanocomposite compared to nanocrystalline Li_2O which is assumed to be responsible for enhancing the Li^+ ion conductivity. In the next section, the defect properties in $\text{Li}_2\text{O}:\text{B}_2\text{O}_3$ nanocomposite are discussed.

9.2 Defect properties in $\text{Li}_2\text{O}:\text{B}_2\text{O}_3$ nanocomposite

The nanocrystalline materials are regarded as heterogeneously disordered with ordered grains and disordered interfaces. The interface atoms occupy regular sites but have reduced coordination number and the interface regions may be classified as highly defective [66]. In addition to grain boundaries, further structural elements that occur with high concentration are triple junctions, i.e. the borderlines where three adjacent crystallites are brought into contact. These may form channels with vacancy-like sites and thus fast diffusion pathways, as predicted by theory [165].

Nanocrystalline Li_2O is a good Li^+ ion conductor and Li^+ ion migrates via cation vacancies [84–86] (see chapter 5.4). The overall conductivity increases if B_2O_3 is added to Li_2O , although B_2O_3 is an insulator [64–66]. This is explained by an enhanced conductivity in the interfacial regions between the ionic conductor grains and the insulator grains. The possible reason for the enhanced conductivity is the enhanced concentration of dislocations, or defects or the formation of new phases [66, 157–159]. In the present section, cation vacancy and Li^+ ion migration in $\text{Li}_2\text{O}:\text{B}_2\text{O}_3$ nanocomposite are discussed.

9.2.1 Cation vacancy

The vacancy is created by removing one Li from the interface region of $\text{Li}_2\text{O}:\text{B}_2\text{O}_3$ nanocomposite, keeping the system neutral. The formation energy of cation vacancy $E_{de}(V)$ is calculated as,

$$E_{de}(V) = E^{Nan}(V) + E(\text{Li}) - E^{Nan} \quad (9.78)$$

Here $E^{Nan}(V)$ and E^{Nan} denote the total energy of the $\text{Li}_2\text{O}:\text{B}_2\text{O}_3$ nanocomposite with and without vacancy, and $E(\text{Li})$ is the energy of the free Li atom. In Table 9.32, the calculated $E_{de}(V)$ of $\text{Li}_2\text{O}:\text{B}_2\text{O}_3$ nanocomposite is presented and also compared with that of nanocrystalline Li_2O .

Table 9.32: Formation energy of cation vacancy, $E_{de}(V)$ (kJ/mol) of $\text{Li}_2\text{O}:\text{B}_2\text{O}_3$ nanocomposite and nanocrystalline Li_2O (PW1PW results with BS A).

	$\text{Li}_2\text{O}:\text{B}_2\text{O}_3$	Li_2O
$E_{de}(V)$	533	577

The $E_{de}(V)$ of $\text{Li}_2\text{O}:\text{B}_2\text{O}_3$ nanocomposite is 533 kJ/mol which is 44 kJ/mol smaller than that of Li_2O . Thus the defect formation is easier in the $\text{Li}_2\text{O}:\text{B}_2\text{O}_3$ nanocomposite compared to that in Li_2O . This confirms that the interface region of $\text{Li}_2\text{O}:\text{B}_2\text{O}_3$ nanocomposite contains more defects than the nanocrystalline Li_2O . This may lead to faster migration of Li^+ ions in the interface region and in turn to enhanced conductivity in the $\text{Li}_2\text{O}:\text{B}_2\text{O}_3$ nanocomposite.

9.2.2 Migration of Li^+ ion

The migration of Li^+ ion in $\text{Li}_2\text{O}:\text{B}_2\text{O}_3$ nanocomposite was investigated by the calculation of activation energy E_A for the Li^+ ion diffusion in the interface region. Li^+ ion migrates via cation vacancy in the interface region. It was observed that (see chapter 9.1.3) lithium atoms have two different types of coordination with oxygen atoms in the interface region, one is three-fold (Fig. 9.37(a)), and the other one is four-fold (Fig. 9.37(b)). Thus there can be two possible mechanisms for the Li^+ ion migration, such as,

- Migration-I: a Li^+ ion migrates from a tetrahedral site to the cation vacancy (V) which is three-fold coordinated to oxygen atoms, or vice versa.
- Migration-II: a three-fold coordinated Li^+ ion migrates to the cation vacancy (V) which is also three-fold coordinated to oxygen atoms, or vice versa.

Both of these two mechanisms are illustrated in Fig. 9.38. In Migration-I (Fig. 9.38(a)), two oxygen atoms are common or bridging between the migrating Li^+ ion and the cation vacancy. Whereas, in Migration-II (Fig. 9.38(b)), there is one bridging oxygen atom between the migrating Li^+ ion and the cation vacancy.

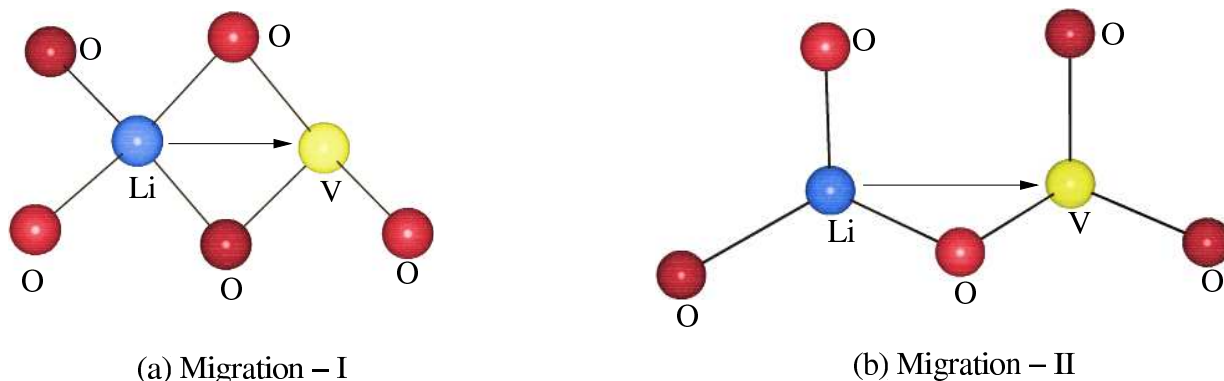


Figure 9.38: Li^+ ion migration in the interface of $\text{Li}_2\text{O}:\text{B}_2\text{O}_3$ nanocomposite, (a) A four-fold coordinated Li^+ ion migrates to the trigonally coordinated cation vacancy, (b) A three-fold coordinated Li^+ ion migrates to the three-fold coordinated cation vacancy.

In both cases, spin polarization plays an important role for the Li^+ ion migration. It was observed that the unpaired electron is localized on the $2p$ orbital of one of the surrounding oxygen atoms. The same situation was observed for the Li^+ ion diffusion in crystalline Li_2O (see chapter 5.4).

In Fig. 9.39, the potential energy curves for the Li^+ ion migration in the interface of $\text{Li}_2\text{O}:\text{B}_2\text{O}_3$ nanocomposite are shown for both types of migration.

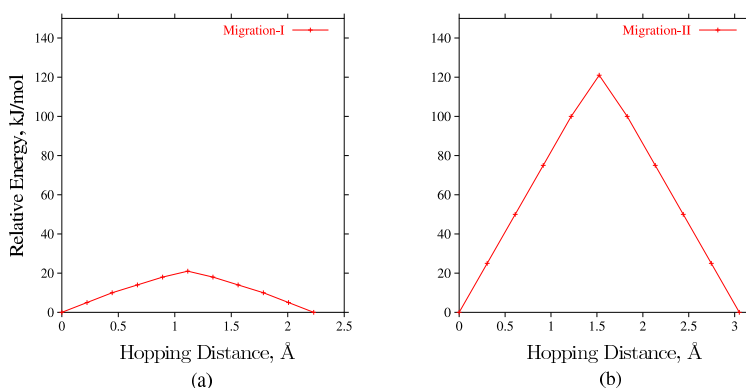


Figure 9.39: Potential energy curves of Li^+ ion migration in the interface of $\text{Li}_2\text{O}:\text{B}_2\text{O}_3$ nanocomposite, (a) Migration-I, (b) Migration-II.

The calculated values for the activation energy, E_A are presented in Table 9.33. E_A was calculated as the difference of energies for the systems in which the migrating ion is mid-way between the neighboring regular sites and the system in which the vacancy is on a regular site. The hopping distance of Li^+ ion migration in the case of Migration-I is 2.23 \AA , which is the distance of the nearest lithium atoms from the vacancy. Whereas

hopping distance in the case of Migration-II is 3.05 Å, which is the distance of next nearest lithium atoms from the vacancy. The experimental hopping distance for the migration of Li^+ ion in Li_2O is equal to the nearest Li-Li distance in Li_2O , namely, 2.29 Å.

Table 9.33: Comparison of calculated activation energies, E_A (eV) for the Li^+ ion migration in $\text{Li}_2\text{O}:\text{B}_2\text{O}_3$ nanocomposite and nanocrystalline Li_2O

	$\text{Li}_2\text{O}:\text{B}_2\text{O}_3$		Li_2O	
	Migration-I	Migration-II	Calculated ^a	Exp. [66]
E_A	0.22	1.18	0.33	0.31

^a Discussed in chapter 5.4

E_A for Migration-I is 0.22 eV and that for Migration-II is 1.18 eV. Thus the Li^+ ion migrates faster in Migration-I than in Migration-II. Therefore, Li^+ ion migration is much more favorable at a distance of the nearest lithium atoms than that of the next nearest lithium atoms. In Table 9.33, the calculated E_A values are also compared with that of Li_2O . It can be seen that E_A for the $\text{Li}_2\text{O}:\text{B}_2\text{O}_3$ nanocomposite is 0.09 eV smaller than the experimental E_A of nanocrystalline Li_2O . Thus it is confirmed that the Li^+ ion migration is faster in $\text{Li}_2\text{O}:\text{B}_2\text{O}_3$ nanocomposite than in Li_2O . Consequently, the conductivity is enhanced in the $\text{Li}_2\text{O}:\text{B}_2\text{O}_3$ nanocomposite.

10 Summary

The structural, energetic and electronic properties of Li_2O , B_2O_3 and $\text{Li}_2\text{B}_4\text{O}_7$ were investigated by means of periodic quantum-chemical calculations. The results of five DFT-type methods and the semiempirical method MSINDO were compared among each other and to available literature data. For MSINDO-CCM calculations, the standard Li parameters were reoptimized for crystalline Li_2O . Whereas, the calculations for B_2O_3 and $\text{Li}_2\text{B}_4\text{O}_7$ were performed with standard empirical parameters.

The comparison of optimized structural parameters shows that the hybrid methods PW1PW and B3LYP give the best results. Other DFT methods (PWGGA, PWGGA-US and PWGGA-PAW) give larger deviations from the experimental data. The comparison of PWGGA results in a LCAO and two plane wave implementations revealed that the basis set dependence on geometry parameters and the band structure is small, but is more pronounced for energetic properties. As for structural parameters, PW1PW gives the best agreement for the energetic and electronic properties with the experiment for all the systems. B3LYP gives similar agreement for the electronic properties, while too small values for the cohesive energy. MSINDO gives larger deviations for the lattice parameters, whereas the energetic and electronic properties are comparable to the DFT methods.

Bulk properties of B_2O_3 low-pressure phase ($\text{B}_2\text{O}_3\text{-I}$) were investigated for both P3_121 and P3_1 space groups. Based on a comparison of their structural, energetic and electronic properties, it is concluded that the two structures are practically the same. By comparing their cohesive energies, it is confirmed that the equilibrium structure is the recently proposed structure with the P3_121 space group.

A theoretical investigation was performed for the cation vacancy and F center in Li_2O . Formation energy of both types of defects was calculated. The convergence of defect formation energy was checked by extending the atomic basis set and energy cutoff. The structural relaxation effects for both types of defect were investigated. The study of electronic properties was performed by calculating the density of states (DOS) of the defective systems.

Li^+ ion diffusion in Li_2O was investigated. Li^+ ion migrates in Li_2O via cation vacancy. The activation energy, E_A for the migration was calculated for both unrelaxed

and relaxed systems. The calculated E_A with PW1PW is 0.33 eV which is 0.02 eV larger than the experimental value. The other DFT methods (B3LYP, PWGGA-US and PWGGA-PAW) give similar deviations from the experiment. Whereas, the reparameterized version of MSINDO does not give a barrier for migration, which must be considered as an artefact of this method.

$\text{Li}_2\text{B}_4\text{O}_7$ was considered as a first model system for the mixed interface of $\text{Li}_2\text{O}:\text{B}_2\text{O}_3$ nanocomposite. The formation energy of cation vacancy and the effect of structural relaxation around the cation vacancy were investigated with PW1PW and PWGGA-PAW methods. The Li^+ ion migration was investigated by measuring E_A . It was observed that Li^+ ion migrates through a one-dimensional channel of five-vertex oxygen polyhedra along the tetragonal axis of LTB crystal. The calculated E_A in LTB with PW1PW method is 0.37 eV which is 0.05 eV smaller than the experimental value. PWGGA-PAW gives a deviation of +0.15 eV compared to the experiment.

Finally, the migration of Li^+ ion was investigated in the $\text{Li}_2\text{O}:\text{B}_2\text{O}_3$ nanocomposite. Since PW1PW approach gives the best agreement with experiment for the bulk properties for all the systems, the defect properties and Li^+ ion conductivity in Li_2O and $\text{Li}_2\text{B}_4\text{O}_7$, this method was chosen for the investigation. A two-dimensional model system of the $\text{Li}_2\text{O}:\text{B}_2\text{O}_3$ interface region was created by the combination of supercells of Li_2O (111) surface and B_2O_3 (001) surface. The formation energy of cation vacancy in the interface of $\text{Li}_2\text{O}:\text{B}_2\text{O}_3$ nanocomposite is 533 kJ/mol, which is 44 kJ/mol lower than that in Li_2O . This shows that the interface region of $\text{Li}_2\text{O}:\text{B}_2\text{O}_3$ nanocomposite is more defective than the bulk, which facilitates the conductivity in this region. It was observed that lithium atoms have reduced coordination number in the interface region compared to Li_2O bulk. This leads to an enhanced mobility of Li^+ ion. Li^+ ion migrates from its regular site to an adjacent vacancy. The migration of Li^+ ion was investigated by calculating the E_A for this process. The calculated value of E_A is 0.22 eV. Compared to the experimental value of E_A for the nanocrystalline Li_2O (0.31 eV), E_A in the $\text{Li}_2\text{O}:\text{B}_2\text{O}_3$ nanocomposite is 0.09 eV lower. This confirms that the $\text{Li}_2\text{O}:\text{B}_2\text{O}_3$ nanocomposite shows enhanced conductivity along the phase boundary compared to that in the nanocrystalline Li_2O .

References

- [1] I. N. Levine, Quantum Chemistry 5th ed., Prentice Hall, New Jersey, 2000.
- [2] A. Szabo, N. S. Ostlund, Modern Quantum Chemistry, Dover Publications, New York, 1996.
- [3] A. R. Leach, Molecular Modelling - Principles and Applications, Addison Wesley Longman Limited, 1996.
- [4] P. A. M. Dirac, *Proc. Roy. Soc. (London)* **123**, 714 (1929).
- [5] M. Born, R. Oppenheimer, *Ann. Physik* **84**, 457 (1927).
- [6] T. Koopmans, *Physica* **1**, 104 (1934).
- [7] C. C. J. Roothaan, *Rev. Mod. Phys.* **23**, 69 (1951).
- [8] C. C. J. Roothaan, *Rev. Mod. Phys.* **32**, 179 (1960).
- [9] J. A. Pople, R. K. Nesbet, *J. Chem. Phys.* **22**, 571 (1954).
- [10] M. J. S. Dewar, C. Jie and J. Yu, *Tetrahedron* **49**, 5003 (1993).
- [11] M. Wolfsberg and L. Helmholz, *J. Chem. Phys.* **20**, 837 (1952).
- [12] J. A. Pople, D. P. Santry and G. A. Segal, *J. Chem. Phys.* **43**, S129 (1965).
- [13] J. A. Pople, D. L. Beveridge, P. A. Dobosh, *J. Chem. Phys.* **47**, 2026 (1967).
- [14] B. Ahlswede, K. Jug, *J. Comput. Chem.* **20**, 563 (1999).
- [15] D. N. Nanda, K. Jug, *Theor. Chim. Acta* **57**, 95 (1980).
- [16] P.-O. Löwdin, *J. Chem. Phys.* **18**, 365 (1950).
- [17] J. Schulz, R. Iffert, K. Jug, *Int. J. Quantum Chem.* **27**, 461 (1985).
- [18] M. C. Zerner, *Mol. Phys.* **23**, 963 (1972).
- [19] R. S. Mulliken, *J. Chim. Phys.* **46**, 497 (1949).
- [20] K. Jug, G. Geudtner, T. Homann, *J. Comput. Chem.* **21**, 974 (2000).

-
- [21] T. Bredow, G. Geudtner, K. Jug, *J. Comput. Chem.* **22**, 861 (2001).
- [22] T. Bredow and K. Jug, MSINDO, in *Electronic Encyclopedia of Computational Chemistry*, Eds. P. von R. Schleyer, N. L. Allinger, T. Clark, J. Gasteiger, P. A. Kollman, H. F. Schaefer III, P. R. Schreiner, Wiley, Chichester, UK, 2004.
- [23] C. Pisani, F. Corá, R. Nada, R. Orlando, *Comput. Phys. Commun.* **82**, 139 (1994).
- [24] T. Bredow, G. Geudtner, K. Jug, *J. Comp. Chem.* **22**, 89 (2001).
- [25] F. Janetzko, R. A. Evarestov, T. Bredow, K. Jug, *phys. stat. soli. (b)* **241**, 1032 (2004).
- [26] T. Homann, T. Bredow, K. Jug, *Surf. Sci.* **555**, 135 (2004).
- [27] K. Jug, T. Homann, T. Bredow, *J. Phys. Chem. A* **108**, 2966 (2004).
- [28] R. G. Parr, W. Yang, *Density-Functional Theory of Atoms and Molecules*, Oxford University Press New York 1989.
- [29] C. J. Cramer, *Essentials of Computational Chemistry Theories and Models*, John Wiley and Sons, Ltd, 2002.
- [30] P. Hohenberg, W. Kohn, *Phys. Rev.* **136**, B864 (1964).
- [31] W. Kohn, L. J. Sham, *Phys. Rev.* **140**, A1133 (1965).
- [32] P. A. M. Dirac, *Proc. Camb. Phil. Soc.* **26**, 376 (1930).
- [33] J. P. Perdew and Y. Wang, *Phys. Rev. B* **45**, 13244 (1992).
- [34] A. D. Becke, *Phys. Rev. A* **38**, 3098 (1988).
- [35] C. Lee, W. Yang, R. G. Parr, *Phys. Rev. B* **37**, 785 (1988).
- [36] A. D. Becke, *J. Chem. Phys.* **98**, 5648 (1993).
- [37] T. Bredow, A.R. Gerson, *Phys. Rev. B* **61** 5194 (2000).
- [38] C. Kittel, *Introduction to Solid State Physics*, 7th ed., John Wiley & Sons, Inc. New York, 1996.

-
- [39] F. Bloch, *Z. Physik* **57**, 545 (1929).
- [40] R. Dovesi in *Quantum-Mechanical Ab-initio Calculation of the Properties of Crystalline Materials*, C. Pisani (Ed.), Springer-Verlag Berlin 1996, S. 31 ff.
- [41] V. R. Saunders, R. Dovesi, C. Roetti, R. Orlando, C. M. Zicovich-Wilson, N. M. Harrison, K. Doll, B. Civalleri, I. Bush, Ph. D'Arco, M. Llunell CRYSTAL2003 User's Manual, University of Torino, Torino, 2003.
- [42] S. F. Boys and F. Bernardi, *Mol. Phys.* **19**, 553 (1970).
- [43] E. R. Davidson and D. Feller, *Chem. Rev.* **86**, 681 (1986).
- [44] A. D. Corso in *Quantum-Mechanical Ab-initio Calculation of the Properties of Crystalline Materials*, C. Pisani (Ed.), Springer-Verlag Berlin 1996, S. 155 ff.
- [45] X. Gonze and Fabio Finocchi *Physica Scripta* **T109** 40 (2004).
- [46] G. Kresse, J. Hafner, *Phys. Rev. B* **47**, 558 (1993).
- [47] G. Kresse, J. Hafner, *Phys. Rev. B* **48**, 13115 (1993).
- [48] G. Kresse, J. Hafner, *Phys. Rev. B* **49**, 14251 (1994).
- [49] D. R. Hamann, M. Schlüter, and C. Chiang, *Phys. Rev. Lett.* **43**, 1494 (1979).
- [50] G. B. Bachelet, D. R. Hamann, and M. Schlüter, *Phys. Rev. B* **26**, 4199 (1982).
- [51] D. Vanderbilt, *Phys. Rev. B* **41**, 7892 (1990).
- [52] G. Kresse, J. Hafner, *J. Phys.: Condens. Matter* **6**, 8245 (1994).
- [53] G. Kresse, J. Joubert, *Phys. Rev. B* **59**, 1758 (1999).
- [54] E. G. Moroni, G. Kresse, J. Hafner, and J. Furthmüller, *Phys. Rev. B* **56**, 15629 (1997).
- [55] P. E. Blöchl, *Phys. Rev. B* **50**, 17953 (1994).
- [56] A. M. Dobrotvorskii, R. A. Evarestov, *phys. stat. sol. (b)* **66**, 83 (1974).
- [57] H. M. Evjen, *Phys. Rev.* **39**, 675 (1932).

-
- [58] F. Janetzko, T. Bredow, K. Jug, *J. Chem. Phys.* **116**, 8994 (2002).
- [59] T. Bredow, R. A. Evarestov, and K. Jug, *phys. stat. sol. (b)* **222**, 495 (2000).
- [60] S. Huzinaga, C. Arnau, *Phys Rev* **54**, 1948 (1971).
- [61] H. Gleiter, *Prog. Mater. Science* **33**, 223 (1989).
- [62] R. W. Siegel, *Encycl. Appl. Phys.* **11**, 173 (1994).
- [63] A. S. Edelstain and R. C. Camarata, *Nanomaterials: Synthesis, Properties and Applications*, Institute of Physics Publ., Bristol and Philadelphia, 1996.
- [64] S. Indris, P. Heitjans, H. Roman and A. Bunde, *Phys. Rev. Lett.* **84**, 2889 (2000).
- [65] S. Indris, P. Heitjans, *Non-Crysta. Solids* **307-310**, 555 (2002).
- [66] P. Heitjans and S. Indris, *J. Phys.: Condens. Matter* **15**, 1257 (2003).
- [67] R. Wyckoff, *Crystal Structures*, New York: Interscience, 1963.
- [68] C.E Johnson, K. R. Kummerer, and E. Roth, *J. Nucl. Mater.* **155-157**, 188 (1988).
- [69] K. Noda, Y. Ishii, H. Ohno, H. Watanabe, and H. Matsui, *Adv. Ceram. Mater.* **25**, 155 (1989).
- [70] R. Dovesi, C. Roetti, C. Freyria-Fava, and M. Prencipe, *Chem. Phys.* **156**, 11 (1991).
- [71] J. Koput, K. A. Peterson, *J. Chem. Phys.* **116**, 9255 (2002).
- [72] A. Shukla, M. Dolg, P. Flude, H. Stoll, *J. Chem. Phys.* **108**, 8521 (1998).
- [73] F. Finocchi and C. Noguera, *Phys. Rev. B* **53**, 4989 (1996).
- [74] R. Dovesi, *Solid State Commun.* **54**, 183 (1985).
- [75] E. A. Mikajlo, K. L. Nixon, V. A. Coleman and M. J. Ford, *J. Phys.:Condens. Matter* **14**, 3587 (2002).
- [76] L. Liu, V. E. Henrich, W. P. Ellis, I. Shindo, *Phy. Rev. B*, **54**, 2236 (1996).
- [77] S. Albrecht, G. Onida, L. Reining, *Phys. Rev. B*, **55**, 10278 (1997).

-
- [78] S. Hull, T.W.D. Farley, W. Hayes, and M.T. Hutchings, *J. Nucl. Mater.* **160**, 125 (1988).
- [79] K. Noda, Y. Ishii, H. Matsui and H. Watanabe, *J. Nuc. Mater.* **133-134**, 205 (1985).
- [80] W. Rauch, *Z. Physik* **116**, 652 (1940).
- [81] Y. Ishii, J. Murakami and M. Itoh, *J. Phys. Soc. Japan* **68**, 2236 (1999).
- [82] M. Itoh, J. Murakami and Y. Ishi, *phys. stat. sol. (b)* **213**, 243 (1999).
- [83] N. M. Masaki, K. Noda, H. Watanabe, R. G. Clemmer, and G. W. Hollenberg, *J. Nucl. Mater.* **212-215**, 908 (1994).
- [84] A. De Vita, I. Manassidis, J. S. Lin and M. J. Gillan, *Europhys. Lett.* **19**, 605 (1992).
- [85] A. De Vita, M. J. Gillan, J. S. Lin, M. C. Payne, I. Stich, and L. J. Clarke, *Phys. Rev. Lett.* **68**, 3319 (1992).
- [86] A. V Chadwick, K. W. Flack, J.H. Strange and J. Harding, *Solid State Ionics* **28-30**, 185 (1988).
- [87] A. Shluger and N. Itoh, *J. Phys.: Condens. Matter* **2**, 4119 (1990).
- [88] H. Tanigawa and S. Tanaka, *J. Nucl. Mater.* **307-311**, 1446 (2002).
- [89] K. Noda, Y. Ishii, H. Matsui, and H. Watanabe, *Radiation Effects* **97**, 297 (1986).
- [90] J. M. Baker, A. Cox. A. J. O'Connell, and R.C.C Ward, *J. Phys.: Condens. Matter* **3**, 6189 (1991).
- [91] W.C. Mackrodt, *J. Mol. Liq.* **39**, 121 (1988).
- [92] K. Noda, K. Uchida, T. Tanifuji and S. Nasu, *J. Nucl. Mater.* **91**, 234 (1980).
- [93] K. Noda, K. Uchida, T. Tanifuji and S. Nasu, *Phys. Rev. B*, **24**, 3736 (1981).
- [94] CRC Handbook of Chemistry and Physics, 72nd Ed. CRC Press, Inc., 1991-1992.
- [95] K. Jug, G. Geudtner, *Chem. Phys. Lett.* **208**, 537 (1993).

- [96] T. Bredow, K. Jug, *Chem. Phys. Lett.* **223**, 89 (1994).
- [97] M. Prencipe, A. Zupan, R. Dovesi, E. Aprà, V. R. Saunders, *Phys. Rev. B* **51**, 3391 (1995).
- [98] L. Ojamäe, K. Hermansson, C. Pisani, M. Causà, C. Roetti, *Acta Cryst. B* **50**, 268 (1994).
- [99] T. Bredow, P. Heitjans and M. Wilkening, *Phys. Rev. B* , **70**, 115111 (2004).
- [100] M. Catti, G. Valerio, R. Dovesi, and M. Causà, *Phys. Rev. B* **49**, 14179 (1994).
- [101] VASP guide: <http://cms.mpi.univie.ac.at/vasp/vasp/vasp.html>
- [102] S. H. Vosko, L. Wilk and M. Nusair, *Can. J. Phys.* **58**, 1200 (1980).
- [103] O. V. Kovalev, Representations of the Crystallographic Space Groups: Irreducible Representations, Induced Representations, and Corepresentations, Gordon and Breach, Philadelphia, 1993.
- [104] C. Pisani, R. Dovesi and C. Roetti, Hartree-Fock *ab initio* Treatment of Crystalline Systems, Lecture Notes in chemistry, volume 48, Springer Verlag, Heidelberg, 1988.
- [105] H. J. Monkhorst and J. D. Pack, *Phys. Rev.* **13**, 5188 (1976).
- [106] D. A. Keen, *J. Phys.: Condens. Matter* **14**, R819 (2002).
- [107] N. Chawla, M. Kerr and K. K. Chawla, *J. Am. Ceram. Soc.* **88**, 101 (2005).
- [108] G. E. Gurr, P. W. Montgomery, C. D. Knutson and B. T. Gorres, *Acta Cryst* **B26**, 906 (1970).
- [109] H. Effenberger, C. L. Lengauer and E. Parthe, *Monats. Chem.* **132**, 1515 (2001).
- [110] C. T. Prewitt, R. D. Shannon, *Acta Cryst* **B24**, 869 (1968).
- [111] F. C. Kracek, G. W. Morey, and H. E. Merwin, *Am. J. Sci.* **35A**, 143 (1938).
- [112] C. W. Ong, H. Huang, B. Zheng, R. W. M. Kwok, Y. Y. Hui, and W. M. Lau, *J. Appl. Phys.* **95**, 3527 (2004).

- [113] Y. Muramatsu, H. Takenaka, T. Oyama, T. Hayashi, M.M. Grush, R.C.C. Perera, *X-Ray Spectrom.* **28**, 503 (1999).
- [114] D. Li and W. Y. Ching, *Phys. Rev. B* **54**, 13616 (1996).
- [115] A. Takada, C. R. A. Catlow, G. D. Price and C. L. Hayward, *Phys. Chem. Minerals* **24**, 423 (1997).
- [116] R. Orlando, R. Dovesi, C. Roetti, *J. Phys. Condens. Matter* **2**, 7769 (1990).
- [117] J. S. Binkley, J. A. Pople, and W. J. Hehre, *J. Am. Chem. Soc.* **102**, 939 (1980).
- [118] B.S.R. Sastry, F.A. Hummel, *J. Am. Ceram. Soc.* **41**, 7 (1958).
- [119] B.S.R. Sastry, F.A. Hummel, *J. Am. Ceram. Soc.* **42**, 216 (1959).
- [120] V.I. Aver'yanov, A.E. Kalmykov, *Glass Phys. Chem.* **16**, 492 (1990).
- [121] A. Jiang, S. Lei, O. Huang, T. Chen, D. Ke, *Acta Cryst. C* **46**, 1999 (1990).
- [122] L. Hanbin, S. Guangqiu, W. Xiaoqing, W. jingzhi and S. Denzhong, *Prog. Crystal Growth Character.* **40**, 235 (2000).
- [123] J. A. Kosinski, Y. Lu, A. Ballato, *IEEE Transactions on Ultrasonics, Ferroelectrics, and Frequency Control* **41**, 473 (1994).
- [124] R. Komatsu, T. Sugawara, N. Watanabe, *Rev. Laser Eng.* **27**, 541 (1999).
- [125] J. Hee-Rak, J. Byung-Moon, Ch. Jung-Won, K. Jung-Nam, *Mater. Lett.* **30**, 41 (1997).
- [126] K. Otsuka, M. Funami, M. Ito, H. Katsuda, M. Tacano, M. Adachi, A. Kawabata, *Jpn. J. Appl. Phys.* **34**, 2646 (1995).
- [127] M. Takeuchi, I. Odagawa, M. Tanaka, K. Yamanouchi, *Jpn. J. Appl. Phys.* **36**, 3091 (1997).
- [128] K.V. Shestopalov, V.A. Nefedov, B.I. Zadneprovsky, *In.: Proc. 1994 IEEE Int. Frequency Control Symp.*, 301, Boston, USA, 1994.

- [129] R. W. Whatmore, N. M. Shorrocks, C. O'Hara, F. W. Ainger, I. M. Young, *Electron. Lett.* **17**, 11 (1981).
- [130] R. Komatsu, T. Sugawara, K. Sassa, N. Sarukura, Z. Liu, S. Izumida, Y. Segawa, S. Uda, T. Fukuda, K. Yamanouchi, *Appl. Phys. Lett.* **70**, 3492 (1997).
- [131] T. Sugawara, R. Komatsu, and S. Uda, *Solid State Commun.* **107**, 233 (1998).
- [132] M. Adachi, K. Nakazawa, and A. Kawabata, *Ferroelectrics* **195**, 123 (1997).
- [133] J. Filipiak, A. Majchrowski, and T. Lukasiewicz, *Arch. Acoust.* **19**, 131 (1994).
- [134] A. S. Bhalla, L. E. Cross, and R. W. Whatmore, *Jpn. J. Appl. Phys.* **24**, 727 (1985).
- [135] M. Ono, M. Sakai, Y. Fujiwara, N. Wakatsuki, *In.: Proc. 1997 IEEE Ultrasonics Symp.* **2**, 1047, Toronto, Canada, 1997.
- [136] C. Furetta, P.S. Weng, *Operation Thermoluminescent dosimetry*, London, World scientific, 1998.
- [137] K. Mahesh, P.S. Weng, C. Furetta, *Thermoluminescence in solids and its applications* (Ashford, Nuclear Technology Publishing, 1989).
- [138] E.F. Dolzhenkova, V.N. Baumer, A.V. Tolmachev, B.M. Hunda, P.P. Puga, *6th Intern. Confer. on Inorganic Scintillators and their Applications* (Book of Abstracts, Chamonix, France, 210, 2001).
- [139] A. É. Aliev, Ya. V. Burak, and I. T. Lyseïko, *Izv. Akad. Nauk SSSR, Neorg. Mater.* **26**, 1991 (1990)
- [140] A. V. Burak, I. T. Lyseïko, and I. V. Garapin, *Ukr. Fiz. Zh.* **34**, 226 (1989)
- [141] C.-S. Kim, J.-H. Park, B. K. Moon, H.-J. Seo, B.-Ch. Choi, Y.-H. Hwang, H. K. Kim, J. N. Kim, *J. Appl. Phys.* **94**, 7246 (2003).
- [142] C.-S. Kim, D. J. Kim, Y.-H. Hwang, H. K. Kim, J. N. Kim, *J. Appl. Phys.* **92**, 4644 (2002).

- [143] I. M. Rizak, V. M. Rizak, N. D. Baisa, V. S. Bilanich, M. V. Boguslavskii, S. Yu. Stefanovich, and V. M. Golovei, *Cryst. Rep.* **48**, 676 (2003).
- [144] V. M. Rizak, I. M. Rizak, N. D. Bausa, V. S. Bilanych, S. Yu. Stefanovych, M. B. Bohuslavskii, V. M. Holovey, *Ferroelectrics* **286**, 771 (2003).
- [145] C.-S. Kim, Y.H. Hwang, H.K. Kim, J.N. Kim, *Phys. Chem. Glass.* **44**, 166 (2003).
- [146] D. P. Button, L. S. Mason, H. L. Tuller, and D. R. Uhlmann, *Solid State Ionics* **9/10**, 585 (1983).
- [147] G. L. Paul and W. Taylor, *J. Phys. C* **15**, 1753 (1982).
- [148] S. F. Radaev, L. A. Muradyan, L. F. Malakhova, Ya. V. Burak, and V. I. Simonov, *Kristallografiya* **34**, 1400 (1989).
- [149] O. Kubaschewski, C. B. Alcock, and P. J. Spencer, *Materials Thermochemistry*, 6th ed.; p. 288. Pergamon Press, New York, 1992.
- [150] I. N. Ogorodnikov, V. A. Pustovarov, A. V. Kurzhalov, L. I. Isaenko, M. Kirm, and G. Zimmerer, *Phys. Solid State* **42**, 464 (2000).
- [151] A. Y. Kuznetsov, A. V. Kruzhalov, I. N. Ogorodnikov, A. B. Sobolev and L. I. Isaenko, *Phys. Solid State* **41**, 48 (1999).
- [152] Ya. V. Burak, Ya. O. Dovgii, and I. V. Kityk, *Sov. Phys. Solid State* **31**, 1634 (1989).
- [153] R. H. French, J. W. Ling, F. S. Ohuchi, C. T. Chen, *Phys. Rev. B* **44**, 4896 (1991).
- [154] W. Y. Hsu, R. V. Kasowski, *J. Appl. Phys.* **73**, 4101 (1993).
- [155] J. Krogh-Moe, *Acta. Cryst.* **B24**, 179 (1967)
- [156] P. Knauth, *J. Electroceram* **5**, 111 (2000).
- [157] J. Maier, *Prog. Solid State Chem* **23**, 171 (1995).
- [158] M. Filal, C. Petot, M. Mokchah, C. Chateau and J. L. Carpentier, *Solid State Ion.* **80**, 27 (1995).

-
- [159] J. B. Phipps and D. H. Whitmore, *Solid State Ion.* **9**, 123 (1983).
- [160] J. Maier, *Physical Chemistry of Ionic Materials*, John Wiley & Sons, Ltd. West Sussex, 2004.
- [161] W. C. Mackrodt, and P. W. Tasker, *Chem. Br.* **21**, 366 (1985).
- [162] A. Lichanot, M. Gelize, C. Larrieu, and C. Pisani, *J. Phys. Chem. Solids* **52**, 1155 (1991).
- [163] M. Ulrich, A. Bunde, S. Indris and P. Heitjans, *Phys. Chem. Chem. Phys.* **6**, 3680 (2004).
- [164] I. Kaur, Y. Mishin and W. Gust, *Fundamentals of Grain and Interphase Boundary Diffusion*, New York: Wiley (1995).
- [165] S. V. Divinski and L. N. Larikov, *Defect Diffus. Forum* **143-147**, 1469 (1997).

Curriculum Vitae

Mohammad Mazharul Islam

27/07/1977	Born in Dhaka, Bangladesh
1987 - 1992	Secondary School, Dhaka, Bangladesh
1993 - 1994	Higher Secondary School, Notre Dame College, Dhaka, Bangladesh
1995 - 1997	Study for Bachelor of Science (Honours) in Chemistry at the University of Dhaka.
July 1999	Receiving of B.Sc (Hons) Certificate in Chemistry at the University of Dhaka.
1997 - 1998	Study for Master of Science in Chemistry at the University of Dhaka
1999-2000	Research work for submission of M.Sc dissertation
March 2001	Submission of M.Sc. dissertation. Title of Thesis: <i>Semi-empirical and Ab initio Study of the Substituent Effect on the Ionization of the Substituted Benzoic Acid and Hydrolysis of Substituted Ethyl Benzoate</i>
April 2002 -	Started Ph.D. in the Institute for Theoretical Chemistry, at the University of Hannover under the supervision of Priv.-Doz. Dr. T. Bredow

Publications

1. Mazharul M. Islam, Volodymyr V. Maslyuk, Thomas Bredow, Christian Minot, Structural and electronic properties of $\text{Li}_2\text{B}_4\text{O}_7$, *J. Phys. Chem B*, **109**, 13597 (2005).
2. Volodymyr V. Maslyuk, Mazharul M. Islam, Thomas Bredow, Electronic properties of compounds of the $\text{Li}_2\text{O-B}_2\text{O}_3$ system, *Phys. Rev. B*, in press (2005).